博士論文

Mesoscopic deconstruction and reconstruction of multicellular organizations:

Towards a nonequilibrium phase transition theory of complex adaptive systems

(多細胞組織のメゾスコピックレベルでの分解と再構成:

複雑適応系の非平衡相転移理論に向けて)

Lou Yuting

楼　玉婷

Department of Human and Engineered Environmental Sciences

Graduate School of Frontier Sciences

The University of Tokyo

東京大学大学院　　新領域創成科学研究科　　人間環境学専攻

February 2018

Acknowledgement

First of all, I would like to thank my parents for always encouraging and supporting me during my life in Japan.

I extend sincere gratitude to my supervisor Prof. Yu Chen, to Prof. Ping Ao, Prof. Wei Tang for their instructions on my research. Especially, I give thanks to Dr. Jufeng Xia for conducting the experiments, the results of which become the crucial part of Chapter 3 in this thesis.

I also express my gratitude to Prof. Zhifeng Shao, Prof. Andreas Deutsch, Prof. Fernando Peruani, Prof. Didier Sornette, Dr. Xiaomei Zhu for providing me valuable discussions and suggestions on the methodological and theoretical part in my thesis. I also thank Prof. Hiroshi Okuda, Prof. Yasuhiro Inoue, Prof. Hirotada Ohashi, and Prof. Eiji Hihara for proposing to me many critical but inspiring questions in the defense of my thesis.

Finally, I sincerely thank RA program of the University of Tokyo grants for Ph.D. research, JASSO scholarship for foreign students, and Japan Society for the Promotion of Science for funding my three-year doctoral research.

Content

Chapter 1

Introduction

1.1 Incipit

From its birth, science is the practice of the philosophy of reductionism [1-4]. Every phenomenon observed in nature shall have its dissected parts originating in the properties of the elements in the sub-scales. A typical scientific approach subsumes the proposal of hypotheses (some abstractive articulation of the properties of sub-scale elements) that can be validated or falsified in real life through the control of critical variables [Fig.1.1(A)]. The relationship between the sub-scale elements and the phenomena of interest can usually be elaborated by stringent mathematical or logical representations, the universal ones of which are deemed as “laws”. Through this paradigm, a tree structure of the scientific disciplines on various scales can be idealized, with elementary particle physics at the root. Nevertheless, with the elevation of the scale, the complexity of the problems of interest explodes. Particularly, the reductionist formalism has severer limitations in exploring the complex adaptive systems (at the top of the disciplinary tree) when the integrity of the complexity cannot be reducible to finite well-defined parts on the sub-levels [5-7]. For instance, one cannot even approach the properties of some materials with the basic principle of particle physics, e.g., the Schrödinger equation of nuclei and electrons [6]. In many complex adaptive systems (CASs) such as biological organisms and socioeconomic systems, multiple factors on multiple microscopic scales behave interdependently in complicated ways to induce insurmountable complexities at the macroscopic level. It seems that human’s reasoning ability (both computational and mathematical), so far, is insufficient to practice large-scale science with the pure superposition of small-scale laws. The old conundrum that “the whole is something besides the parts” pointed out by Aristotle [8] stands long over thousands of years.

The very core of conquering complexity is to achieve a proper understanding of the nature of complexity and of the scientific tools to deal with it. In the 20th century, complexity was thought to originate merely from the non-linearity and high-dimensionality. Urged by the rising demand for processing the monstrous amount of biological data, mathematicians and computer scientists have been involved in engineering complexity and have recognized (at least in biological systems) that complexity can be classified into three types: reducible, self-averaging, and wild [9]. Reducible complexity refers to the complexity in which its degrees of freedom can be eventually reduced to very low. This means that although numerous microscopic parts constitute the macroscopic integrity, very few of them (or modules of them) are indispensable. Self-averaging complexity refers to the high-dimensional complexity that has a stable low-dimensional approximated description by averaging over many degrees of freedom. The Central limit theorem [10] is one of the most famous representations stating a universal type of self-averaging complexity in nature. This also conforms to the fundamental principle of statistical physics as explicated by Landau [11] that "when the number of particles is large, the regularity appears". The third type, wild complexity, refers to those intractable, chaotic and inseparable to sub-scales.

To tackle these distinct types of complexity, modern science has developed new paradigms as opposed to the old reductionist ones. One of the most successful is the statistical physics, which has not only solved problems in gases and condensed matters but also extends to biological, financial, economic, societal and ecological problems where self-averaging complexity may exist [12-16]. Its magic lies in the attention to the interdependence structure of the sub-scale elements instead of the detailed mechanics of these elements. In spite of the distinctive mechanics of sub-elements on different scales, the complex macroscopic phenomenon is not sensitive to these details due to the self-averaging nature of the complexity. Some interdependence structures beneath, by contrast, can prevail across scales to reproduce consistent macroscopic system behaviors, thereby enabling an alternative representation of the complex system with simpler mechanistic rules which are easy to analyze. Meanwhile, with the development of the computational technology as well as the explosion of data volume, data-driven details substitute the hypotheses or laws on the smaller scales that base the reductionist model construction, making the wild complexity accessible at least in the computational world. This data-driven modeling for real complex objects also serves as a complementary role for the identification and management of reducible complexity through a set of tools for model reduction [17].

Although such non-reductionist approaches thrive in recent decades aiming at harness complexity in a variety of scientific fields [18-20], this stream of science is still in its infancy. Critical issues like the trade-off between the validity and the analyzability of the model still exist to undermine its scientific power to solve the complexity problems in practice. One may understand this methodological dilemma for the science

of complexity more deeply if looking into the efforts and struggles in the field of systems biology [21].

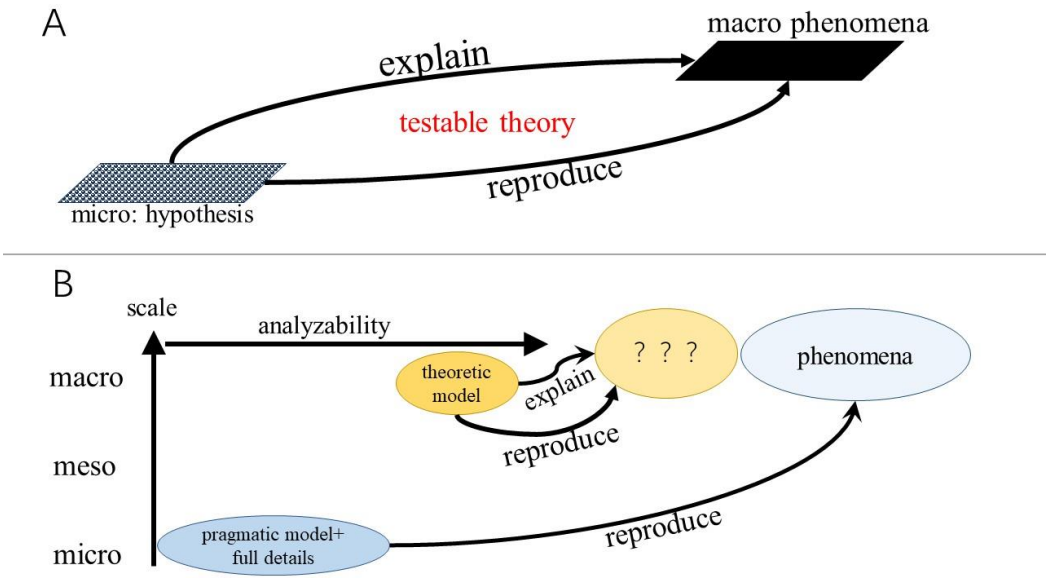

Figure 1.1 Modeling scheme for simple system (A) and complex systems (B).

1.2 Multicellular systems and systems biology

Biological complexity is the largest research focus within the realm of complexity science for its tremendous data quantity available. The calls for studies on multicellular systems are increasing with the high incidence of chronic and systematic diseases such as cancer, diabetes, HIV in modern societies. Multicellular systems are complex because they have many kinds of cells cooperative to maintain system functions under the signals from extra-, inter- and intra-cellular levels; they are also adaptive to turbulent physiological environments. Moreover, different from many complex materials in physics, they are open, dissipative and elusive.

Traditional science to the phenomena on the multicellular level is to identify pathological reasons underlying at the subcellular level. Take complicated diseases for instance: the elementary subcellular parts like the abnormal genetic expression, or the malfunction of some critical signaling pathways are supposed to explain everything as the atomic laws supposed to construct all large-scale phenomena. However, many chronic diseases such as cancer, dystonia, diabetes, psoriasis, and among others, have diverse origins and are susceptible to various conditions, hence there is no definite cure

for them so far.

Systems biology, as a new sub-category of biology using anti-reductionist approaches, then comes to the stage and is anticipated by many to unravel the elusive biological complexities [18]. Its anti-reductionist nature is revealed by the term "system". Systems biology embraces two branches: pragmatic systems biology, which emphasizes on the large-scale interactions between molecules [22-23], and systems-theoretic biology, which emphasizes on the system principles [24-25]. Pragmatic systems biology encompasses the details of the sub-cellular level as many as possible based on empirical data and serves as an ideal platform for managing reducible complexity. Systems-theoretic biology, by contrast, only consider the simple models that target at different types of self-averaging complexity. Therefore, pragmatic systems biology is bottom-up and data-driven with a solid biological basis on the microscopic level, while systems-theoretic biology is top-down and hypothesis-driven, with abstract interdependence structures that may outline the skeleton of the system. These two branches of systems biology can be regarded as partially inheriting the old-fashioned science (mentioned in the first paragraph in Ch.1.1) because the pragmatic one grasps a tint of reductionism while the theoretic one trying to obey the hypothesis-driven convention. The existing split of the reductionist and hypothetical formalisms in two branches renders critical question to systems biology about its scientific power. The problem with pragmatic systems biology is the difficulty to draw hypotheses or theories because the models are too complicated or the data is too massive; with systems-theoretic biology, the proposed hypotheses have too vague biological meanings to be testable in experiments because the model demonstrations are too simple [see Fig1.1 (B)]. Awareness is rising that only the integration of both pragmatic and theoretic methods can make systems biology a true science which produces verifiable or falsifiable hypotheses and help engineer real biological complexities [21].

1.3 Mesoscopic approach

In this thesis, I am devoted to unraveling the complexity of multicellular systems as a typical instance of CASs by proposing a mesoscopic anti-reductionist approach for merging the complicated microscopic details and simplified theoretical explanations. The mesoscopic approach, standing between bottom-up and top-down fashions, serves to shrink the gap between pragmatic and theoretic branches. The rationale behind this methodology is that for any system (either man-made or natural) with substantial complexities, the reducible and self-averaging ones can be well-understood through top-down simple models and there shall be the various simpler isomorphic representations across the scales of those complicated systems targeting at the

phenomena of interest. Hence the challenge lies in how to map the bottom-up complicated models, which have high phenomenological reliability, to the appropriate top-down simple ones, which have the strength of mechanistic illustration. Constructing a model at the **mesoscopic** level that properly captures the skeleton of the complicated models and is reducible to simpler models shall be one solution. For multicellular systems, the mesoscopic model could have the microscopic details modularized at the cellular level (which is hereafter referred to as "cell-based") instead of the genomic level. The benefit of the cell-based representation of multicellular systems lies in its capability of being mapped to simple theoretic models that can easily find their analogs which are solvable under standard analytical schemes.

1.4 Mesoscopic multicellular models

For multicellular systems, an appropriate mesoscopic standpoint is a single cell. Any details on subcellular levels can be aggregated into the description of single-cell-based behaviors; meanwhile, any macroscopic information that is central to our knowledge about a multicellular system (such as the number and the positions of the cells or the structure and the order of the cell population dynamics) could emerge from the interactions of these well-expressed single cells.

The existing mesoscopic models can be classified into two categories: Lagrangian and Eulerian. In analogy to the Lagrangian and Eulerian specifications of the fluid dynamics, Lagrangian models specify the kinetics of every single cell, therefore usually embedded in an off-lattice space. By contrast, Eulerian models specify the dynamics of each position point in the space, therefore having an on-lattice spatial setting. Usually in fluid mechanics, these two specifications can be easily transformed to each other through neat equations; nevertheless, in the modeling of multicellular systems, such convenient transformation between two formalisms can hardly be found due to the model complexity. In the following subsections, I will introduce several typical models of Lagrangian and Eulerian representations and their powers for different modeling goals.

1.4.1 Eulerian models

Eulerian specifications of the systems describe the "number" in question by position. A typical representation of the dynamics is the partial differential equation (PDE) of position and time variables, i.e., describing the time-dependent "fields". Mostly, the partial differential equations are in the "diffusion and reaction" type [27]: The numbers/amounts of cells or extracellular substance vital to cellular processes are

changing spatially and temporarily based on the principles of chemical reactions and diffusions, and cell chemotaxis or haptotaxis, whose coefficients of reactions or diffusions can be measured from experiments. The interactions between cells will be parameterized by the coefficients. These partial differential equations are very powerful for reproducing pattern formation since the proposal by Turing in 1952 [28].

Another typical representation of the Eulerian formalism is the cellular-automaton (CA)-like family. The system exists on the predefined lattice network and each node of the lattice can have different states whose kinetics are based on a set of simple and hypothetical rules for interactions between neighboring nodes. One node can represent a subset of, a single or several cells. Two remarkable models in this category are lattice-gas cellular automaton (LGCA) [29] and cellular Potts model(CPM) or GGH model[30]. LGCA is a biological realization of the lattice gas method for fluid modeling, where the flowing parcels at one lattice node are multiple single cells. The most eminent advantage of LGCA is its extendibility to macro continuum equations (e.g. the master equations) which are more analyzable. By contrast, the lattice node in CPM is only a small part inside a single cell and each node is labeled by the index of this cell; therefore, a CPM cell could be outlined by the alignment of nodes of the same labels. The change of label follows the simple rule of minimizing the cell-specific surface tension (represented by a Hamiltonian). Therefore, CPM is very powerful for reproducing deformable cell shape and for simulating tissue morphogenesis and cell sorting [31].

CA-like models can also combine with discretized PDEs to modulate the node states kinetics under the impact of extracellular fields (e.g., in tumor growth [32], angiogenesis [32, 33] or vasculogenesis of blood vessels[34]) because both types of models fall into the Eulerian formalism. These models usually entail discrete-continuum techniques [35] to discretize spatiotemporally the continuous PDEs for merging the CA rules.

1.4.2 Lagrangian models

The Eulerian specification of multicellular systems is intimately related to a macroscopic continuum description; by contrast, the Lagrangian specification is more compatible with microscopic details. In Lagrangian models, each individual element (e.g. a cell), instead of a predefined position (e.g. a node in a lattice) is followed through time. This enables one to embrace more individual processes (such as the activation of signaling pathways, the occurrence of mutations inside the cell) into the models. Particularly, when the biological problems at hand involve cell biomechanics, for instance, the cell shape change with viscoelasticity of cell membrane, which is considered critical to subcellular biochemical processes, the Lagrangian formalism will be the suitable one.

For addressing biochemical problems, the multicellular system can be modeled as

an aggregation of viscoelastic particles. There are many variants of such kind of multi-particle models, whose modeling goals are the forces of cell compression, deformation and adhesion during different cellular processes (growth, division, migration, necrosis, etc.). Since the system coordinates are individual-centered, Lagrangian models are mostly lattice-free. Sophisticated sub-cellular functions can also be embedded in each cell to model more realistic biochemical processes and the degree of sophistication of the individual subcellular formalism will decide how detailed the model could be. Some remarkable models are vertex model[36], colloidal particle model[37], deformable ellipsoidal cell model[38], subcellular element model[40], finite-element model[41], etc.

Lagrangian models can also be coupled with Eulerian models to establish hybrid multi-scale models for some complex modeling goals that require specification of individual cellular processes [42]. For example, the immersed-boundary cell (IBcell) model (see Ch.2.1) needs Eulerian models for simulating the fluid motions of extracellular factors and Lagrangian models for simulating individual viscoelastic cells to reproduce the hydrodynamics around heart[43], blood clotting[45], epithelial tissue embryogenesis[44], among others. Since these models are advantageous at giving specified modeling details, they are more difficult to analyze and yet serve as good foundations upon which the mesoscopic approaches can base.

1.5 Thesis objective

The aim of this thesis is twofold: one is the achievement towards theory establishment for multicellular homeostasis through a mesoscopic methodology and the other is the methodological exploration of engineering complex adaptive systems. In the following chapters, I am devoted to demonstrating that how a complicated multicellular system can be deconstructed to the cellular level and reconstructed to theoretic models with minimal complexity for the phenomena of interest on the top (which is homeostasis, tumorigenesis, and aging).

The outline of the thesis is as follows: In Ch.2, a mesoscopic model adapted from a complicated hybrid multi-scale model for multicellular homeostasis is introduced; both non-mutational and mutational situations are studied. Longtime simulations in a large parameter space are facilitated by this mesoscopic model. In Ch.3, I studied the multicellular aging through the comparison between *in vitro* experiments and mesoscopic models. Two mesoscopic models at different levels of scale contribute to the identification of the critical parameters for the multicellular aging and to the analogy between the critical behavior of the multicellular system and those of nonequilibrium physical systems. In Ch.4, the multicellular homeostasis is reproduced by a simple spin

model that can be representative of the complicated mesoscopic models. This minimal model can be analytically solved with standard procedures and a nonequilibrium phase transition theory is thence proposed. Ch.5 presents a discussion on the generalized mesoscopic methodology to other CASs and its application prospect.

Chapter 2

Multicellular homeostasis in silico

The maintenance of homeostasis in tissue is the essential theme for disease prevention [46]. Testable theories potentially helpful to the modulation of multicellular homeostasis are in high demand. Multicellular homeostasis *in silico* is the computational instance of the living multicellular systems keeping stable morphologies and functions. It mimics the real tissue homeostasis based on massive empirical pre-knowledge at the subcellular, cellular and multicellular levels. The models intended for reproducing multicellular homeostasis are hybrid, multi-scale, and mostly in a coupled Eulerian with Lagrangian formalism. One of the most successful models for multicellular homeostasis is the Immersed Boundary cell model for epithelium formation proposed by Rejniak *et al*. In this chapter, I will show how this detail-ridden model can be simplified to a mesoscopic model that is more computationally and theoretically achievable without losing the information critical to the phenomena of homeostasis maintenance.

2.1 Model

(Note: All figures in Ch. 2.1 and Ch. 2.2 are adapted from Ref.[49].)

The immersed boundary method was first proposed by Peskin [43] for reproducing flow patterns around heart valves and was then developed to a prototype model for deformable eukaryotic cells. As inferred by its name, the immersed boundary cell model (IBcell) is mainly featured by the dynamics of elastic cell membranes (i.e., cell boundary) immersed in a viscous Newtonian fluid which corresponds to cytoplasm inside the single cells, the extracellular matrix outside the tissue and empty room (or

lumen) existing in the multicellular architecture [47]. Not only does the complex cell morphology can be accurately reproduced, the cell phenotype decision can also be well represented through the molecular dynamics on the cell membranes which receive extra-, inter- and intracellular signals. Both the fluid dynamics and molecular dynamics are represented by a set of ordinary/partial differential equations and the intercellular adhesion is modeled by an elastic spring satisfying Hook's law. All the kinetic constants and coefficients are the empirical value obtained from the experimental results in the literature, manifesting the data-driven nature of this method. Since the cell membrane mechanics are at the cellular level and the molecular dynamics are at the subcellular level, the coupling between them can be realized by setting thresholds on the sub-cellular level to trigger the cellular behaviors. By embedding specific fluid and molecular dynamics into IBcell framework, one can reproduce both the precise multicellular architecture as well as cell phenotype dynamics for some specific tissue types.

A direct comparison between experimental data and IBcell simulation results can be performed to shows its remarkable phenomenological power. Rejniak *et al* have applied IBcell framework to epithelial acini formation and to reproduce the four homeostatic states with distinct multicellular architectural structures observable in experiments (see Ch.2.1.3 for details) [48]. Their computational results shed new light on multicellular homeostasis that the abnormality of the systems such as degeneration and tumorigenesis can also be some other homeostatic states, which emerge merely from the multicellular interactions without environmental stresses or malignant genetic alterations. Nevertheless, the Navier-Stokes equations for the fluid dynamics and the heavy details regarding the forces exerted on cell membranes in IBcell require huge computational resource and hamper a thorough exploration of the mechanistic reasons behind the diversity of multicellular homeostasis. The small cell number and the short simulation time because of this computational inefficiency also limits the feasibility of drawing a complete theory of homeostasis formation and transition.

As is pointed out in Ch.1.1, the complexity can be categorized into three parts: reducible, self-averaging and wild. Clearly, in terms of the homeostasis formation, many sub-elements in the IBcell can be reduced and the interdependence structure producing self-averaging complexity can be well-kept with a simpler model representation. Despite that the largest phenomenological power of IBcell lies in the accurate modeling of the cell morphologies comparable with the experimental images, those complex details should be reduced or replaced by other simple ones as the research goal is to generate falsifiable hypotheses for the diversity of multicellular homeostasis.

2.1.1 Cell-based discrete receptor dynamics model (DRDM)

By examining the diverse homeostatic states reproduced by IBcell [48] (see Fig. 2.4 in 2.1.3), one can find that these homeostatic states can be distinguished from other aspects than the multicellular architecture. Indeed, another key macroscopic feature capable of distinguishing different homeostatic states is the distribution of cell phenotypes, i.e., the sub-population structures of the cell colony. Hence a new mesoscopic cell-based model [49] intended for cell phenotype dynamics has been proposed with higher computational efficiency but with lower morphological precision.

In the new mesoscopic model, the continuously formulated fluid and receptor dynamics in IBcell are spatiotemporally discretized to a set of cell behavioral rules. Different from IBcell, the simulation space in the new model is a torus lattice with the node spacing of a single cell size. Each lattice can be occupied at most by one cell. Hence, the cells in this mesoscopic model will longer have precise morphology. The receptors on the cell membrane are still functioning, yet the spatial information of these receptors on a subcellular scale will be lost. Thence, the receptor dynamics with the absence of the representation of cell membrane become totally Eulerian. The behaviors of a cell are executed when various types of the receptors hit or stay below the respective thresholds. Apparently, the receptor dynamics are the core of the model that govern the whole system dynamics, therefore the model is called discrete receptor dynamics model (DRDM) hereafter. Under this reformation, all the information from extra-, inter- and intracellular conditions is coarse-grained as the profile of a lattice node (a virtual "cell"; refer to Table 2.1) and could be traced for statistical analyses even with cell heterogeneity through a longtime evolution.

As shown in Table 2.1, the cell in the DRDM is a structure of data without the representation of cell membranes and subcellular organs. Information at three level of scales is embraced: at the cellular level, five types of receptors (growth, adhesion, ECM, arrest, and death) and extracellular matrix (ECM) are synthesized and degraded at each

Table 2.1 Profile of each lattice node in DRDM.

Node profile			
Receptor amounts R(t)	ECM	Thresholds T	Environment Information
Growth $R_g(t)$		Growth g	Growth factor γ
Adhesion $R_h(t)$		Polarization p	Growth-inhibiting factor a_{scr}
ECM $R_E(t)$	concentration	ECM e	Death-inducing factor d_{scr}
Arrest $R_a(t)$	$E(t)$	Arrest a	Neighbors:
Death $R_d(t)$		Death d	left, right, top, bottom
		Adhesion h	

Note: The receptor amounts and ECM concentrations are dynamically updated, whereas the thresholds T and environment information are constant and homogeneous. The neighboring nodes of each node are four Von Neumann nodes throughout the simulations.

cell node; at the subcellular level, thresholds T embrace genetic information of the cell inheritable from its mother; at the extracellular level, the environmental information includes the addresses of neighboring nodes along with the nutrients, the growth inhibitors, and the death-inducing factors. Each cell can access the profiles of neighbors for localized intercellular interaction by visiting their addresses. If the node is not occupied, the amount of receptor and ECM will be zero.

All cells in the DRDM (also in IBcell) are the progenitor cells in epithelial tissues with cell differentiation not modeled. Three paralleled modules of cell behaviors are considered: cellular process, migration, and death [see Fig.2.1(A)]. The module of cellular process encompasses cell growth, cell proliferation, cell adhesion, cell polarization and the subsequent cell cycle arrest. The programs of cell movement and cell suicide are checked each time step whether the necessary environmental or internal conditions are met. Note that the elementary component in DRDM is a cell, one-time iteration should be much coarser than that of the characteristic timescale of molecular dynamics. Fig.2.1(B) shows the realization the cell behavior in simulation as a flowchart for each round of iteration.

Now let's specify the detailed receptor dynamics for each time iteration. Table 2.2 shows the evolution rules for each type of receptor with the corresponding cell behaviors, which is, in fact, the transformation of receptor configuration at each node [Fig. 2.1(C)]. Growth receptors are the only source of energy and other receptors can be transformed from the growth receptors through different transitional paths according to the cellular conditions (the first column in Table 2.2); eventually, all of the receptors should, in theory, flow towards death receptors because death receptors are non-degradable whereas the remaining four kinds of receptors can degrade by transforming into other types. Nevertheless, metastable loops may exist to lock the cells in a certain phenotype (e.g. everlastingly proliferative). The dynamics of the whole system is thence determined by the competition among various metastable loops of cell proliferation (either normal or tumorigenic), the cell cycle arrest (either temporary or permanent arrest) and cell death.

The following paragraphs will explain one by one the rules of receptor dynamics in Table 2.2 from its biological ground.

1) Growth:

Condition: Cell grows when it is not arrested and the sum of growth and adhesion receptors below a level of R_M, which corresponds to the minimal physical mass required for cell division. This is to ensure that the cell has synthesized a sufficient quantity of materials for performing the mitotic program. The "materials" required for mitosis can be represented by the summed amount of growth and adhesion receptor.

Behavior: *Grow*. This cellular stage is G1, during which the cell mass increases and growth receptors along with ECM are synthesized.

Receptor dynamics: Each newly born cell is assigned with a growth receptor amount B. When it grows, growth receptor amount $R_g(t)$ increases at the rate γ, which is a uniformly homogeneous concentration of growth factors. Meanwhile, ECM is synthesized around the growth receptors and degraded around other receptors, hence $E(t)$ linearly increases with $R_g(t)$ at the rate s_1 while it decreases with other types of receptors at the rate s_2. Accordingly, a larger growth rate γ yields a larger $R_g(t)$ and a larger $E(t)$, in accord with the fact that ECM serves as a local storage of growth factors [50]. Moreover, the growth rate γ compared with R_M -B controls the time resolution of DRDM. In the following simulations, it takes roughly 5 steps for a cell to divide using the parameters in Table B1 in Appendix B(1), implying that one step *in silico* corresponds to several hours in real time because, in real world, cells usually have a doubling time around 20-30 hours in vitro[51].

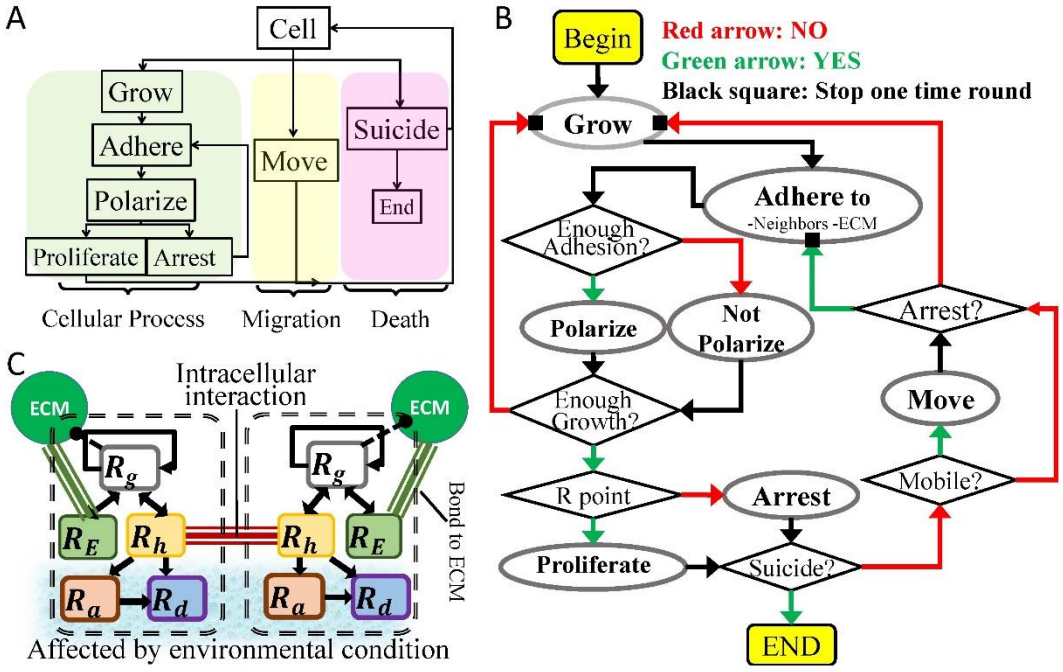

Figure 2.1 Model construction of DRDM. (A) Three modules of cell behaviors in paralleled execution during each time step. (B)The flowchart of the single cell behaviors at one step of time iteration: circles represent the cell behaviors and the diamonds the checkpoints. All cells begin from *Grow* function (either born by the mother or seeded into the space); at time steps other than the first round, the cell starts from either *Grow* or *Adhere* function according to the state where it finishes in the last iteration. The cell executes cell behaviors in the sequence shown by the flowchart until it reaches the black squares, which is the terminal of this round. If the cell chooses to die, the life of this cell along with all the processes will end. (C) The transformation among five kinds of receptors of two interacting cells. The synthesis rates of arrest and death receptors are subject to environmental conditions (refer to Table 2.1).

2) Adhere:

Condition: None.

Behavior: *Adhere* to neighboring cells and ECM.

Receptor dynamics: First, adhering to neighbors needs a transformation of some growth receptors into adhesion receptors (or turning back into growth receptors when cell-cell adhesion is lost), depending on the sizes of two cells [see Appendix A(1)]. The essence of this intercellular adhesion lies in that larger cells which have larger adhesive surface need more adhesion receptors. The second part of *Adhere* function refers to the cell-ECM adhesion**,** by which some amount of growth receptor continuously transforms into ECM receptors which are adhesive to ECM. The amount of ECM receptor $R_E(t)$ is proportional to the amount ECM $E(t)$ with a factor $1/e_{scr}$ [see Appendix A(2)]. The formation of ECM receptors may stimulate a negative feedback to the cell growth because large $R_E(t)$ increases the tendency of cells to polarize [see 3) Polarize]. However, if the ECM threshold e is too high, meaning that the cell is very insensitive to ECM and allows an enormous amount of R_E transformed, then the polarization and the subsequent cell cycle arrest will not easily occur. These modeling details of cell-ECM interaction are related to some experimental observations: a detachment from ECM ($e_{scr}\rightarrow\infty$) yields uncontrollable growth; a mild adhesion to ECM (a low e) induces the cell into cell cycle arrest and a strong adhesion to ECM (a high e) promotes cell proliferation [52].

3) Polarize:

Condition: For apical polarity, the epithelial cell needs sufficient apical junction complexes engaged with both lateral contact (adhesion between cells) and basal contact (adhesion between the cell and ECM) [53]. Therefore, the cell should have $R_h(t)$ and $R_E(t)$ with respect to their thresholds p and e for cell polarization.

Behavior: *Polarize*. Cell polarization blocks the growth-inducing signals and ceases apoptosis [53,54], hence the accumulation of death receptor is halted while the cell is prepared for cell-cycle arrest.

Receptor dynamics: If the cell is polarized, it accumulates arrest receptors $R_a(t)$ by transforming some adhesion receptors at a fraction $a_{scr,}$ which is a growth inhibiting factor; if the cell depolarizes, it transforms adhesion receptors into death receptor amount $R_d(t)$ by a fraction d_{scr}, which is a death-inducing factor. Both a_{scr} and d_{scr} embrace the information about the unfavorable environmental conditions to the cell vitality, such as the lack of nutrients or the existence of fatal toxicities.

4) Restriction point:

Condition: Comparing the amount of arrest receptor $R_a(t)$ with arrest threshold a. For a growing cell turning into a quiescent stage G0, $R_a(t)$ must exceed its threshold a; for a growth-arrested cell to reenter the growing stage G1, it not only needs $R_a(t)$ below

a, but also the growth receptor amount $R_g(t)$ above its threshold *g*.

Behavior: *Restriction point* is a checkpoint for cell cycle arrest. Arrested cells can emerge as *temporarily arrested* or *permanently arrested*. Temporarily arrested cells are revocable if the local conditions favor cell growth once again. However, if unfortunately, the cell's growth receptors have been degraded to a quantity below the threshold *g*, it will become muted and be not responding to any cycle-related signals. Meanwhile, if the cell-cell or cell-ECM adhesion decreased due to the loss of influx of growth receptors, the cell may depolarize and some arrest receptors and adhesion receptors will transform into death receptor by a fraction d_{scr} [refer to 3) Polarize]; during this process, the cell may die of excessive death receptors. This mechanism means that cell cycle arrest has a limited time window, out of which the arrested state become permanent (not considering some external stimuli are brutally operated to activate the cell).

To mention, arrest receptor is only a conceptual representation of the aggregated growth-inhibiting signals and it does not exist in real cells. In IBcell, transitions between growth and arrest are controlled by a single parameter (equivalent to the growth threshold *g* in DRDM). The reason of arrest receptor being here is that many growth-inhibitory signals through specific pathways, the deprivation of nutrients, contact inhibition, DNA damages, and among other [55] can exist independently of growth receptors. In the DRDM, the arrest receptor is the "effective receptor" that unifies these various growth-inhibiting signals. Such separated two-way functions of *Restriction point* enables the realization of the asymmetry between G1 to G0 and G0 to G1, processes, the former of which is controlled solely by arrest threshold *a*, and the latter of which by both arrest threshold *a* and growth threshold *g*, agreeing with the fact that the G0 to G1 processes can be much slower than the G1 to G2 ones [56].

Receptor dynamics: None. The cell state is changed from cell growth to cell cycle arrest.

5) Proliferate:

Condition: The cell is not arrested and the total cell mass (the summed amount of growth, adhesion and ECM receptor) exceeds R_M.

Behavior: Giving birth to a new daughter cell in the empty neighboring site. Multi-stage processes (such as S phase, G2 checkpoint, M phase, etc[57]) are involved in real cell division but in DRDM (also as in IBcell), cell division is only a simple event of one cell splitting into two at a time step.

Receptor dynamics: The mother cell assigns a basic amount of growth receptor *B* to its daughter, who inherits the genotype *T* from the mother (the inheritance of genetic information is trivial when *T* is homogeneously constant in Ch.2.2, whereas it is non-trivial to the system in Ch 2.3 where mutation strategies are involved). The proliferative cell must find an empty neighbor to lay its daughter, and if not, the cell keeps proliferative and wait until cell cycle arrest ensues or it dies. This waiting state of

proliferative cells is different from the quiescent state abovementioned in that the waiting proliferative cells still have the *Grow* function switched on whereas quiescent cells do not. Hence, these waiting proliferative cells are called tumorigenic cells hereafter because of their eminent features of keep growing uncontrollably, which is one of the hallmarks of cancer cell [58].

6) Suicide:

Condition: The death receptor exceeds death threshold d.

Behavior: A cell can basically die in a necrotic or an apoptotic way, the former of which is induced by the exogenous fatal environment and the latter of which is an endogenous sacrifice for the tissue vitality. In DRDM, there is no distinction between necrotic and apoptotic cell death and the death receptors represent all the internal and external cues against cell survival. The death receptor can be transformed from adhesion receptors only if the cell is not polarized. This is compatible with the observation that the propensity of cell death is higher when it is far from being arrested [59].

Receptor dynamics: All receptor amount $R(t)$ and ECM amount $E(t)$ become zero at the instantaneously.

7) Move:

Condition: The total amount of adhesion receptor and ECM receptor stays below a threshold h.

Behavior: Cell chooses an empty neighboring node with minimal surrounding ECM amount to move. Normally, cells can migrate through chemotaxis or haptotaxis while conjunct with basal stroma and other cells [60]. Chemotaxis is not modeled in the current DRDM model because the micro-environment is homogeneous in space. Therefore, *Move* function in DRDM only involves haptotaxis, in which cells migrate downward along the adhesion gradient by the tensile forces to be mechanistically balanced [60,61]. This serves as a simplified rule corresponding to the complex fluid dynamics in IBcell model. The principle of the mechanical balance is as such: the compression from surroundings felt by each cell at node i can be represented by the total ECM amount of all the surrounding cells and then the compression C_i is formulated as:

$C_i(t) = \sum_{j \in N} E_j(t)$, where N is the set of neighboring sites.

Clearly, the cells struggle with local adhesive forces under the repulsing compression from surroundings. If the cells live a weak adhesion culture, they should diffuse from a site with high compression to a site with lower compression.

Receptor dynamics: Suppose that a cell at site i is surrounded by several vacant neighboring sites, which are denoted as a set K. The cell can migrate to the vacant neighbor k only if $C_k < C_i$ and $C_k = \min(C_{j\in K})$. The information of receptors, ECM, and thresholds of k is copied from that of n and this information is then deleted at n.

Table 2.2 Cell behaviors corresponding to the discrete receptor dynamics in DRDM.

Conditions	Cell Behaviors	Receptor Dynamics	
$R_g(t)+R_h(t) < R_M$ AND not arrested	*Grow*	$R_g(t+1)=(1+\gamma)R_g(t)$ $E(t+1)=E(t)+s_1R_g(t)-s_2[R_h(t)-R_a(t)+R_d(t)]$	
None	*Adhere*	$R_h(t+1)=\mathrm{AD1p}[R_{\mathrm{neighbor}}(t), R_g(t)+R_h(t)]$ [Appendix A(1)] $R_E(t+1)=E(t)/e_{scr}$ [Appendix A(2)] $R_g(t+1)-R_g(t)=R_h(t)+R_E(t)-R_h(t+1)-R_E(t+1)$	
$R_h(t) \geqslant p$ AND $R_E(t) \geqslant e$	*Polarize*	$R_a(t+1)=R_a(t)+a_{scr}R_h(t)$ $R_h(t+1)=(1-a_{scr})R_h(t)$	
$R_h(t) < p$ OR $R_E(t) < e$	*Depolarize*	$R_d(t+1)=R_d(t)+d_{scr}[R_h(t)+R_a(t)]$ $R_h(t+1)=(1-d_{scr})R_h(t)$ $R_a(t+1)=(1-d_{scr})R_a(t)$	
Not arrested: $R_a(t) \geqslant a$	*Restriction point*	Entry into Arrest	
Arrested: $R_a(t) < a$ AND $R_g(t) > g$		Exit from Arrest	
$R_g(t)+R_h(t) \geqslant R_M$ AND not arrested	*Proliferate*	Empty neighbor j	$R_a^j(t+1)=R_g(t+1)=B$ $T^j(t+1)=T(t)$
		No space	None
$R_d(t) > d$	*Suicide*	$R(t+1)=0, T(t+1)=0$	
$R_h(t)+R_E(t) < h$	*Move*	Move to the vacant neighboring site with least local ECM	

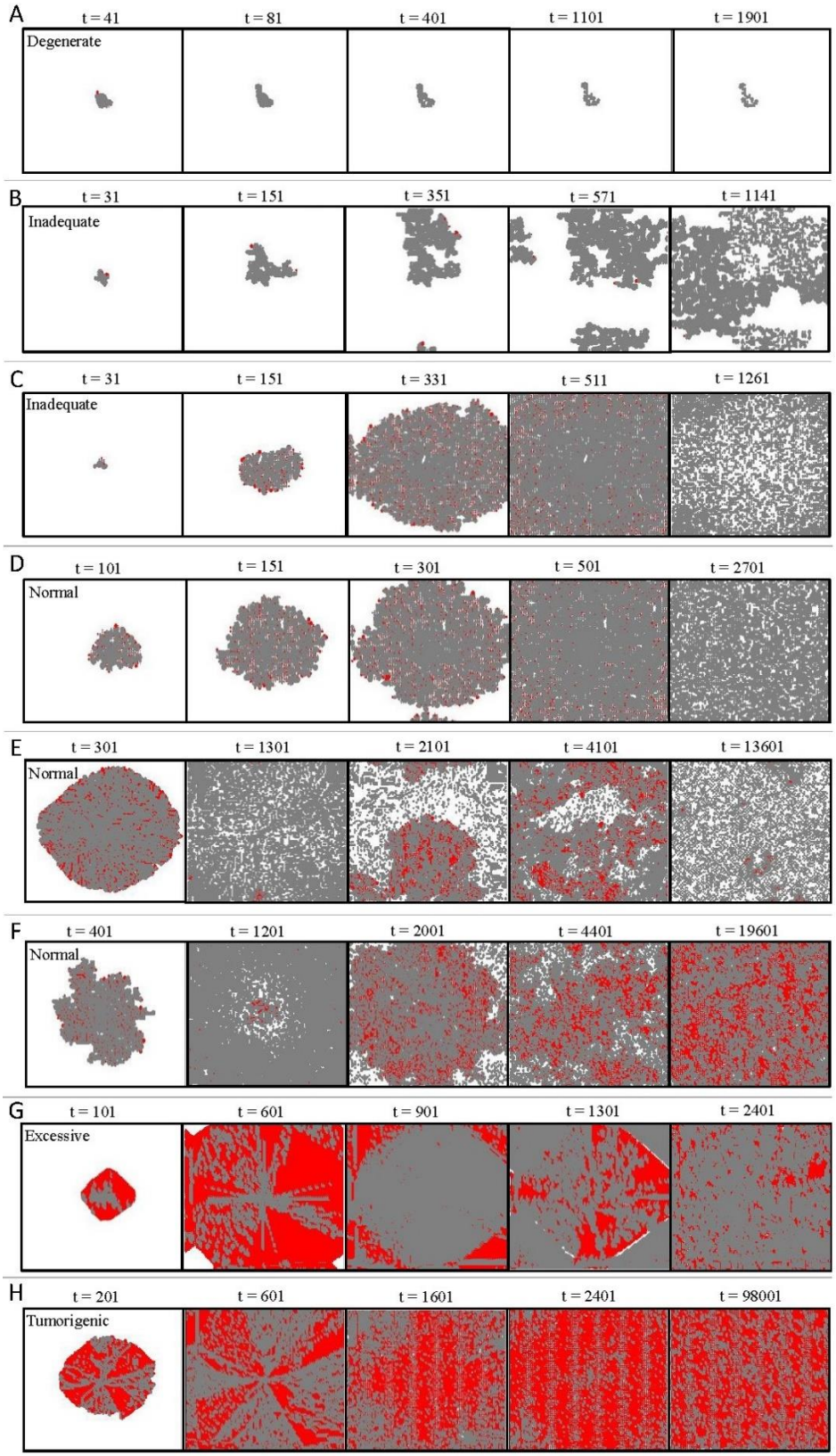

Figure 2.2 Diverse growth patterns in DRDM under different parameter settings.

2.1.2 Basic output of diverse homeostasis

The parameter settings are summarized in Table B1 in Appendix B(1). Lattice size is 71×71 with a total volume of 5041 nodes. The initial condition is to seed one growing cell with $R_g(0)=B$ to the lattice. Thresholds T, growth-inhibiting factor a_{scr}, and death-inducing factor d_{scr} are global constants to mute the effect of endogenous and exogenous homogeneity, thus enabling one to focus on the role of cellular interactions in multicellular homeostasis. Pseudo codes are presented in Appendix E.

Fig.2.2 shows the growth patterns of the system with different parameter settings. Since the fluid mechanics of ECM in IBcell has been simplified for computational efficiency, the cluster of the cells cannot appear with a spherical architecture of acinar lumens due to the lack of modeling "lowest surface tension" at the outer layer; thence multiple anomalously shaped hollows emerge. Nevertheless, morphology is only the consequence, not a cause, of the cell phenotype dynamics and in Ch.2.1.4, I will show that without the representation of morphology, the DRDM can still reproduce the various phenotype dynamics (corresponding to respective acinar morphology) and the phase diagram (i.e., the system states in a parameter space) of IBcell.

Let's inspect the snapshots in Fig.2.2 in detail. To mention, the living cells (the nodes with a non-zero number of receptors) appear as colored dots (proliferative cells as red, while arrested cells as grey), each of which has the diameter linearly related to the total receptor amounts of the cell represented. The rheology of the multicellular topology in terms of proliferative and arrested cells can define the growth pattern of the cell clusters. Degenerate morphology [Fig.2.2 (A)] is a small anomalously shaped cluster of arrested cells; a similar type is the small inadequate morphology [Fig.2.2 (B)], which can have longer expanding time, however, with anisotropic directions, and is eventually shaped as a large cluster of arrested cells with irregular outer layers and small hollows. Inadequate morphology can have another type with much regular shape [Fig.2.2 (C)] resembling the normal ones [Fig.2.2(D)] at beginning stage where the proliferative cells are evenly distributed at the outer layers; after that, the cells at the center of the *inadequate* system either die or become arrested and then the remaining cells form a large cluster of arrested cells with scattered large hollows, whereas those in the *normal* system, the newly born cells will reoccupy the hollows left by old cells and extend the life of the system. More typically, the normal homeostasis [Fig.2.2 (E-F)] shows temporarily oscillatory growth patterns after the growing cluster has occupied the whole space in fully connected topology: the system locally undergoes the cycle of growing, getting arrested, dying and being; long after these metastable cycles of life, the topological structures become more and more homogeneous with the arrested cells fully connected and proliferative cells evenly distributed. However, the longtime evolution of normal homeostasis does not last for eternity and may have bifurcated destination such as *inadequate* [Fig.2.2 (E)] and *tumorigenic* [Fig.2.2 (F)].

The system can reach tumor-like architecture without undergoing normal oscillatory growth as shown in Fig.2.2(G-H), leaving the proliferative cells dominant in the space. Oscillatory patterns can still occur as a consequence of the competition between the arrested and proliferative cells and the system may slowly form *excessive* morphology in which arrested cells win to have a fully connected topology[Fig.2.2(G)], or keeps *tumorigenic* if proliferative cells win to have a connected topology with very few of them getting arrested [Fig.2.2(H)].

One can easily observe that the *degenerate* and *tumorigenic* morphologies in DRDM have straightforward correspondence to the unstable growing and the degenerate acinar architectures in IBcell, whereas the *inadequate*, *normal*, *excessive* patterns in DRDM cannot be identified as equivalent to the hollow structure of stable acini in IBcell (a discussion has been detailed in Ch.2.1.3). The reason lies in that the DRDM cells do not intimately align to form continuous surfaces because the minimization of multicellular surface tension is not modeled. If the submodels regarding the multicellular surface tension are introduced (e.g., adding a simple rule to *Move* function: all cells must adhere to some other cells while moving), smooth surfaces of hollows (which is acini-like) can be reproduced in the DRDM (Fig.2.3). However, this modification enables a finer simulation of morphology at the sacrifice of computational efficiency (nearly a doubled simulation duration) and imposes little qualitative changes on the phenotypic population structure and on the basic characteristics of diverse homeostasis described above. One can even improve the *Move* function by introducing more sophisticated mechanisms that are comparable to the hydrodynamics in IBcell for a better reproduction of shape of hollows, which helps distinguish semi-hollowed lumens from full-hollowed lumens as in IBcell, but with a slower computation. Finally, one may notice that DRDM can only reproduce multiple "acinar structure" instead of a single lumen (as in IBcell). This discrepancy can also be solved by adding flow mechanisms of ECM if one would like to reduce the computation speed. These trivial changes brought by Move function implies that these complex subcellular details indeed can be reduced to some extent without impairing the interdependence structure lying inside the receptor dynamics.

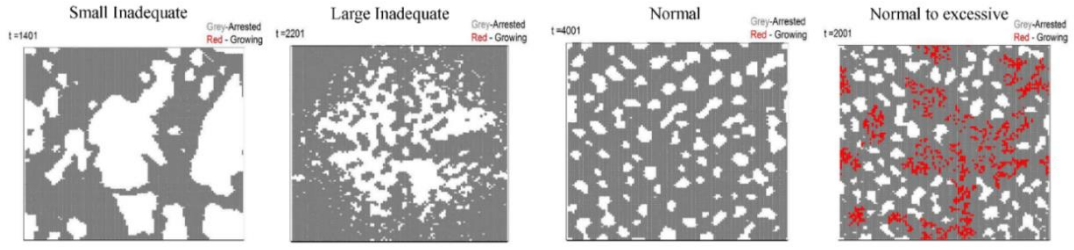

Figure 2.3 Emergence of acini-like lumens in the DRDM with a simple surface tension model and doubled simulation time. Note that the semi-lumen and full-lumen structures in IBcell are still not distinguishable with this simple modification.

2.1.3 Validation: A comparison with IBcell

As is mentioned in Ch.2.1.2 and Ch.2.1.3, the simplified fluid dynamics and the subsequent inaccurate cell morphology will not bring qualitative change to the phenomena of diverse homeostasis. This fact can be confirmed by a direct comparison between the DRDM result and IBcell result in terms of their sub-population structure. Meanwhile, only a comparison of results on short timescale is possible since the timescale in IBcell simulation is around 30 days *in silico,* which needs only several hundred of time steps in DRDM.

The only concern with the absence of inaccurate morphological results in DRDM is that one needs other indicators than morphology to describe and distinguish different system states. As is demonstrated in Ch.2.1.2, morphology is more of only the consequence rather than the cause of the phenotype dynamics, one can conceive an indicator embracing the phenotypic information. A system vitality index is then proposed in [49] as an indicator for phenotypic population structure (hereafter called phenotype structure in short). The definition of this index, denoted as V, is as follows:

$$V = w_1 N_a + w_2 N_t = N(w_1 N_a/\mathrm{N} + w_2 N_t/N) \qquad \text{(Eq. 2.1)}$$

where N, N_a, N_t are the numbers of total, arrested, and tumorigenic cells and w_1, w_2 are the coefficients weighing the contribution of the two terms. As the definition implies, three pieces of information are embraced: the total cell number, the arrested cell number, and the tumorigenic cell number, hence this index a measure of vitality of the system and the two weights can be arbitrarily selected to make this indicator a good parameter that distinguishes different states of the system. According to ref. [49], the two numbers are set as w_1=0.1, and w_1=1, based on which V ranges from zero to the size of space. Compared with the straightforward representation of morphology in IBcell, the advantage of this mathematical indicators lies in its precision, its capability of being recorded continuously through longtime simulation, and most critically, the convenience to be calculated and displayed for densely sampled parameter spaces.

The simulation results of IBcell are presented from two aspects: 1) the 2D/3D morphochart [Fig.2.4(A)] and 2) the time evolution of the population (proliferating, dying and total cells) near the critical boundary of morphochart [Fig.2.4(C)]. With the properly defined order parameter V, one can compare the phase diagram of DRDM with the morphochart of IBcell and the time evolution of the three population near the critical boundary of phase diagram in DRDM phase diagram with the population dynamics at critical regions in IBCell morphocharts.

The 2D/3D morphochart in IBcell {Fig.2.4 (A), cited from Fig. 3(D) in Ref [47]} is plotted in the space of three parameters: g^{IB}(the growth receptor concentration), d^{IB}(the death receptor concentration), e^{IB}(ECM receptor concentration). Note that both growth-to-arrest and arrest-to-growth transitions in IBCell depends solely on the

concentration of growth receptor g^{IB}, whereas in DRDM on g and a. Fig.2.4(A) shows that the different types of acinar architectures emerge in different sub-spaces of the morphochart: stabilized degenerate architecture with high g^{IB} and low e^{IB} , stabilized semi/no-lumens with high d^{IB} and low e^{IB}, tumor-like structures with high e^{IB} or low g^{IB} and the stabilized hollowed lumen sitting at the center of the morphochart.

Before comparison, the correspondence between the various morphology in IBcell to different value ranges of phenotype structure V used in DRDM simulation should be clarified. By counting the arrested, proliferative and the total cell number in IBcell acini, one may find that: $V < 250$ corresponds to a stabilized degenerate architecture, $500 < V <1500$ to semi/no- lumen acini, $V >1500$ to the un-stabilized tumor-like structures, $250 < V < 500$ to the perfect hollowed acini. The boundaries of different phases are indeed ambiguous, just as the many morphologies of acini in IBcell shown in Fig.2.4(C) is hard to be classified to any well-articulated form of structure. It should be mentioned that most morphologies in IBcell correspond to the small values of V because of a smaller total cell number.

In DRDM, the mechanism of entry into and exit from cell cycle arrest are "asymmetric", i.e., the former controlled solely by a and the latter by both a and g, Therefore, the two diagrams in the parameter space of g-d-e and a-d-e are presented [Fig.2.4(B)]. One can observe that the only difference between the IBcell morphocharts and DRDM phase diagrams is that the tumor-like acini can exist when g^{IB} is near zero in IBcell while this is not the case in DRDM. This is because $g^{IB} \to 0$ is equivalent to the situation that a approaches infinity in DRDM, which is not attainable. Yet, the trend is still observed that the domain of tumor-like morphology ($V >1500$) is expanding with a getting larger [green domain in Fig.2.4(B)], stating that the DRDM phase diagrams qualitatively agree with IBcell morphocharts.

Next, let's inspect the subpopulation dynamics for different phases around the critical boundary. The three population dynamics (proliferative, death and total) near the critical boundary of the hollowed lumen and the semi-lumen in 2D morphochart of g^{IB} and d^{IB} in IBcell are shown in Fig.2.4(C) {adapted from Fig.3 (B) in Ref.[47]}. Accordingly, the 2D phase diagram in DRDM is plotted in the space of g and d [Fig.2.4(D)], where the population dynamics near the critical boundary between the phase $250<V<500$ and the phase $500<V<1500$ are presented. Similarly to the population dynamics in IBcell, the total cell number (the black line) and proliferative cells (the light green line) increases at the first stage, after which they decrease due to the emergence of dying cells (the red line). If the cells at the center of clusters die out quickly (lower d^{IB} or d), the multicellular structure appears as a hollowed lumen [refer to the inset 1 in Fig.2.4 (C) and (D)]; if the cells at the center of the cluster do not die quickly enough (due to a higher d^{IB} or d), these cells will become arrested in the center, yielding in semi- or even no-lumen structure [refer to inset 2 in Fig.2.4(C) and (D)]; if newly born proliferative cells reoccupy the space left the dying cells due to a lower g^{IB}

or *g*, an unstable and tumorigenic acinar structure tends to appear [refer to inset 3 in Fig.2.4(C) and (D)]. In short, the similar population dynamics in two models emerge in the same parameter zones around the critical boundary.

A small discrepancy is that cells gradually die in the DRDM whereas, in IBcell, cells die at the same time point. This may be explained by the difference in the system size (or the total cell number). By increasing the death accumulating rate d_{scr}, one can modulate the total cell number in DRDM to a level around 300, which is the characteristic acini volume in IBcell, and the DRDM cells can die in synchronization [inset 4 in Fig.2.4(C) and (D)].

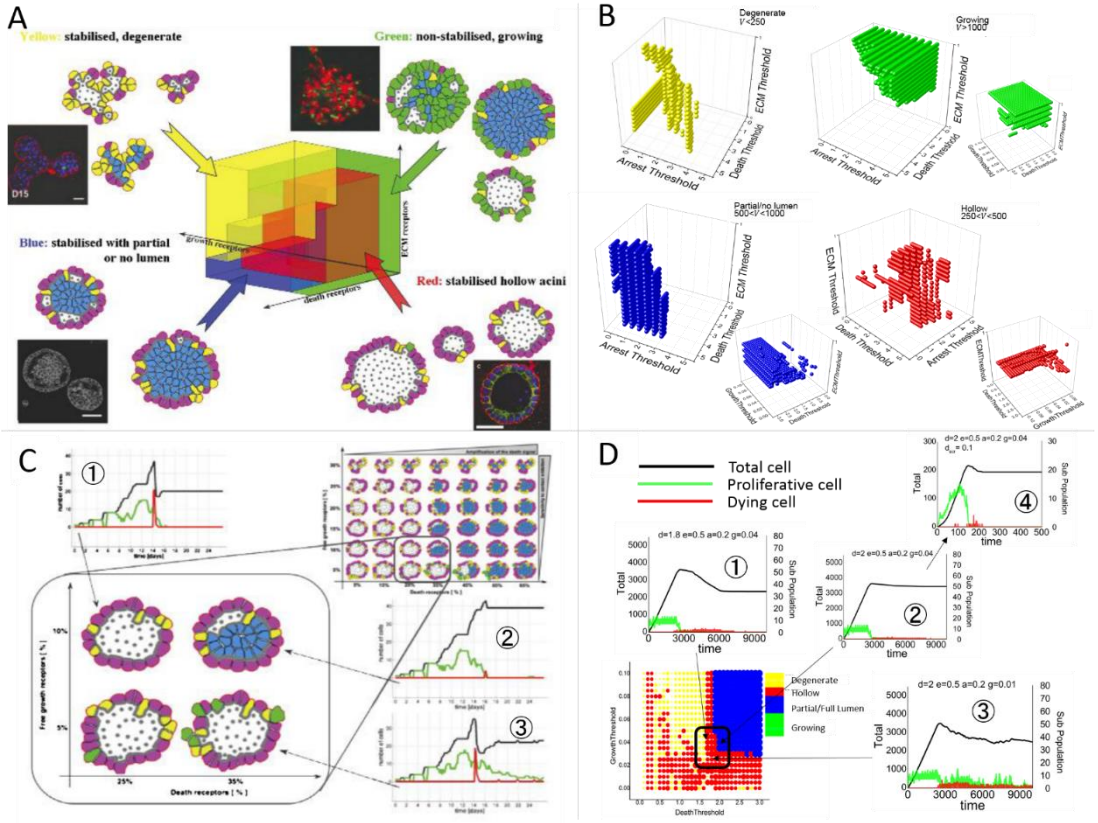

Figure 2.4 A validation of DRDM by comparison with IBcell. (A) The 3D morphochart of IBcell (Fig.3 (D) in Ref[47]) with four distinctive acini architectures emergent from four different subspaces of morphochart. (B) The phase diagram in DRDM simulation with four different ranges of *V* emergent from four different subspaces of the diagram. (C) Population dynamics of proliferative, dying and total cells near the critical boundary in the 2D morphochart from IBcell (Fig.3 (D) in Ref[47]). (D) Population dynamics of proliferative, dying and total cells near the critical boundary in a 2D phase diagram from DRDM simulations.

2.2 Non-mutational homeostasis *in silico*

The short timescale observation has validated that DRDM still keeps the power of reproducing the phenotype dynamics in IBcell even with no modeling of fluid mechanics. Now, a longer simulation and large-ensemble statistical analysis can be implemented with DRDM due to its computational efficiency.

2.2.1 Longtime evolution of DRDM

Cells cooperating through the fluctuation of receptor configurations yields the self-organization of diverse homeostatic growth patterns (as seen in Fig.2.2), some of which have very long periods before reaching the stationary patterns. The system trajectories of these growth patterns described by the compositional proportion of arrested cells N_a/N in relation to the total cell population N/N_{max} (N_{max} is the lattice size) have been presented in Fig.2.5(A).The arrows point to the time direction. Not only do these evolutionary trajectories have diverse paths, but also do they show non-trivial longtime behaviors, especially for *inadequate* (red), *normal* (dark yellow and blue) and *excessive* (green) growth patterns, whose trajectories can be trapped into some local quasi-stable orbits before reaching the final states.

These longtime behaviors can also be illustrated by the time evolution of N_a/N [Fig.2.5(B)] under various values of the critical parameter e (ECM threshold). For e approaching some critical value [Fig.2.5 (B1)], the arrested population percentage at

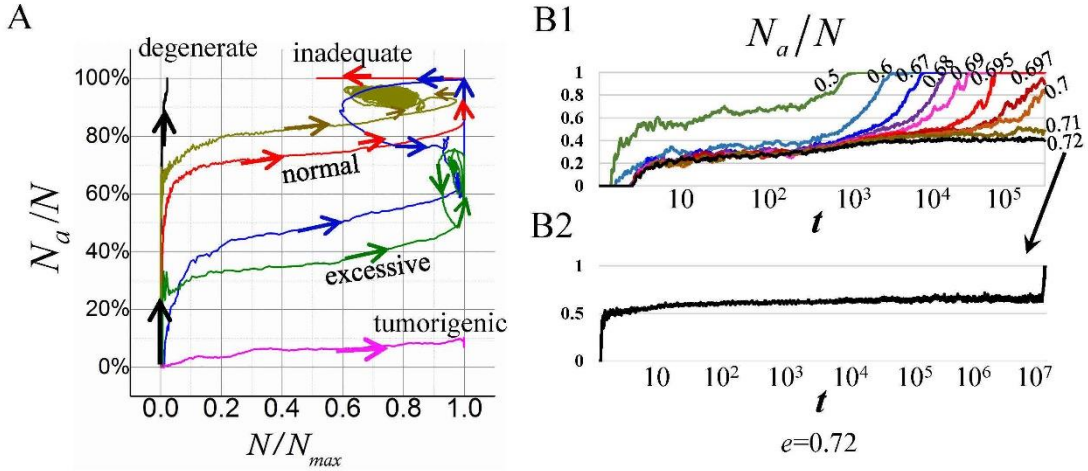

Figure 2.5 Longtime evolution of homeostasis. (A) System trajectories on the time log of arrest population percentage N_a/N versus total cell population N/N_{max}. (B) Longtime evolution of arrested cell population as the control parameter e approaching its critical value, from 0.5 to 0.72(B1) and 0.72(B2). Time is denoted as t and one time step corresponds to about 5 hours in real time according to the current parameter settings of B, R_M and γ.

early stage (t <10^3) will decrease with e (implying a shift in growth pattern from *degenerative* to *inadequate* or *normal* patterns) but the final stationary state at t <10^3 is still degenerate [refer back to the growth pattern in Fig.2.4 (E)]. Another difference among these states lies in the time length of the non-degenerative quasi-stable plateaus, during which these homeostatic structures evolve steadily and slowly without reaching degeneration. If e is sufficiently close to its critical value [Fig.2.5 (B2)], the quasi-stable plateau becomes extremely long.

Table 2.3 Meaning of different colors in phase diagram of V in Fig.2.6

State	V	Color map
Tumorigenic	>4000	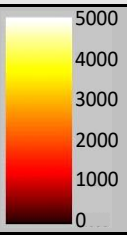
Excessive	3000-4000	
Normal	1500-3000	
Inadequate	250-1500	
Degenerate	<250	
(including Extinction)	0	

2.2.2 Quasi-stable homeostasis and phase diagrams

To better probe the quasi-stable homeostatic evolutions in DRDM, I proposed another two order parameters besides the phenotype structure *V:* cell average proliferation time and the relaxation time. The control parameters of the three-dimensional (3D) phase diagrams are death threshold *d*, ECM threshold *e*, and arrest threshold *a*, as they are mostly investigated in the literature [51-58] and these three are also the control parameters used in IBcell morphochart. The death threshold *d* is inversely related to the tendency of cell death, the ECM threshold inversely related to sensitivity to ECM, and the arrest threshold inversely related to the propensity to cell cycle arrest. See other parameters Table B1 in Appendix B(1).The model robustness regarding the variations of some other important parameters like the thresholds *p, h, g* will be discussed in Ch.2.2.4.

1) Phase diagram of V

The definition of V has been demonstrated in Ch. 2.1.4 (Eq.2.1). The meaning of the colors in the phase diagrams in Fig.2.6(A-C) is elaborated in Table 2.3, where a qualitative mapping between the general classes of growth patterns (termed as “state” hereafter) and the ranges of V is exhibited. Again, the boundaries among these states are ambiguous in terms of the value of V and this classification is proposed just for the conciseness of demonstration. One can also relate these states to the exemplary morphological outputs in Ch.2.1.2 to have an intuition on their growth patterns in the2D real space.

Basically, one may find that the total parameter space can be dissected into several subspaces with similar color and these subspaces are recognized as different "phases" of homeostatic states in the diagram [Fig.2.6(A)]. An interface separates the phase (in dark colors) of the *degenerate* and the *inadequate* states from that (in light colors) of the *excessive* and the *tumorigenic* states. The *normal* states (in orange and red colors) are located near this interface [bottom panels in Fig.2.6(A)]. Meanwhile, the color of sub-spaces embracing *inadequate*, *normal* and *excessive* states mildly changes with time [comparing the left panels with the right panels in Fig.2.6 (A)]. An explicit illustration of this mild time-dependent change in the phase value can be seen from Fig.2.6 (B1-B3), where only the sub-spaces of normal states (orange-red) at 5×10^3 time steps are shown. These normal states at an early time will gradually split into the two clusters of phases, tumorigenic (white), or the degenerate (dark red), over a large timescale of 10^6 steps, and the sub-space of the normal states shrinks over time. By contrast, the region of the excessive and the tumorigenic states are expanding, because the total value of V summed across the subspace of these states (V >3000) becomes larger through the time [Fig.2.6(B3)].

The roles of three thresholds contributing to different homeostatic phases can also be understood. Both a low value of ECM threshold e and a low value of arrest threshold a correspond to a formation of degenerative phase; A high e (>0.6) along with a low death threshold d (<1.5) contributes to the *tumorigenic* phase; A higher arrest threshold a(>0.5) with a higher d (>2) falls into the *inadequate* phase and with lower d (<2) yields an *extinctive degenerate* phase, whereas a lower a (<0.5) with lower d(<1) is non-extinctive degenerate states . Standing narrowly besides the critical interface is the *normal* phase, in which the subspace closer to a high e has the tendency to become *tumorigenic* and that closer to a low a undergoes degeneration. Also, e larger than 0.8, which implies a strong cell-ECM adhesion, saliently ensures the emergence of the tumorigenic states as shown in Fig.2.6(B3), in accord with the findings in the literature [52].

2) Phase diagram of A

Fig.2.6(C) shows the phase diagram of cell proliferation age A, which measures how many times a cell has divided averaged across all the cells living in this system at a specific time. If the $A(t)$ decreases with time t, the system is undergoing "rejuvenation", whereas the system is aging if $A(t)$ increases through evolution. Like the phase diagram of V, the phase diagram of A also shows several subspaces with similar colors, which are blue (relatively small A, young), light green and cyan (medium A, mature), and yellow or red (relatively large A, old) [Fig.2.6(C)]. Note that the phase of extinctive degeneration (all cells have died) is not colored for a clarity of presentation. Also the phase diagrams are plotted for two distinctive time steps, 5×10^3 and 5×10^5, the comparison between which reveals that a part of young phase is rejuvenating (blue

turning into violet) and a part of old phase becomes even more aged through time (yellow turning into red or red turning into dark red). The phase of mature systems, sitting at the critical interfaces between different phases, may have two subspaces: the aging one (green turns into yellow) and the rejuvenating one (green turns into light blue). Moreover, comparing the structure of phase diagram of *V* and *T*, one may easily find that the phase of old systems in Fig.2.6(C) locates where the phase of *inadequate* states appears in Fig.2.6(A), and the phase of young systems resides in the phase of *tumorigenic* states.

3) Phase diagram of *T*

As one may notice, some subspaces in the phase diagram of *V* and *A* evolve with time slowly until they reach the stationary states while others do not. Hence the time *T* over which the quasi-stable states can last, or in other words, the "relaxation time" for the system reaching a final stationary homeostasis is also another order parameter for distinguishing different types of homeostatic states. Fig. 2.7 shows the phase diagram of the relaxation time *T* with the upper limit of the simulation time preset as 10^8 time steps for saving the computational resource, so relaxation time larger than 10^8 will be recorded as 10^8 in the phase diagram.

The relaxation time *T* is measured as the minimal time *t* satisfying:

$$\left|\bar{A}(\tau)-\bar{A}(\tau/2)\right|\le\varepsilon,\text{for } t\le\tau\le t+\log t^{-\varepsilon} \qquad \text{(Eq.2.2)}$$

where $\bar{A}(\tau)$ is a moving average of *A* in a time window from $\max(\tau-l,0)$ to τ with the ideal window length *l*, and ε is an infinitesimal value ($\varepsilon\to 0$) as a criterion for "stationary state". Eq.2.2 means that if a system's age has a small enough change ε in the following sufficiently long time $\log t^{-\varepsilon}$, i.e. there is no aging or rejuvenating processes, the system is considered as stationary. In Fig.2.6(D), the time window length *l* is 10^4, which is the characteristic timescale of the systems need to reach a quasi-stable stage and ε is chosen as 10^{-3}. If *T* is not found with Eq.2.2, then the system will be denoted as $T=10^8$ for plotting the phase diagram. Therefore, the blue dots in Fig.2.6(D) with $T\in(10^7,10^8]$ include the systems that have not yet reached the stationary states. Once again, the phase separation of *T* appears by their characteristic orders of scales and each phase seems to have corresponding parts in the phase diagrams of *V* and *A*. Ch. 2.2.3. will further elaborate this correspondence among three phase diagrams.

4) A 2D phase diagram

For better observing the structure of the phase diagrams, one may inspect the two-dimensional (2D) phase diagram with *a* fixed. Fig.2.6(E) shows a 2D phase diagram integrating both the information of *V* and *T* in the space of ECM threshold *e* and death threshold *d* at three levels of arrest threshold *a*. The color of the cubes describes *V* based on the colormap in Table 2.3 and the size of the cubes describes *T*. Although the 2D

diagrams have sophisticated changes under different *a*, one may still figure out the skeleton of the phase diagram [the right-bottom figure in Fig.2.6(E)]. Basically, two boundaries (the thick black lines) separate three main phases, phase X with smaller *V*, phase Y with larger *V*, and phase *S* with large *T* (implying slow dynamics). In each main phase, there exist several sub-phases with ambiguous boundaries (the thin dashed lines). To detail, Phase X is composed of the *extinct* (X1), the *degenerate* (X2) and the *inadequate* (X3) states; Phase Y consists of the *normal* (Y1), the *excessive* (Y2) and the *tumorigenic* (Y3) states; phase S, consists of the *inadequate* (S1), *normal*(S2) and *tumorigenic*(S3).

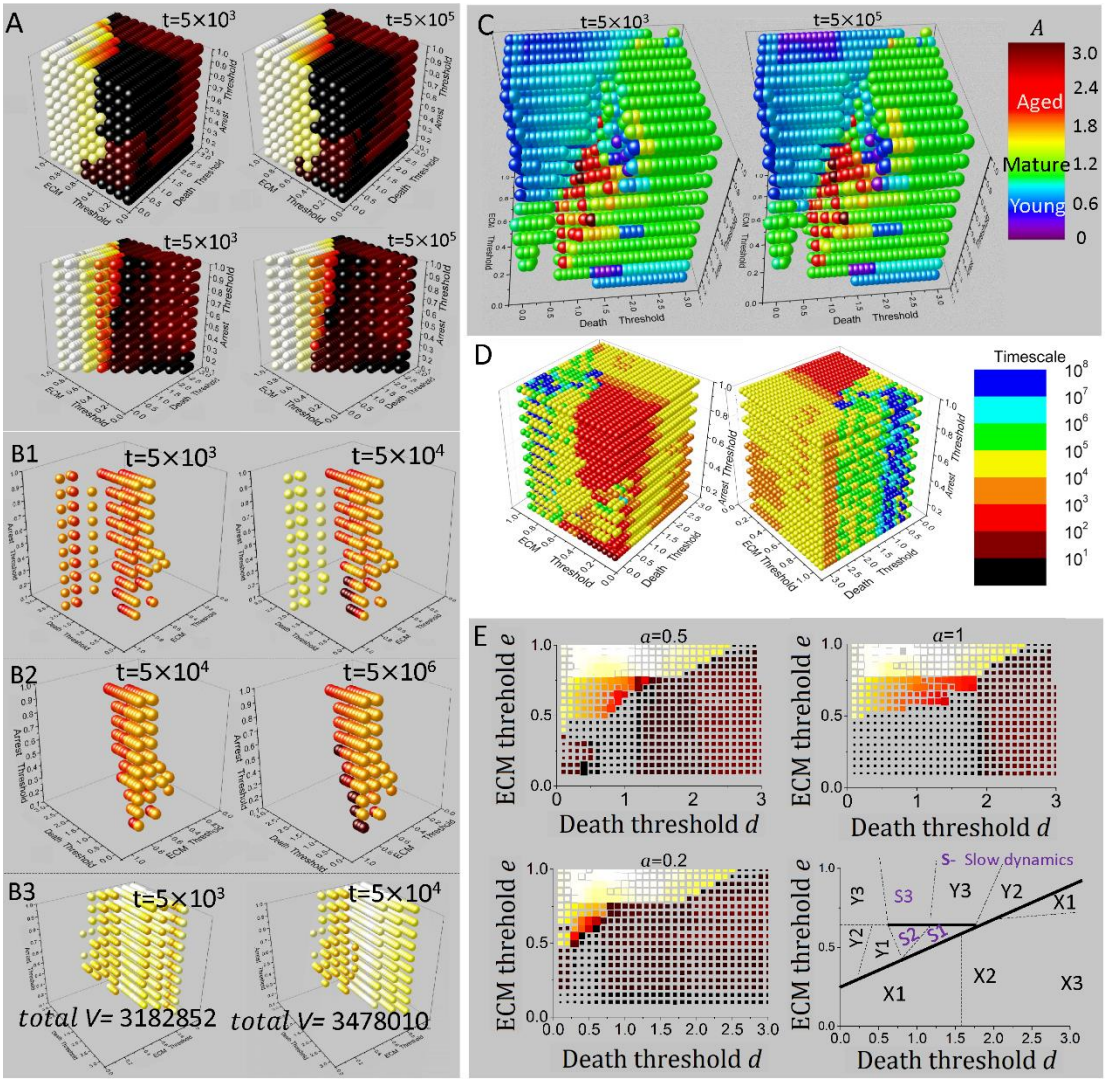

Figure 2.6 Phase diagrams of *V*, *A*, *T*. The colormap for (A),(B) and (E) are presented in Table 2.3. (A)3D Phase diagram of *V* at two different time points. (B) Bifurcation of normal systems over long time. (C) 3D Phase diagram of *A* at two different time points. (D) 3D Phase diagram of *T*. (E) 2D phase diagram of *V* under different *a* and a summarized sketch.

2.2.3 Correspondence among three order parameters

As is mentioned, the separated phases in the diagrams of *V*, *A*, and *T* have some correspondence. By a rough observation, one can relate the *degenerate* (or the *tumorigenic*) phase in Fig.2.6(A) to the *aged* (or the *young*) phase in Fig.2.6(C). Moreover, the phase of large *T* [the phase S in Fig.2.6(E)] seems to correspond to the *normal* and *mature* phases. One also can examine the correspondence of *V*, *A*, and *T* from a dynamical point of view. This correspondence can statistically stand out if the simulation results in the whole parameter space are re-organized into the space of *V*, *A*, and *T*.

Fig. 2.7 presents the relationships among the trend of *V* (denoted as $\delta V/V_0$, where V_0 is the system size), the trend of *A* (denoted as $\delta A/A_T$, where A_T is the system age measured at *T*) and the relaxation *T*. The variation of *V*, i.e., δV, is calculated as $\delta V = V(T) - \bar{V}$, where $\bar{V}$ is an average of *V* over the time window from max($T-l$,0) to *T*; similarly, the variation of *A*, i.e., δA, is calculated as $\delta A = A(T) - \bar{A}$, where $\bar{A}$ is an average of *A* over the time window from max($T - l$,0) to *T*. Here the window length *l* is again 10^4.

In Fig.2.7(A), the data points in the positive zone of the vertical axis, i.e., $\delta V/V_0>0$, represent the systems evolving towards the *tumorigenic* states, while those in the negative zone, i.e., $\delta V/V_0<0$, represent the system evolving towards *degenerate* states. The color of the data points represents the change in system age, with the blue or violet standing for rejuvenation and the yellow or orange for aging. The system's stationary age A_T is invalid when all the cells have died so the $\delta A/A_T$ for *extinctive* sates will be given a specified value "-1", which is far smaller than that of a rejuvenating process and colored in grey. Basically, one can find that *extinctive* systems have the shortest relaxation time nearly around 10^3 time steps and feature a degenerative process before

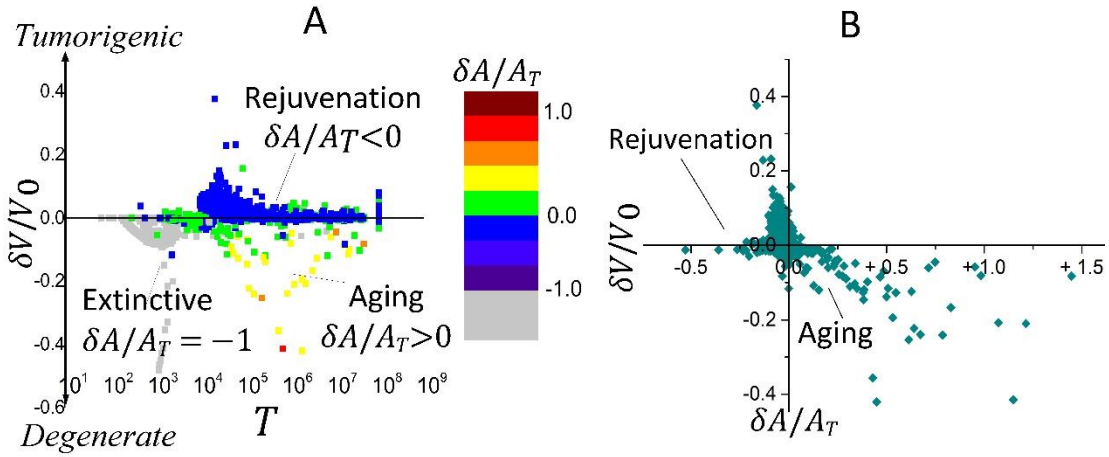

Figure 2.7 The correspondence among three order parameters: The relationship (A) between the trend of *V* ($\delta V/V_0$) and relaxation time *T* and (B) between $\delta V/V_0$ and the trend of *A* ($\delta A/A_T$).

getting *extinct*. *Tumorigenic* processes ($\delta V/V_0>0$) tend to accompany the rejuvenating process (blue) with a large spectrum of relaxation time T; by contrast, non-extinctive *degenerate* evolutions are all undergoing aging (yellow and orange). Both tumorigenic and degenerate evolutions have a large spectrum of relaxation time T implying that some of these evolutions may appear very slow [see Fig.2.6(E)]. Fig.2.7(B) exhibits the relationship between $\delta V/V_0$ and $\delta A/A_T$, and one can clearly see the negative correlation between them.

These statistical discoveries reinforce the conclusions drawn in Ch.2.2.2 that the systems can have quasi-stable plateaus in phenotype structure $V(t)$ and age $A(t)$, and the normal systems sitting near the critical states can evolve into two divergent terminations, tumor (accompanying with rejuvenation) or degeneration (accompanying with aging). These results also naturally suggest that the origin of the tumorigenesis and aging at the multicellular level may lie in some critical interdependence structure of homeostasis formation with no regard to the environmental stresses or mutational malfunctions.

2.2.4 Robustness

The longtime results abovementioned is obtained in the phase space of e, a, and d. One should also be cautious about the influence brought by other important parameters to the current conclusions. As shown in Table B1, there are many parameters in the DRDM, and with the dimensionless analysis, other non-reducible parameters other than e, a, d are the adhesion threshold h, the polarization threshold p, and the growth threshold g. Fig.2.8 shows a comparison between the control parameter setting (used in Chs.2.2.1-2.2.3) and other three groups of parameter settings wherein the growth threshold g, adhesion threshold h, and polarization threshold p are varied respectively. All four groups fix the arrest threshold a as $0.5R_M$.

Fig.2.8(A) shows the histogram of phenotype structure V binned to five ranges (corresponding to *degenerate*, *inadequate*, *normal*, *excessive* and *tumorigenesis* as described in Table 2.3) plotted at the time of 5×10^3 steps when the quasi-stable homeostasis has just emerged. The data of V is collected from the whole parameter space of d ($0< d <3$) and e ($0< e <1$). The diversity of homeostasis exists for all four groups but the phase with low V (< 250) shrinks for g=0 or even disappear for p = 1, implying that a low g (no regrowth barrier) and a high p (low tendency for cell polarization) promote the growth of system at the early stage.

Fig.2.8(B) shows that the frequency distribution changes from 5×10^3 to 5×10^6 steps, with a substantial decrease in the frequency of *inadequate* systems (30% to 50%) and a slight decrease in that of *normal* systems (2% to 4%) for all groups. Meanwhile, the frequency of *degenerate* systems soars by 30% to 60% and that of tumorigenic systems by 2% to 4%. Yet some subtle differences between the control and the variation groups can also be recognized in the inset of Fig. 2.8(B): all three variation groups have

a higher frequency of the *tumorigenic* states than the control group, which indicates the roles of strong cell motility (high h), strong regrowth ability (low g) and weak polarization (high p) in increasing the tumor incidence.

Fig.2.8(C) displays the static correlation between phenotype structure V and relaxation time T with the simulation time truncated at 10^6 steps; in all groups, the relaxation time spreads over a large spectrum from 10^4 to 10^6. The robustness of the main conclusions in Ch. 2.2.2 is proved to a certain degree. Nevertheless, the groups with low g and high p have much longer relaxation times for the data clusters with extremely low values of V, implying that strong growth signals and weak polarization can postpone the onset of degeneration or aging process.

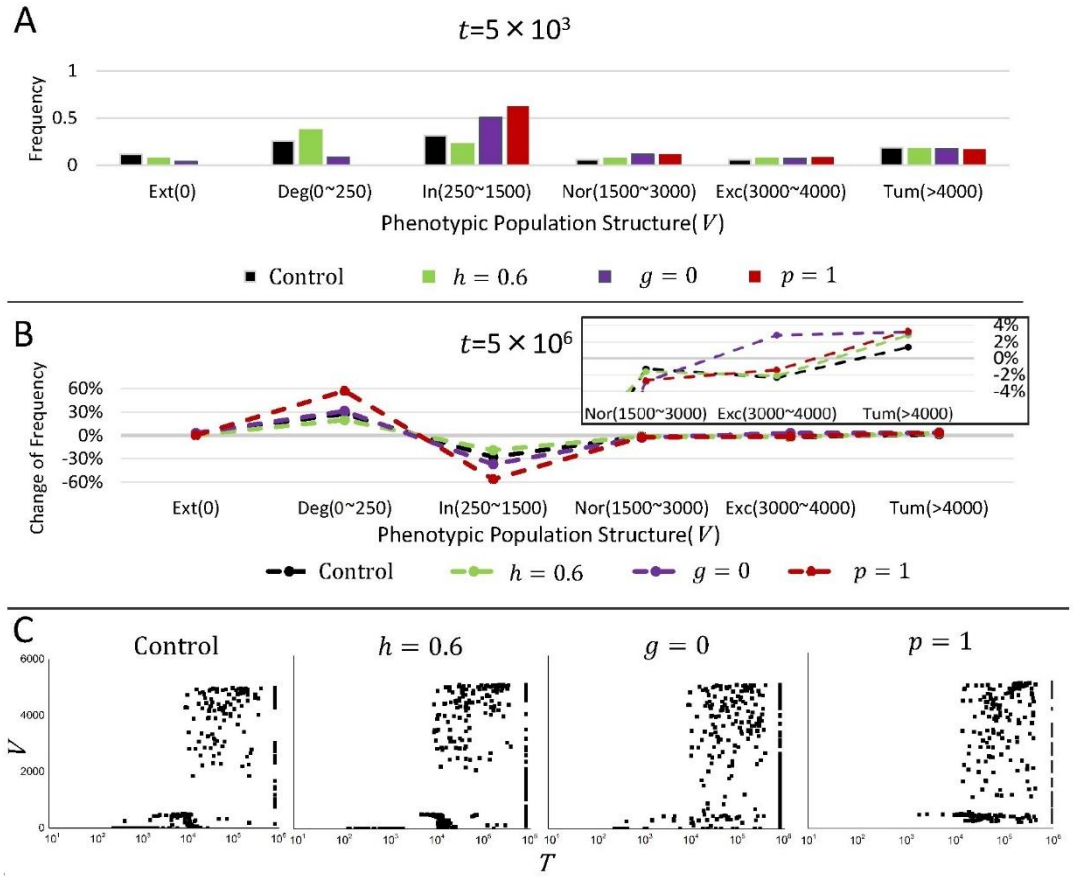

Figure 2.8 The robustness test under the variations of the other important thresholds h, g, and p. (A) Histogram of the phenotype structure at a short time. (B) Change of distribution frequency at a larger time. (C) The static correlation between V and T.

2.2.5 Discussion: a glass transition point of view

Cell replicative senescence characterizes the aging in tissues [63]. One on hand, macroscopic statistics and microscopic molecular mechanisms elaborate that cancer generally coincides with aging [64]. However, other experimental evidence reveals that anti-aging signaling induces cancer, showing an antagonism between aging and cancer [65]. In the DRDM, replicative senescence is modeled by the cells permanently falling into cell cycle arrest and is quantified by the increase in the system age A during degenerative processes. The longtime simulation results suggest that both cancer and aging are two bifurcated trajectories developed slowly from a *normal* phase which has an appropriate phenotype structure at an earlier stage of system evolution. This common origin of cancer and aging provides an explanation for the coincidence and antagonism of cancer and aging at the multicellular level.

Regarding the origin of aging, one of the claims is that aging is a natural consequence of cell developmental program rather than the accumulation of mutational faults [67]. DRDM results also agree with this claim in that no mutation has been introduced in the model. A critical interdependence structure must exist in the homogeneous rules of intercellular interactions to yield the emergence of quasi-stability of *normal* states and its bifurcation into two ends.

This quasi-stability can be understood in another statistical picture: by scanning the parameter space of *e-d-a* to obtain 3×10^4 samples of simulation results (one sample for one set of parameters) over $t = 10^6$ time steps, one can plot a histogram of the phenotype structure as shown in Fig.2.9. The horizontal axis is the normalized phenotype structure v, formulated as

$$v = 0.1N_a / N_{max} + N_t / N_{max} \qquad \text{(Eq.2.3)}$$

(also refer to Eq. 2.1) where N_a, N_t, and N_{max} are the number of arrested cells, tumorigenic cells, and the total lattice nodes. As demonstrated in Ch.2.1.3, v not only represents the structures of the phenotypic subpopulations but also implies the global fitness of the system, with $v = 0$ corresponding to the extinction (all cells dead) and $v = 1$ to a complete tumorigenic state (all cells proliferative). Therefore, one may also regard v as vitality index of the system.

In Fig.2.9(left), the histogram has the three high bulks roughly at degenerate ($v < 0.08$), normal (v spanning from 0.3 to 0.7), and tumorigenic ($v = 1$) states, By transforming the frequency $f(v)$ into a normalized probability $P(v)$ as:

$$P(v) = f(v) \Big/ \int_0^1 f(v)\mathrm{d}v,$$

one can obtain a "pseudo energy landscape" with − log P (v) as an effective free energy and v as the conformation coordinate [right panel in Fig.2.9]. From a perspective of statistical physics, the conformations featuring the lower energy can exist with the larger incidence in nature because equilibrium dynamics tend to push the system into the state with minimal free energy. Two big energy minima can be detected at degenerate and tumorigenic ranges of v, implying that degeneration and tumorigenesis are two equilibrium states, i.e., two most stable forms, of homeostasis in the DRDM. Nevertheless, a shallow and rugged valley of normal states spans an extensive region of medium v with a higher level of effective energy, indicating that the *normal* state is a metastable state which has intrinsic potential to evolve towards degeneration or tumorigenesis as a relaxation process, and the ruggedness of the normal valley implies that the system dynamics could also be arrested in many sub-metastable states which slow down the relaxation. In this sense, the longtime evolution of quasi-stable *normal* states in the DRDM is analogous to the slow relaxation of the glasses [68]. In order to clarify this glass-forming mechanism in multicellular homeostasis, a further reduction on the degrees of freedom and an abstraction of the essential interdependence structure for resolving self-averaging complexity are needed to link to some analyzable theories in nonequilibrium statistical physics (see Ch. 4).

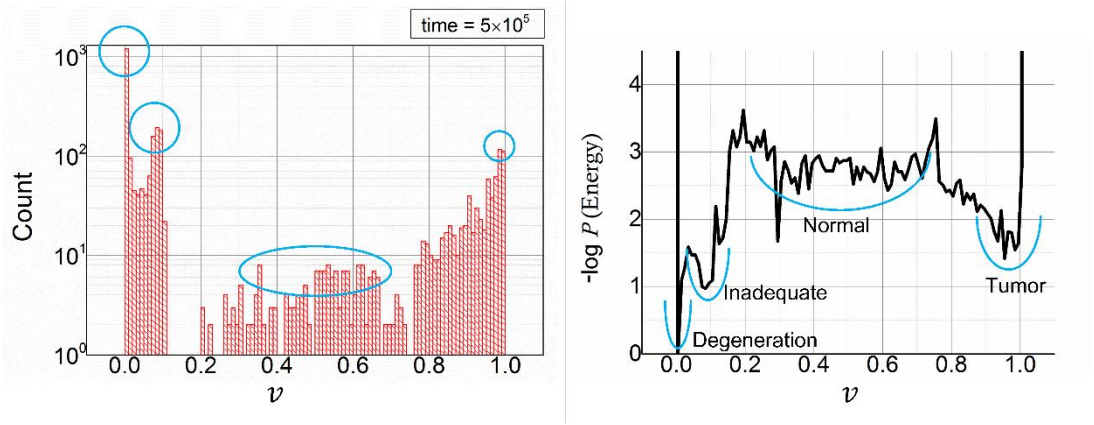

Figure 2.9 Histogram (left) and corresponding probability distributions (right) of normalized phenotype structure v measured at $t = 10^6$ steps in 3×10^4 sessions of simulation.

2.3 Homeostasis with mutations

(The contents including figures and tables in Ch.2.3 are adapted from Ref.[69])

The homeostatic dynamics in the abovementioned DRDM is self-organized through local interactions among individual entities without considering adaptation and the non-mutational receptor dynamics seem to embrace the core interdependence structure responsible for the emergence of diverse homeostatic states and for the slow bifurcation of normal homeostasis into tumorigenic and degenerative states. Nonetheless, abundant experimental and theoretical works on cancer genomics show that genetic instability and intratumor heterogeneity are indispensable in cancer progression and in its resistance to therapies [70-72]. In this part, some mutation models will be introduced to the DRDM to scrutinize the system dynamics under the coupling effect of self-averaging complexity (related to the essential non-mutational interdependence structure) and the complexity brought by mutation and adaptation.

2.3.1 Mutation models: somatic mutations

As the entities like DNAs, genes, chromosomes, proteins are not explicitly modeled, a mutation event in DRDM is defined as a small amount of variation in one cellular parameter (such as the thresholds in Table B1) related to the genetic information. Thereby in this model, the concept of mutation is not narrowly referred to the alterations of genes; instead, this mutation can be a combined effect of genetic and epigenetic changes along with disordered regulation of the endogenous network [73] manifested at the cellular level.

The mutations in real systems are somatic, meaning that the subcellular abnormalities are accumulating slowly and steadily through time [74] and the

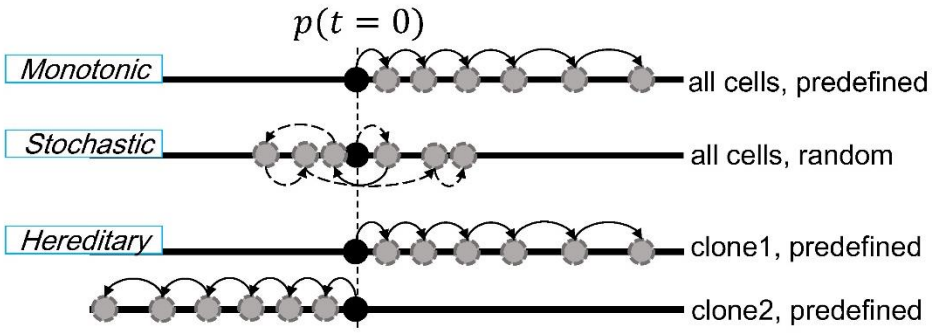

Figure 2.10 Three ideal prototypes of mutation models in the space of the mutant *p*. The arrows point to the direction of time.

inheritance of genetic information contributes to the clonal expansion in cancer [75]. Additionally, most mutations at genetic or epigenetic levels are unnoticeable and harmless on the phenotypic level, whereas very few others yield a non-trivial phenotypic consequence because of the variation of genetic contents hitting critical levels. Combining these facts, three prototype mutation sub-models are conceived as illustrated in Fig.2.10: *monotonic*, *stochastic*, and *hereditary*, with p representing the mutable cellular parameter. The two basic principles underlying these models are that p is replicable through cell division and the variation of it are iterative through time. Due to the absence of genetic details in DRDM and to the lack of the knowledge about how cellular traits should vary with time, one can only articulate the rules of the mutation of p based on simple assumptions. Two extremal cases are first considered: 1) the mutations are algebraically accumulating in one direction (the *monotonic* model) or 2) they are totally isotropic and unpredictable (the *stochastic* model). Then a third case sitting in between is conceived (the *hereditary* model). The mathematical representations of the mutation can be formulated as:

$$p_i(t+1) = p_i(t)F(\mu), \qquad \text{(Eq.2.4)}$$

for any chosen mutable cellular parameter p of a cell at site i when it proliferates time $t + 1$. $F(\mu)$ is the mutation function depending on a mutation rate μ. Next, let me introduce the respective formulations of $F(\mu)$ for three mutation models. Note that μ is a critical parameter associated with the timescale difference between the non-mutational relaxation and the mutational adaptation processes: a low μ makes the effect of mutation trivial, whereas a high μ accelerates the adaptation of the system.

1) *Monotonic* model

The *monotonic* mutation model belongs to the first extreme, i.e., a simple algebraic accumulation of mutations at a predefined mutation rate with no heterogeneity. It idealizes a scenario where the mutation towards one direction at each step is triggered by those at previous steps, thus forming a positive feedback which amplifies itself through time. This amplification of mutation effect is usually seen in cancer where a small alteration in the tumor suppressor genes like p53[76] causes a series of malfunctions in the cell cycle inhibition, self-repairing, apoptosis and even the activations of other oncogenes in progression, as a result of which the level of growth factors may incessantly increase.

Accordingly, the function $F(\mu_m)$ in Eq.2.4 for the *monotonic* model is formulated as $1+\mu_m$ or $1-\mu_m$, rendering an algebraic increase or decrease in p_i; the subscript m in μ_m stands for "*monotonic*". Note that for each mutable p, there are two mutation directions which are also inherited from the ancestor.

2) *Stochastic* model

The *stochastic* model belongs to the second extreme, i.e., the directions of mutation are isotropic, showing the maximal heterogeneity. This kind of mutational isotropy is conventionally believed to occur at the genetic level [77]. Unlike the *monotonic* mutation, the *stochastic* model does not assume any regular feedback dynamics that define the relationship between the subcellular variations and the changes in cellular traits and the mutation at the cellular level is also random because of the uncertainty and complexity brought by the infinite degrees of freedom.

Hence, the mutation function $F(\mu_s)$ for the *stochastic* model is formulated as $\exp(\mu_s X)$, where $X \sim N(0, 1)$ is a random variable with a standard Gaussian distribution and the subscript of s in μ_s stands for "stochastic". As shown in Fig.2.10, p_i randomly drifts in the mutant space with unpredictable trajectories, so *stochastic* mutations feature the maximal heterogeneity among the cells in theory.

3) *Hereditary* model

As one may notice, the real mutations at the cellular level can hardly be fully homogeneous or with perfect heterogeneity. Cells from the same clone mutate in a more similar way and various clones may coexist or compete. This is the "clonal expansion" in many multicellular systems [75]. The *hereditary* model is thence proposed for realizing a limited heterogeneity like that of clonal expansion. As is shown in Fig.2.10, *hereditary* mutation is a mixture of different monotonic mutations and cells with the same clonotype (copied from their mothers) share the exclusive *monotonic* mutation strategy symbolizing their clonal lineage. Positive feedback loops towards multiple directions characterized by the different cell clones can thereby coexist in the system and the competition among them yields clonal expansion; nevertheless, since the cells within each clone still share one *monotonic* mutation strategy along each dimension of the mutant space p, the heterogeneity of the mutations disappear in each clone.

The formulation of $F(\mu_h)$ is the same as those in the *monotonic* model but the different clonotypes have distinct predefined mutation rates and the mutation directions. The subscript "h" refers to "*hereditary*".

In the last part of Ch.2.3.2, I will also introduce a more complex mutation model that integrates the *hereditary* with *stochastic* mutations to be more representative of the mutations in the real clonal evolution.

4) Sub-models of mutation in DRDM

In this study, I chose the ECM saturation rates e_{scr} and the death receptor transforming rate d_{scr} as two mutable parameters, which also play critical roles in controlling homeostatic states in DRDM. Note that the ratio of these rates over their respective thresholds serve as the dimensionless control parameters.

Table 2.4. Sub-models of mutations in DRDM for any cell at site i when it proliferates at $t+1$.

Sub-model	Rules	Characteristics
monotonic	$e^i_{scr}(t+1) = e^i_{scr}(t)(1-\mu_m)$ or $e^i_{scr}(t+1) = e^i_{scr}(t)(1+\mu_m)$ or $d^i_{scr}(t+1) = d^i_{scr}(t)(1-\mu_m)$ or $d^i_{scr}(t+1) = d^i_{scr}(t)(1+\mu_m)$	homogeneous deterministic
stochastic	$e^i_{scr}(t+1) = e^i_{scr}(t)\exp(\mu_s X)$ and $d^i_{scr}(t+1) = d^i_{scr}(t)\exp(\mu_s X)$, $X \sim \mathcal{N}(0,1)$	heterogeneous stochastic
hereditary	c =1: $d^i_{scr}(t+1) = d^i_{scr}(t)(1+\mu_{h,d})$ and if $d^i_{scr}(t+1) > d^i_{scr}(0)(1+s)$, $e^i_{scr}(t+1) = e^i_{scr}(t)(1-\mu_{h,e})$	
	c =2: $d^i_{scr}(t+1) = d^i_{scr}(t)(1-\mu_{h,d})$ and if $d^i_{scr}(t+1) < d^i_{scr}(0)(1+s)^{-1}$, $e^i_{scr}(t+1) = e^i_{scr}(t)(1+\mu_{h,e})$	
	c =3: $d^i_{scr}(t+1) = d^i_{scr}(t)(1+\mu_{h,d})$ and if $d^i_{scr}(t+1) > d^i_{scr}(0)(1+s)$, $e^i_{scr}(t+1) = e^i_{scr}(t)(1+\mu_{h,e})$	limited heterogeneous
	c =4: $d^i_{scr}(t+1) = d^i_{scr}(t)(1-\mu_{h,d})$ and if $d^i_{scr}(t+1) < d^i_{scr}(0)(1+s)^{-1}$, $e^i_{scr}(t+1) = e^i_{scr}(t)(1-\mu_{h,e})$	clonal expansion
	c =5: $e^i_{scr}(t+1) = e^i_{scr}(t)(1+\mu_{h,e})$ and if $e^i_{scr}(t+1) > e^i_{scr}(0)(1+s)$, $d^i_{scr}(t+1) = d^i_{scr}(t)(1-\mu_{h,d})$	sequential mutation
	c =6: $e^i_{scr}(t+1) = e^i_{scr}(t)(1-\mu_{h,e})$ and if $e^i_{scr}(t+1) < e^i_{scr}(0)(1+s)^{-1}$, $d^i_{scr}(t+1) = d^i_{scr}(t)(1+\mu_{h,d})$	deterministic
	c =7: $e^i_{scr}(t+1) = e^i_{scr}(t)(1+\mu_{h,e})$ and if $e^i_{scr}(t+1) > e^i_{scr}(0)(1+s)$, $d^i_{scr}(t+1) = d^i_{scr}(t)(1+\mu_{h,d})$	
	c =8: $e^i_{scr}(t+1) = e^i_{scr}(t)(1-\mu_{h,e})$ and if $e^i_{scr}(t+1) < e^i_{scr}(0)(1+s)^{-1}$, $d^i_{scr}(t+1) = d^i_{scr}(t)(1-\mu_{h,d})$	

Note: c is the clonotype identity, s is the coefficient controlling the significance of the sequence in mutation and $\mu_{h,d}$, $\mu_{h,e}$ are the mutation rates for d_{scr} and e_{scr} respectively in the *hereditary* model.

Hence, changing d_{scr} and e_{scr} with fixed the threshold d and e is equivalent to varying the thresholds with fixed values of the rates. This equivalence also implies that the

current DRDM still embraces some reducible degrees of freedom.

The ECM saturation fraction e_{scr}, which is the upper limit of the ECM amount secreted by per mass of its growth receptors, decides the sensitivity of a cell to its ECM. When e_{scr} is small, ECM concentration reaches saturation level very rapidly so that the growth receptors are quickly transformed into ECM receptors, yielding a higher tendency for polarization and the subsequent cell cycle arrest. The death receptor transforming rate d_{scr}, as the term expresses, decides the susceptibility of a cell to death. In a simpler interpretation, the decrease in e_{scr} contributes to the cell cycle arrest and the increase in d_{scr} to the cell death. The specific mutation rules for e_{scr} and d_{scr} are summarized in Table 2.4. Since two mutable parameters are involved in the *hereditary* model, the sequences of two mutations have been considered as well. For clonotype c = 1, for instance, the cell first mutates d_{scr} and then triggers the mutation of e_{scr} if the value of d_{scr} has changed by a fraction s ($s \geq 0$) of the original value, where s is a sequence coefficient. If s = 0, the mutations of the two parameters are simultaneous; otherwise, two mutations occur in a sequence. If s is sufficiently large, the mutation of a second parameter will be postponed over so long a time that the 8-clone-hereditary model is reduced to a straightforward mixture of four monotonic mutations listed in Table 2.4 (row 2, column 2). It should be mentioned that the choices of the *hereditary* clones indeed can be **any** linear combinations of the *monotonic* mutations; nevertheless, the eight clones adopted here are the most representative ones spanning the whole mutant space of d_{scr}-e_{scr}.

2.3.2 Time-dependent results

The simulation results are divided into two parts. The first examination is on the effect of different mutation models under specific normal-to-degeneration transitions which correspond to the life process of a healthy tissue (most cells stay in cell cycle arrest and the total cell number is large; refer to Ch.2.2.). Parameter settings are listed in Table B2 in Appendix B(2). The effect of mutations could be identified through comparing the time-dependent evolutions of the normalized phenotype structure v (Eq.2.3) under different mutation rates. Note that v = 1 corresponds to tumorigenic states and v = 0 corresponds to extinctive degeneration.

1) *Monotonic* mutations:

As shown in Fig.2.11, mutations of e_{scr} and d_{scr} disturb the original relaxation process (all black curves with v roughly above 0.1 lasting about 10^5 steps before a catastrophic crashing) in various ways. If e_{scr} is mutated as $e^i_{scr}(t+1) = e^i_{scr}(t)(1+\mu_m)$ [denoted as $e_{scr}\uparrow$ in Fig.2.11(A)], the sensitivity to ECM decreases and thus postpones cell cycle arrest; by contrast, the mutation $e^i_{scr}(t+1) = e^i_{scr}(t)(1-\mu_m)$ [denoted as $e_{scr}\downarrow$ in Fig. 2.11(B)] causes a higher propensity for cell cycle arrest. As one can observe, the

increase in e_{scr} veered the degenerative processes towards tumorigenesis with larger mutation rates μ_m [Fig.2.11(A)], whereas if e_{scr} mutates to a smaller value, the catastrophic crash occurs earlier to extinction, indicating a severer degeneration with this mutation [Fig.2.11(B)].

The results of d_{scr} mutation are more difficult to interpret. The mutations yielding higher values of d_{scr} (denoted as $d_{scr}\uparrow$), i.e., a higher synthesis rate of death receptors, veer the degenerate process first towards tumorigenesis then towards an extinctive catastrophe [Fig.2.11(C)]. Contrastingly, the mutations yielding lower values of d_{scr} (denoted as $d_{scr}\downarrow$) extend the "lifespan" of the homeostatic quasi-stable degenerative states before the catastrophic crash; although the temporal fluctuations of v are intensified with increasing μ_m, the trend of degeneration has not been changed [Fig.2.11(D)]. Additionally, there exists a critical value of μ_m exceeding which the degenerative process transitions to the tumorigenic process in $e_{scr}\uparrow$ and $d_{scr}\uparrow$ mutations [the red curves in Fig.2.11 (A) and (C)].

To summarize, if μ_m is large enough to affect the homeostatic relaxation process, the decrease in tendency of cell cycle arrest promotes the emergence of tumorigenesis; counterintuitively, the increase in cell death rate induces tumorigenesis followed by an extinction, and the decrease in death rate merely extending the period of quasi-stable plateaus without inducing a phase transition.

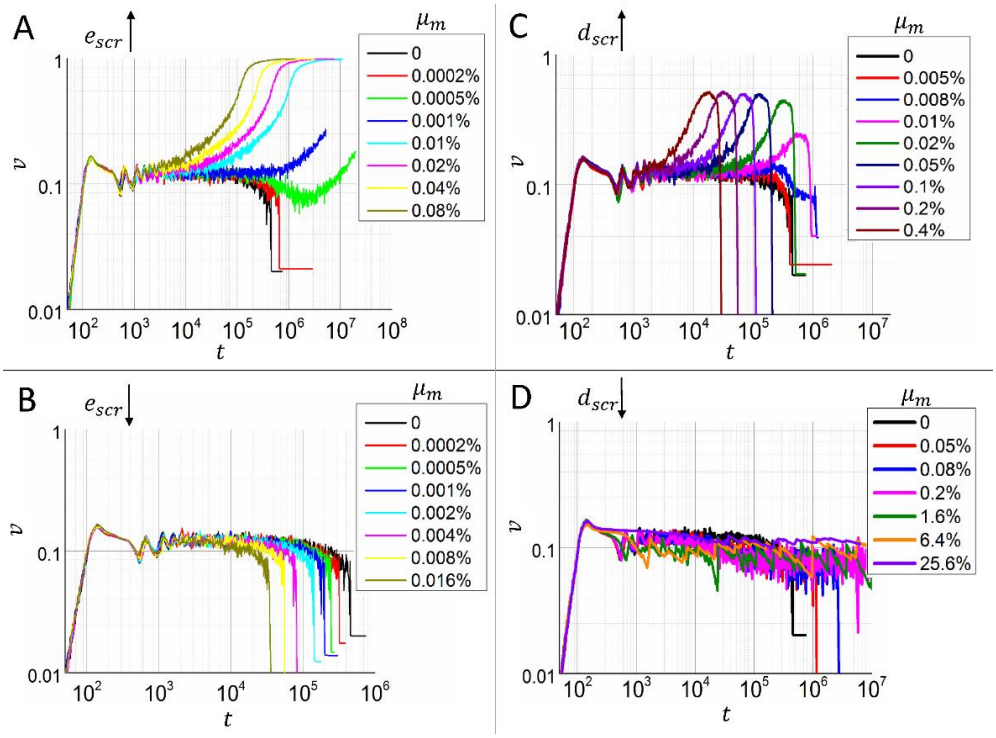

Figure 2.11 Time evolution of phenotype structure index v under four distinctive monotonic mutations with different mutation rates. Zero values of μ_m correspond to a typical non-mutational homeostatic process (black) Note that all figures are plotted in log-log scale.

2) *Stochastic* and *hereditary* mutations

The effect of *stochastic* mutations is rather simple: there exists a critical value of μ_s, surpassing which leads to a phase transition from degeneration to tumorigenesis; an earlier advent of tumorigenesis corresponds to larger values of μ_s as illustrated in Fig.2.12 (left). It seems that neutrally heterogeneous mutations are tumor-inducing by nature.

By contrast, the reality-mimetic *hereditary* mutations bring about a peculiar picture of the system evolutions [Fig.2.12 (right)]. One can observe three basic phases of the evolutionary patterns of $v(t)$ by varying the mutation rate μ_h. For very small mutation rates $\mu_h (= \mu_{h,e} = \mu_{h,d})$ (identified as *phase I*), mutations have very small effects on the original process. For a medium range of μ_h (*phase II*), $v(t)$ veers towards tumorigenesis during the quasi-stable plateaus before crashing into extinction and this evolutionary pattern has also been seen under the *monotonic* mutation $d_{scr}\uparrow$ [refer to Fig.2.11(C)]. For even larger mutation rates μ_h (*phase III*), the system totally deviates from the original degenerative trend to an acute tumorigenesis, which is later followed by a spontaneous regression [$v(t)$ slowly decreasing to over 0.3].

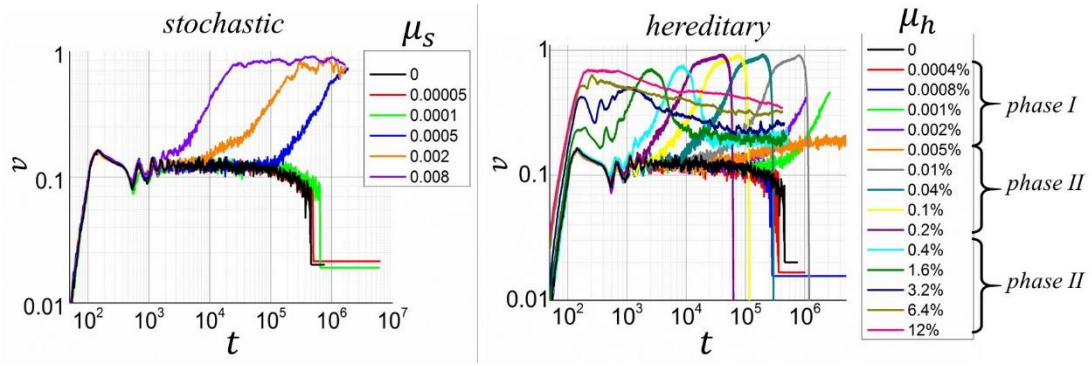

Figure 2.12. The *stochastic* mutation model under varying μ_s (left) and the *hereditary* mutation model under different mutation rate $\mu_h (= \mu_{h,d} = \mu_{h,e})$ with the sequence coefficient s =0.05 (right).

3) Subpopulation dynamics with *hereditary* mutations

To unravel the complexity involved in *hereditary* mutations, one must scrutinize the subpopulation dynamics, i.e., the dynamics of "clonal expansion" in relation to different mutation rates.

Fig.2.13 (A) exhibits the snapshots of the clonal expansion with the eight colors labeling different clonal lineages, whose mutation rules can be found in Table 2.4. Eight ancestors with distinct clones are initially scattered into the 2D space and then develop into eight patches occupying territories in similar sizes with recognizable boundaries at early stages [the top two panels in Fig.2.13 (A)]. After thousands of steps, the

boundaries between patches become vague because of the invasion of advantageous clonal lineages into the territory of the disadvantageous ones. Through a longtime competition among these clones, only one clone can survive as the "fittest" and eventually take over the whole space. This clonotype is hereafter termed as *winner* for simplicity of demonstration.

The incidence of each clonotype to become a *winner* in 200 sessions of simulation for several mutation rate μ_h are exhibited in Fig.2.13(B). *Winner* is algorithmically identified as the clonotype *c* satisfying that

$$N_c(t) > 0.8\sum_c N_c(t)$$

for all time $t > t_0$, where N_c is the number of cells in clonotype *c* and t_0 is a finite time point characterizing the timescale of clonal competition. Under different mutation rates μ_h, the distribution of *winner* is different:

(i) In the non-mutational case ($\mu_h = 0$), all clonotypes can win with nearly 12.5% as is expected.

(ii) For μ_h slightly over zero [< 0.01%, corresponding to the *phase I* in Fig.2.12 (right)], c = 7 and 5 can win with higher probability than others while the evolution of *v* seems erratic because of the unpredictable winner [see the curves of 0.0008%, 0.001%, 0.002% and 0.005% in Fig.2.12 (right)]; however, degeneration still reigns, manifesting the strong impact of the original non-mutational degenerative homeostasis.

(iii) For μ_h in a medium range roughly from 0.01% to 0.3% [corresponding to *phase II* in Fig.2.12 (right)], c = 7 and 3 are most probable to become *winner* while the system undergoes the extinction-inducing tumorigenesis [see the curves of 0.01%, 0.04%, 0.1%, and 0.2% in Fig.2.12 (right)].

(iv) For μ_h even larger [> 0.3%, corresponding to *phase III* in Fig.2.12 (right)], c = 5 and 2 replace c = 7 and 3 to become *winner* and the evolution of *v* undergoes an acute tumorigenesis succeeded by spontaneous regression [see the curves of 0.4%, 1.6%, 3.2%, 6.4% and 12% in Fig.2.12 (right)].

Fig.2.13(C) shows the normalized phenotype structure *v* measure at the time t_0 (the time when *winners* appear) averaged over the 200 sessions for varying μ_h. One can observe a continuous transition from *phase I* to *phase II* and from *phase II* to *phase III*, within which *phase II* has the highest averaged $v(t_0)$, i.e., most tumorigenic.

Fig.2.13 (D) shows the subpopulations dynamics of eight clonal lineages in three phases respectively. One may easily find that in *phase III* (μ_h=1%), c = 7 and 3 can thrive before the domination of c = 5 and 2, implying that the emergence and the regression of tumor in *phase III* could be explained by this alteration of the dominant clonotypes.

For the effect of the mutation sequence, one can compare the winning rates between $c = 7$ and $c = 3$ or between $c = 5$ and $c = 2$. Mutation rules of $c = 7$ (or $c = 5$) differs from $c = 3$ (or $c = 2$) merely by the mutation of e_{scr} prior to the mutation of d_{scr} (refer to Table 2.4). As shown in Fig.2.13 (B), the fact that $c = 7$ (or $c = 5$) has higher *winner* incidence than $c = 3$ (or $c = 2$) does suggests that e_{scr} mutations are more effective than d_{scr} mutations.

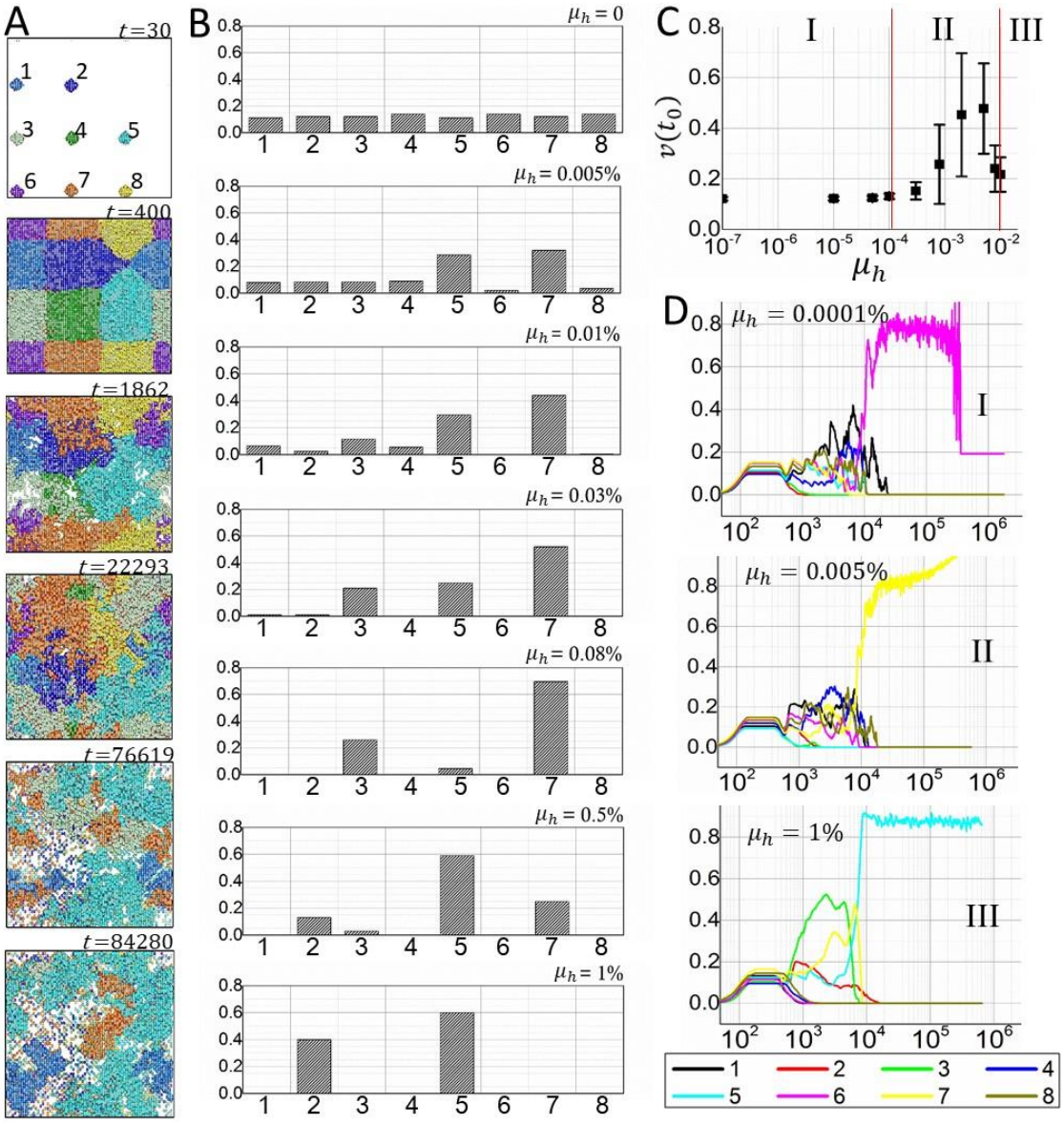

Figure 2.13 Subpopulation dynamics in the *hereditary* model. (A) A sample result of the interspecies competition among eight clonal patches (μ = 0.5%). (B) The frequency of becoming *winner* for eight *hereditary* clones in 200 sessions of simulation for each mutation rate μ_h. (C) Averaged v measured at time t_0 under varying μ_h. (D) Time evolutions of the subpopulations in three phases.

2.3.3 Bridging hereditary and stochastic models

It should be noted that the foregoing *hereditary* model uses equal mutations rates for e_{scr} and d_{scr}. This constraint of equality brings about undesirable rigidity to the mutations. Hence, loosening this constraint should give some plasticity to the *hereditary* mutation rules and may bridge the gap between the *hereditary* and the *stochastic* model.

Two modified *hereditary* mutation rules are then proposed:

(i) *Stochastic hereditary* model:

The *hereditary* rules in Table 2.4 can be multiplied by some stochasticity. For instance, for $c = 1$, the rules becomes $d^i_{scr}(t+1) = d^i_{scr}(t)(1+\mu_{h,d})\exp(\mu_{sh}X)$ and if $d^i_{scr}(t+1) > d^i_{scr}(0)(1+s)$, $e^i_{scr}(t+1) = e^i_{scr}(t)(1-\mu_{h,e})\exp(\mu_{sh}X)$, where $X \sim \mathcal{N}(0,1)$ is a random variable from Gaussian distribution and μ_{sh} scales the strength of stochasticity. Fig.2.14 (A1) shows the results of the *stochastic hereditary* model in *phase II* ($c = 3$ or 7 wins; left) and *phase III* ($c = 2$ or 5 wins; right) with varying μ_{sh}. As is conjectured, the newly added plasticity of mutation rules veers the degenerative homeostasis to sustainable tumorigenesis, i.e., the one followed by no extinction and no regression, like those in the *stochastic* models [Fig.2.12(left)].

(ii) *Biased hereditary* model:

A bias between the two mutation rates $\mu_{h,e}$ and $\mu_{h,d}$ such that $\mu_{h,e}/\mu_{h,d} > 1$ can be built in. Fig.2.14(A2) shows the results of *biased hereditary* mutations for *phase II* (left) and *phase III* (right). In *phase II*, a larger ratio of $\mu_{h,e}/\mu_{h,d}$ can prevent the occurrence of extinctive crash (the blue and orange lines); likewise in *phase III*, a larger ratio of $\mu_{h,e}/\mu_{h,d}$. can cancel the spontaneous tumor regression. It confirms that $\mu_{h,e}$ larger than $\mu_{h,d}$ also promotes the sustainable tumorigenesis.

To understand why the *stochastic hereditary* and the *biased hereditary* models have similar behaviors, one can inspect the mutational paths of d_{scr} and e_{scr} under these models. Fig.2.14 (B) shows the time evolutions of the ensemble average of d_{scr} and e_{scr} in their logarithmic scales (denoted as $\langle \log d_{scr} \rangle$ and $\langle \log e_{scr} \rangle$) in the *hereditary model* (the straight lines) and in the *stochastic hereditary* model (the dotted lines). One can observe that the stochasticity given to the hereditary rules yields larger variations in e_{scr} than in d_{scr} , implying that the effective mutation rates under the *stochastic hereditary* mutations are indeed satisfying $\mu^{eff}_{h,e} > \mu^{eff}_{h,d}$, which is the same as defined in the *biased hereditary* model.

Fig.2.14(C) exhibits the comparison of subpopulation dynamics of eight clonal lineages between the *stochastic hereditary* model (C1) and the *biased hereditary* model (C2). Both models show an alteration of dominant clonotypes (from $c = 3$ and 7 to $c = 2$ and 5) underlying the emergence of sustainable tumorigenesis. Combining all the information, it seems that a larger $\mu_{h,e}$ than $\mu_{h,d}$ protects the clonotypes $c = 2$ and 5 from extinction against the temporary domination of $c = 3$ and 7.

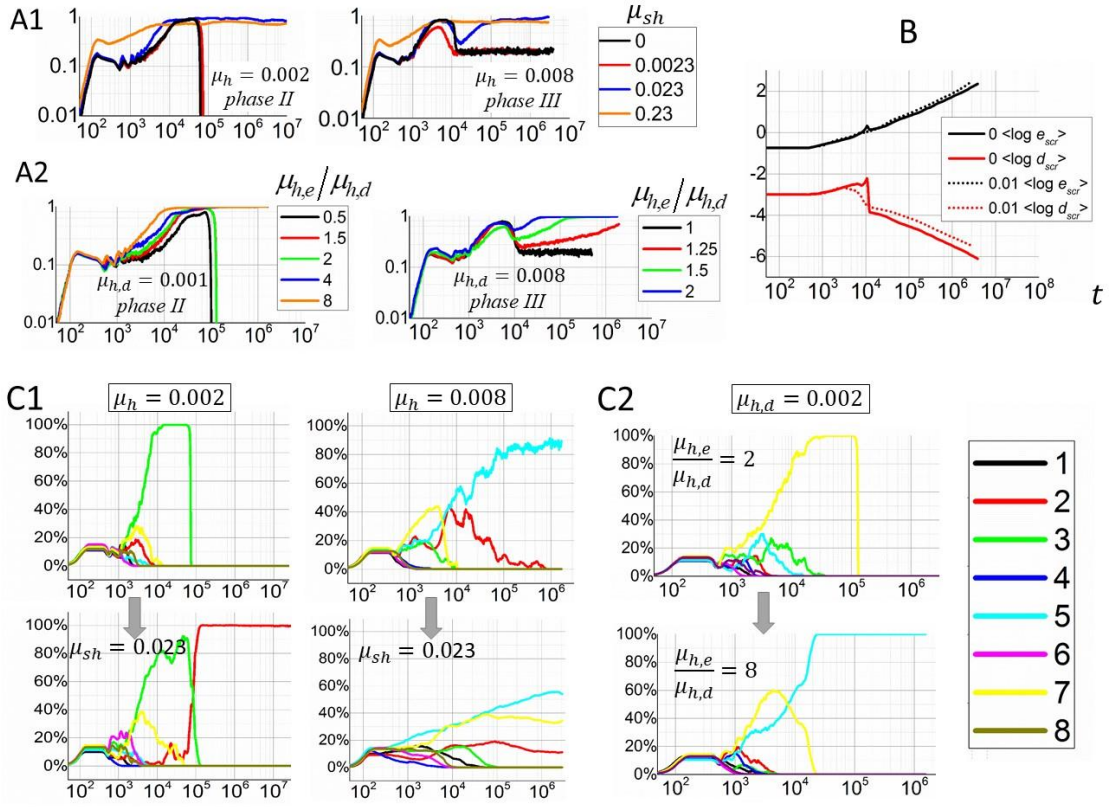

Figure 2.14. Complex *hereditary* models. (A) A comparison of $v(t)$ among the *stochastic hereditary* and the *biased hereditary* model. (B) A comparison of averaged log d_{scr} (t) (red) and averaged log e_{scr} (t) (black) between the *hereditary* model (straight lines) and the *stochastic hereditary* model (dotted lines). (C) Subpopulation dynamics of eight clonal lineages in the *stochastic hereditary* model (C1) and the *biased hereditary* model (C2).

2.3.4 Evolutionary paths on the phase diagram

Despite that the system behaviors under various mutation models seem to be very complicated regarding the mutation strategies and mutation rates, one may seek a unified explanation for them. As proposed in [69], the system's evolutionary trajectories on the phase diagram reveal a strikingly simple principle underlying those complexities: the phase diagram serves as a fitness landscape that selects the mutational paths of individual cells.

Fig.2.15 (A) shows a non-mutational phase diagram exhibiting several phases distinguished by the value of v measured at 10^6 steps in the parameter space of $10^{-3} < e_{scr} < 10^3$ and $10^{-7} < d_{scr} < 10^2$. A simulation time of 10^6 steps is considered as sufficiently long for the most quasi-stable relaxations to be near their equilibria. Similarly as is in Fig.2.6, several phases can be identified by their normalized

phenotype structure v: extinction abbreviated as *E.* (grey), degeneration abbreviated as *D.* (red), inadequate-growth abbreviated as *I.* (orange), and tumorigenesis abbreviated as *T.* (blue). *Normal* homeostasis (yellow and green) narrowly sits between the boundary of *T.* and *D.* (or *I.*).

Fitness landscape, first proposed by Wright [78], is used to visualize the relationship between the genotype and its survival rate (i.e., fitness) in evolutionary biology. Here, the non-mutational phase diagram of DRDM can be viewed as a special fitness landscape for individual cells to "climb": the two control parameters are then mapped to the two genotypes and the normalized phenotype structure v is indeed the survival rate under non-mutational homeostasis.

Usually, if no intercellular interaction is considered, a larger e_{scr} or a smaller d_{scr} promotes the individual fitness of one cell straightforwardly. A larger e_{scr} induces a higher propensity for proliferating and a smaller d_{scr} a lower death rate. The fittest states in terms of individual fitness should appear at the largest e_{scr} and with the smallest d_{scr}. Nevertheless, this fitness landscape resulted from non-interactive cell behaviors can be substantially distorted by the non-mutational homeostatic processes with the real fittest states moved to some phases that do not have maximal individual fitness (e.g., the phase of tumorigenesis *T.*).

Fig.2.15 (A) also shows the mutational paths for four *monotonic* mutations (white arrows) and for eight *hereditary* mutations (black arrows). The initial point (marked as a star) is located at $d_{scr} = 0.001$ and $e_{scr} = 0.18$ and this pair of initial values is shared by all cells at $t = 0$. Note that the initial point sits on the boundary of phase *D.* and *I.*, meaning that the non-mutational homeostasis of the system is normal-to-degenerate. Under *monotonic* mutations, the star symbolizing the system state should move upward, downward, leftward, and rightward. As one may see, the rightward mutation corresponds to an increase in e_{scr} and results in a dynamic phase transition from *D.* to *T.* as seen in Fig.2.11 (A); the leftward mutation corresponds to the decrease in e_{scr} and drives the system into the phase of *D.* and terminates the system dynamics earlier as seen in Fig.2.11 (B). The upward mutation corresponds to an increase in d_{scr} and propels the system first across the zone of near *T.* then reaching the zone of *E.*, explicating the reason why there is a temporary rise of v towards tumorigenesis succeeded by a crash into extinction in Fig.2.11(C). The downward shift corresponds to the decrease in d_{scr} and locks the systems deeply into *I.* without a chance of phase transition as the extended lifespans of the quasi-stable plateaus shown in Fig. 2.11 (D).

In a similar way, one can understand the complicated system behaviors of the *hereditary* model by this phase diagram. The eight *hereditary* mutational paths shift along the two diagonal lines $\log d_{scr} \sim \pm \mu_{h,d}/\mu_{h,e} \log e_{scr}$. If $\mu_{h,d} = \mu_{h,e}$, the mutations are along $\log d_{scr} \sim \pm \log e_{scr}$ (the white dashed lines on the diagram). Clearly, $c = 3$ or 7 will bring the system first towards *T.* quickly before reaching *E.*. By contrast, $c = 2$ or 5 pushes the system along the boundary of *I.* and *T.* hence the system is robustly *normal*.

Other four mutational paths c =1, 4, 6, 8 drive the system leftwards to *D.*, therefore these four clones can hardly survive if the mutation rate is high.

Fig. 2.15(B) shows four typical evolutionary trajectories of d_{scr} and e_{scr} distribution under various mutation models. Each "+" on the schematic phase diagram represents a cell in the space of e_{scr} and d_{scr}. In Fig.2.15 (B1), one can observe that the mutational paths under the *hereditary* model point to two diagonal directions $\log d_{scr} \sim \pm \log e_{scr}$ at an early stage; however, the upper paths are short-lived without foreseeing the phase *E.* behind *T.*. By contrast, the bottom paths mutate along the diagonal lines, which

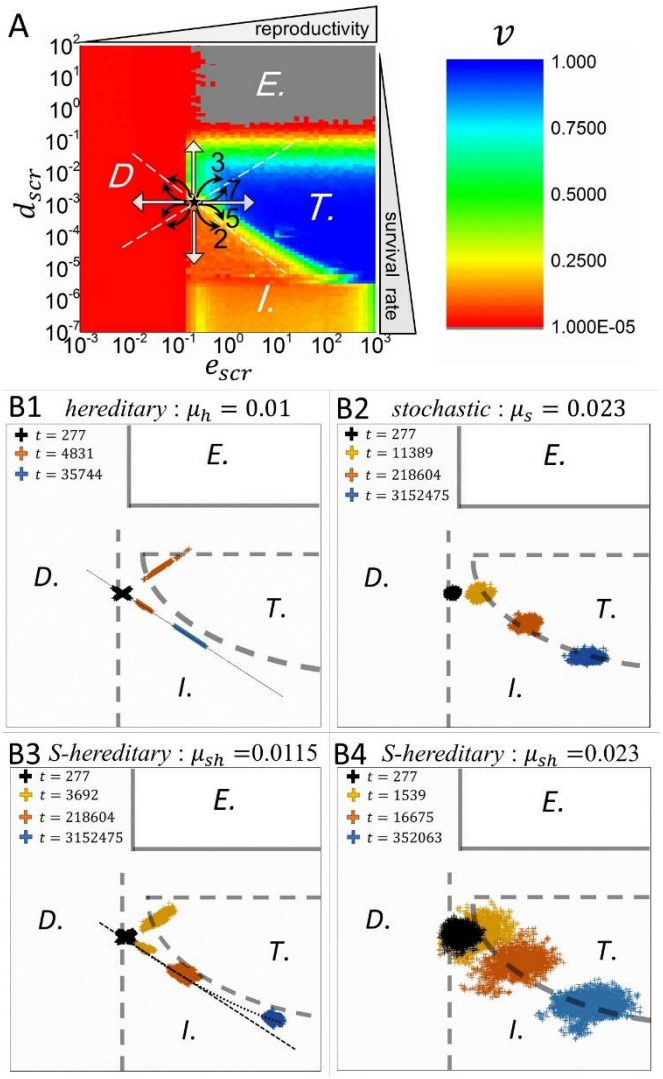

Figure 2.15 System trajectories in the space of d_{scr} and e_{scr} superposed on the phase diagram. (A) The phase diagram in the space of d_{scr} and e_{scr}. Meanwhile, the increase in e_{scr} (or d_{scr}) is related to the increase in the reproductivity (or survival rate) for each individual cell. (B) Sample system trajectories on the phase diagram: (B1) in the *hereditary* model (*phase III*), (B2) in the *stochastic* model, (B3-B4) in the *stochastic hereditary* model with small stochasticity and huge stochasticity.

slightly deviates from phase *T.*. If μ_h is smaller, the upper mutational paths (held by c =3 or 7) could advance more slowly and c =3 or 7 would survive longer as *winner*, yielding the phase *II* dynamics in Fig.2.12(right) and Fig.2.13(C-D); if μ_h is large enough, c = 3 or 7 can only dominate temporarily before all of them are eradicated and the system will undergo a short-time tumorigenesis; then c = 2 or 5 would thrive as *winner* and the system spontaneously regresses from tumorigenesis to normal states, i.e., the *phase III* dynamics in Fig.2.12(right) and Fig.2.13(C-D).

In Fig.2.15 (B2), one can observe that the *stochastic* mutations are isotropic and the system quickly finds the phase *T.*: the cell marks on the diagram first move right-upwards then right-downwards exactly on the boundary between *I.* and *T.* as a perfect example of the self-organization of stable tumorigenesis under both homeostasis and the mutation. Similarly, for *stochastic hereditary* models [denoted as *S-hereditary* in Fig.2.15 (B3-B4)], the stochasticity can drag the original mutation path towards the proximity of *T.* if the intensity of stochasticityμ_{sh} is high enough.

Also, one can understand why the biased hereditary model can also give rise to sustainable tumorigenesis. The initial values of e_{scr} and d_{scr} and the phase structure determine that for the system to be stable in phase *T.* , the e_{scr} mutation must be faster than d_{scr} mutation, i.e., $\mu_{h,e}/\mu_{h,d} > 1$ [Fig.2.14(A2)]. If d_{scr} mutation is extremely slow, then the system needs a sufficiently large $\mu_{h,e}/\mu_{h,d}$ to ensure a fast e_{scr} mutation for reaching *T.* [refer to *phase II* in Fig. 2.14(A2)].

2.3.5 Phase diagram as a fitness landscape for “system selection”

The methodology used in Ch.2.3.4 is not confined to the DRDM mutation. A more general application to other models is within the vision. Let’s consider any control parameter x uniformly encoded as an individual property that controls the non-adaptive phase separation. These phases can be distinguished by an order parameter v that incorporates the fitness information. Fig.2.16 (A) shows a one-dimensional (1D) schematic phase diagram for a generic system, whose states are marked as a ball sitting where the ensemble average of x is. The fitness landscape under non-adaptive relaxation processes, denoted as $f_{sys}(x)$, is just the phase function $v(x)$. It works as a Wright potential of “system selection” for the individuals. Fig.2.16 gives an exemplary landscape of $f_{sys}(x)$, in which the system fitness decreases with a smaller x and has three phases with two boundaries. One essential point is that the order parameter v must be associated with f_{sys}. Next, suppose that $f_{in}(x)$ is the individual fitness landscape under non-interactive processes (e.g., natural selection or sex selection), the total fitness landscape synthesizing the interactive and non-interactive selections can be the superposition of the $f_{sys}(x)$ and $f_{in}(x)$. Fig.2.16 (B1-B3) present three examples of the synthesized fitness landscape under three distinctive $f_{in}(x)$.

In Fig.2.16 (B1), $f_{in}(x)$ has the same trend with $f_{sys}(x)$, hence the synthesized

fitness has the maximum at $x = 0$. By contrast, if $f_{in}(x)$ has the opposite trend to $f_{sys}(x)$ as depicted in Fig.2.16(B2), the evolutionary trajectories of the system may be arrested in some locally fittest state in a way related to mutational paths: under the *stochastic* mutations, the system can explore freely within the proximity of $x(0)$ and always has a chance to overcome the fitness barrier to reach the globally fittest state which exactly sits near the critical boundary between two phases.

As for some more rigid mutations, they may not have enough freedom to overcome the fitness barrier and therefore tend to evolve towards a state with extremely low f_{sys} and only to reach the local maximum of fitness there. Fig.2.16(B3) shows a more complicated situation where $f_{in}(x)$ is nonlinear and having multiple peaks; as a result, the fitness barrier becomes so huge that no paths to the globally fittest state (P3) are inaccessible for all mutation strategies.

One can deduce that for any multi-dimensional control parameter $\boldsymbol{x}$, the synthesized fitness from $f_{sys}(\boldsymbol{x})$ and $f_{in}(\boldsymbol{x})$ may exhibit outrageous complexity, because of which the evolutionary dynamics look erratic especially under rigid mutations. Also, the system's initial condition (where the ball initially locates) can severely affect the whole evolutionary process, adding more complexity to the problem. One can even expect a fluctuating landscape where the function of $f_{in}(\boldsymbol{x}, t)$ is dynamically updated because of the turbulent environment or the heterogeneous coevolution among the individuals. The speed of evolution (gradients of the landscape) depends on both the mutation rate μ of single reproduction events and the transient system fitness (see more discussions in Ch.5.2).

The mutational DRDM simulations is a vivid example of a system with a 2D control parameter $\boldsymbol{x} = \{e_{scr}, d_{scr}\}$ and with the system fitness measured as the phenotype structure. Under the ergodicity assumption, the normalized phenotype structure v can be the probability of each cell to be proliferative. In other words, v is also meaningful to a single cell and it can be superposed to the individual fitness $f_{in}(x)$.

In the range of $e_{scr} > 10^{-1}$ and $10^{-4} < d_{scr} < 10^{-2}$, the phase function of each coordinate, i.e., $v(e_{scr})$ or $v(d_{scr})$, is close to the schematic 1D phase diagram in Fig.2.16 (B2). This clarifies the reason why under the stochastic or the *stochastic hereditary* mutations, the center of the cell cluster in the parameter space always sits exactly on the boundary between *I.* and *T.* because it has the highest fitness. This competition of the system fitness and individual fitness may serve as a mechanism for self-organized criticality [79], which prevails in many other kinds of CASs. A test of this hypothesis to the financial market modeling is present in Appendix C. The mesoscopic approach here enables a direct reproduction of what is conjectured by many biologists: self-organized criticality can be a trade-off between system's robustness and evaluability [80], i.e., critical states of the systems can have highest synthesized fitness under both system selection and natural selection.

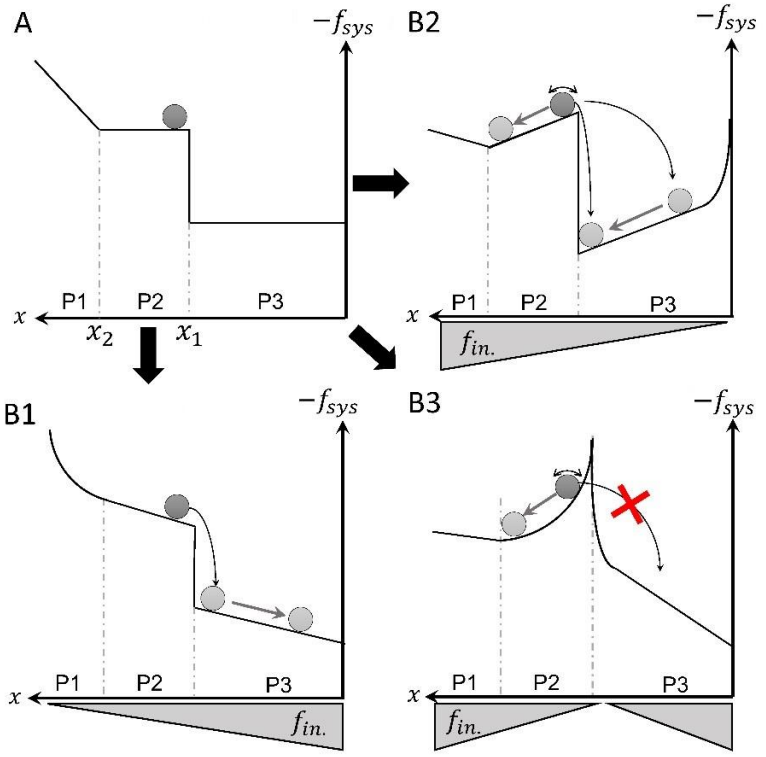

Figure 2.16 Mutational paths visualized as the rolling ball on a 1D schematic fitness landscape. The ball represents the ensemble average of the individual genotype x and the height of the ball corresponds to the equilibrium state of the system. (A) Non-mutational fitness landscape (phase function) $f_{sys}(x)$ of interaction-based relaxation processes. Points x_1 and x_2 are two hypothetical critical points around which a first-order phase transition (at x_1) and a second-order transition (at x_2) happen. (B) The synthesized fitness landscape under three different formulations of individual fitness function of fin(x) with the $f_{sys}(x)$ presented in (A).

2.4 Summary of Chapter 2

The mesoscopic cell-based discrete receptor dynamics model (DRDM) is reformed from a multiscale hybrid model, immersed boundary cell (IBcell) model (Rejniak *et al.*) by coarse-graining the scale of time and space and by reducing the complicated fluid dynamics which cost huge computational resources. Upon the validation of DRDM, I show that DRDM has kept the interdependence structure indispensable for the emergence of diverse homeostasis through the receptor dynamics although the morphological precision is lost. Longtime simulation and large-ensemble analysis are thereby achievable with DRDM and the results gave such a complete

picture of multicellular homeostasis that normal or healthy homeostasis is near the critical range of the system, and therefore it is unstable and eventually slowly transition towards degenerative and tumorigenic states, the former of which is accompanied by aging of cells and the latter by rejuvenation. Cancer and aging seem to have the same origin from the natural evolution of normal homeostasis without extracellular stresses or subcellular mutations.

Through a modeling with mutations, I have shown that the complicated dynamics resulted from the coupling of the self-organization of homeostasis and the individual adaptation has strikingly simple principles. The non-mutational self-organization of homeostasis forms a system fitness landscape where each individual cell can climb with mutations. Tumorigenesis is not the direct consequence of mutation but of the system reaching tumorigenic homeostatic states with the aid of mutations; in some cases, mutations coupled with homeostatic relaxations make the system more robustly sitting at the critical states. These results suggest that the self-organization of homeostasis has a decisive role in system evolution with the phase function serving as the Wright potential of “system selection” on the individual adaptation.

Chapter 3

Multicellular aging

(Note: All contents in Ch.3 including figures and tables are adapted from Ref.[81].)

The most important findings in the DRDM, which is inaccessible from IBcell or other more detailed models are that the non-mutational normal homeostasis is intrinsically quasi-stable near system's critical states and is absorbed into three possible states, extinction, degeneration and tumorigenesis, the evolution to the latter two of which can be rather slow. Normal homeostasis appears as a critical phenomenon of the multicellular system. In light of the statistical nonequilibrium theories for the critical phenomenon in physical systems, a bundle of scaling laws shall appear near the vicinity of the critical point [83]. For instance, the relaxation time should diverge in power-law relation to the control parameters, and this was previously observed in the non-mutational DRDM simulations [see Fig.2.5(B)]. For nonequilibrium systems like glasses, there exists another important scaling law about time variable: if the system near the critical states is perturbed at different time after its preparation(termed as waiting time), the time of its relaxation of this perturbation is in power-law relation to the waiting time:

$$R(t - t_w / t_w^{\theta}) = \bar{R}(t), \qquad \text{(Eq.3.1)}$$

where $R(t, t_w)$ is some relaxation function ($R = 0$ is the end of the relaxation) and $\bar{R}(t)$ is a waiting-time-independent rescaled form, t_w is the waiting time, and θ is the scaling exponent characterizing the aging speed. This scaling is about time, thus called *dynamical scaling* [84] and physical systems showing such dynamical scaling are defined to be aging [82-85]. To avoid ambiguity, the biological aging in the DRDM is referred to as the increase of proliferation age (see the definition in Ch.2.2.2), whereas the aging obeying *dynamical scaling* is termed as physical aging hereafter.

3.1 Wound healing in the DRDM

In DRDM, physical aging can be testable computationally by creating a wound as the perturbation, which has been waited for a specific time after the system reaches quasi-stable states. The multicellular systems react to the wound in a process called wound healing, and wound healing is exactly the biological analog of relaxation against perturbation in the physical systems. Different from physical systems, wound healing is more complex than the mechanistic rearrangement of component positions as in the physical systems. It involves complex biochemical processes that regulate coordinated cell cycle dynamics and cell migration [86].

The investigation of *dynamical scaling* of wound healing in both DRDM and real experiments will help test the hypothesis that normal homeostasis of multicellular systems is a critical phenomenon. The parameters used for wound healing simulation [listed in Table B3 in Appendix B(3)] will reproduce a normal-to-degeneration homeostasis, which is representative of a healthy tissue. Cells were seeded into space simultaneously at the confluence with half density. Then, a small scratch of wound modeled by removing all the cells (clearing the profiles on the lattice nodes) in the wound bed will be implemented after a specific waiting time t_w.

Fig.3.1(A) shows that the healing processes decelerate with waiting times t_w as expected. Fig.3.1 (B) shows the time evolution of normalized unhealed area for waiting times from 24 time steps to 90 time steps; the healing curves with rescaled time axis are present in the inset of Fig.3.1(B), from which one can find that the healing curves fit dynamical scaling with scaling exponent of 0.75 for time larger than 36 steps and smaller than 90 steps. Scrutinizing the dynamics of the subpopulations during the growth before wounding, one can observe a growing population of arrested cells undergoing three regimes [Fig.3.1(C)], the second of which (with a steady linearity) is concomitant with the *dynamical scaling* regime. This suggests that the speed of the colonization of arrested cells is related to the aging rate θ of the system.

Remember that the increase in the arrested cell population is a degenerative process accompanying the increase in averaged proliferation age, i.e., the biological aging (refer to Ch.2.2.3). Hence, the slowdown of wound healing in the DRDM is an instance of both biological aging and physical aging.

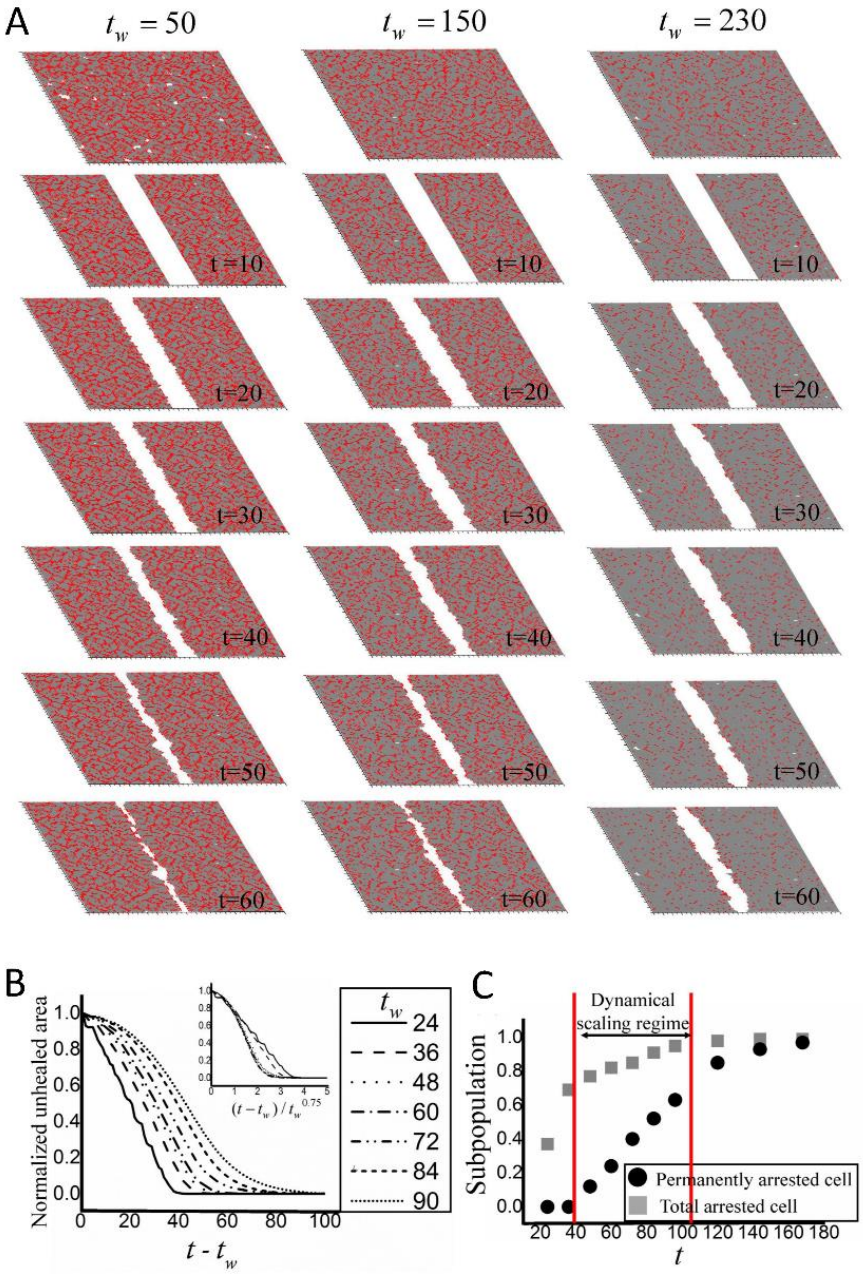

Figure 3.1 Slowdown of healing in DRDM. (A)Snapshots of simulated time-delayed wound healings in the DRDM) with low diffusivity. Grey dots represent arrested cells, while the red ones proliferative cells. ECM threshold $e = 2.5R_M$, arrest threshold $a = 0.2R_M$, growth threshold $g = 0.1\ R_M$, adhesion threshold $h = 0$ (zero motility). Other parameters are listed in Table B3. (B) Healing processes on a normal and a rescaled (inset) time axis. (C) Population dynamics for arrested cell during the waiting before wounding. Permanently arrested cells are defined as the arrested cells with the sum of growth and adhesion receptor amount below growth threshold g.

3.2 Time delayed wound healing assays (TDWHA)

Wound healing assay (WHA) [87] is a simple and inexpensive in vitro experiment used for studying the coordinated cell proliferation and migration in tissue regeneration or tumor invasion. In WHAs, "wound healing" specifically refers to the event that a sheet of cells regenerates a confluent monolayer after some cells have been removed. Just as relaxation is the collective response of particles to an external perturbation in physics, healing is the collective response of cells to an external damage (the wound).

Conventional WHAs require wounds to be performed immediately after cell starvation is finished to avoid any time-dependent changes in cellular conditions, which is, nevertheless, indeed my research focus. Therefore, a controlled waiting time before wound creation is added on purpose to the original WHA protocols, and this modified experimentation is called time-delayed WHA (TDWHA) hereafter. With all the other experimental settings identical, the relationship between the waiting time and the time-dependent healing functions can characterize the endogenous evolution of the system. Particularly, a slowdown of healing with the increasing waiting time is suggestive of the loss of regenerative power in the system, which is considered as a hallmark of tissue aging [138].

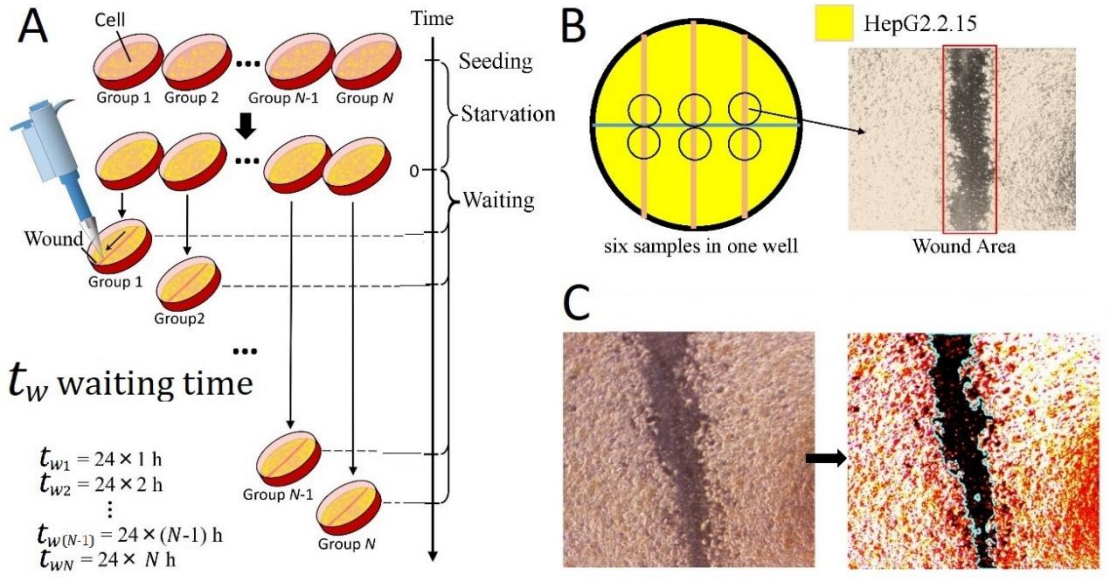

Figure 3.2 Time-delayed wound healing assays. (A) A schematic protocol. Group number N corresponds to a waiting time of $24 \times N$ h. (B) Left: one well has three scratches (wound gaps) represented by the vertical pink lines; six sample areas, marked by six circles, are located in the center adjacent to the horizontal auxiliary blue line. Right: a sample of photograph taken by the microscope (magnification: 400×). (C) Post-processing of images using Photoshop CS6 to calculate the wound area by the number of pixels enclosed by the wound edges (cyan curves).

3.2.1 Experimental settings

Newly thawed HepG2.2.15 cells were seeded near confluence into 6-well dishes at an initial density u_0. The dishes were divided into N groups, in each of which 6-12 samples waited for a specific period of time t_w =24, 48, 72…(hours) before the creation of a 0.25mm scratch wound by a pipette [Fig.3.2(A)]. After that, each group was continuously observed for about 190h and photographed once every 24h. The medium was replaced once or twice a day to keep sufficient nutrients. Two series of experiments were conducted with different initial seeding densities, $u_0=5\times10^5$ cells/mL in Experiment I and $u_0=2\times10^6$ cells/mL in Experiment II. The cell line was chosen as the HepG2.2.15 for its slow cell packing and low propensity to mutations to avoid uncontrollable variations in cell conditions through time. All other experimental settings are controlled as identical [see APPENDIX D(1)].

In each dish, three parallel straight wound gaps were created (the vertical pink lines), with six samples located at the center of the well adjacent to a horizontal auxiliary blue line as shown in the left panel of Fig.3.2(B). The right panel in Fig.3.2 (B) presents an exemplary snapshot from the experiments. The photographs were post-processed in Adobe Photoshop CS6 for counting the pixel number in the wound areas using the Magic Wand Tool [Fig.3.2(C)].

3.2.2 Pre-wounding conditions

1) Cell growth:

Fig.3.3(A) shows the pre-wounding cell conditions in Experiments I and II. During waiting, the total cell number increased to a saturation level with the single-cell viability decreasing to a non-zero level [see APPENDIX D (2-3) for the methods]. Growth saturation in Experiment II occurred earlier than in Experiment I because of the higher

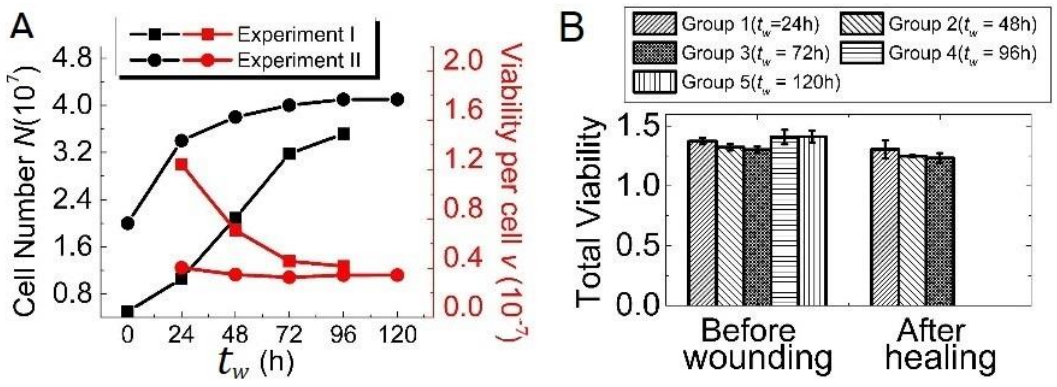

Figure 3.3 Cell number and cell viability. (A) The pre-wounding time evolution of cell number (black), and single cell viability (red) during natural growth. (B) Comparison of the total cell viability immediately before the wounding and after the completion of healing (Groups 1-3 only).

seeding density. Fig.3.3 (B) shows the total cell viability immediately before the wound creation and after the healing completion in Experiment II. Compared with the pre-wounding viability, the post-healing viability in Groups 1-3 decreased slightly about 5%, which is an insignificant fraction considering the standard errors (2% to 7%). One can thence ensure that no metabolic deterioration occurred to cells on the experimental time scale. With sufficient nutrients, the saturation of cell number and/or viability was most probably caused by density-dependent contact inhibition [90-94].

2) Wound edge roughness:

Increasing contact inhibition is also related to increased intercellular cohesion, which might introduce uncontrollable geometries to the wound edges which were intended to be straight. The wound geometry can affect the healing efficiency [98], so one needs to examine whether the irregularity of the wound edge geometry has artificially introduced undesirable confounders.

The irregularity of the edge geometry can be quantified by its edge *roughness*, which is related to the fractal dimension of the line [99]. Suppose the edge line is described as the edge height x as a function of its position y in the x-y coordinate system as shown in Fig.3.4 (A). One of the several ways to calculate this roughness is to fit the scaling exponent α in the height-deviation function $G(r) = r^{\alpha}$ of a wound edge line with respect to the window length r. The height-deviation function is defined as follows:

$$G(r) = \frac{1}{N-r}\sum_{i=1}^{N-r}\sigma_i(r),$$

where $\sigma_i(r)$ is the standard deviation of the edge height x_j in a spatial window $y(i) < y(j) < y(i+r)$, where $y(j)$ is the evenly sampled edge positions $y = i$ ($i = 0,1,2,\ldots,N$) along the vertical axis [see Fig.3.4 (A)]. When the exponent α is 1, the edge is perfectly straight; if α is close to zero, the line is rather rough.

For obtaining an intuition about the relationship between the edge roughness and the healing efficiency, a series of wound healing simulations with DRDM was conducted with wave-shaped edges [Fig.3.4 (B)]. The healing data in DRDM suggested that wounds with highly curved edges characterized by small α can heal more rapidly [Fig.3.4(C)], agreeing with the conclusions in the previous literature [98]. Moreover, healing time increases with *roughness* α nonlinearly: for α close to zero (i.e., extremely rough edges), healing time rises rapidly, whereas for $\alpha > 0.1$, healing time climbs slowly, implying that healing efficiency is not so sensitive to the edge geometry unless it is extremely rough. Fig.3.4(D) shows the exemplary height-deviation functions $G(r)$ obtained from the edge data of Experiment I, whose rough exponent α is displayed in Fig. 3.4(E) for group average (dotted circles) and individual samples (open squares). Overall, no significant difference in wound edge roughness could be identified in group

average. Notwithstanding that the variances were large for groups t_w =72 and t_w =96, the absolute individual values of α were all within the range from 0.3 to 0.55. According to Fig.3.4 (C), the healing efficiency is not sensitive to the roughness when $\alpha > 1$. In conclusion, the irregular curvatures of wound geometry caused by increasing intercellular adhesion did not bias the groups with different waiting times in experiments.

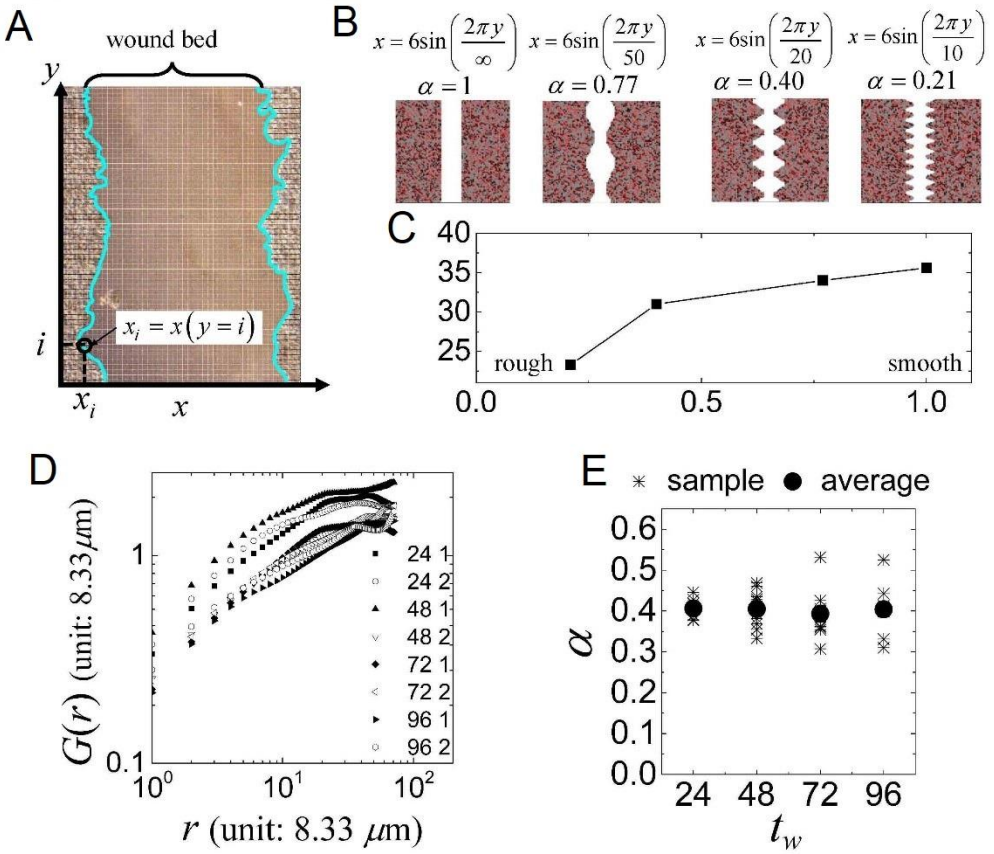

Figure 3.4 Edge roughness in DRDM simulations and *in vitro* experiments. (A) A newly set *x*-*y* coordinate system for quantifying the wound edge (outlined in light green). Sample points $y = i$ are evenly distributed along *y* axis. (B) Roughness exponent α calculated for four wave functions aligned with their wound bed geometries. (C) Wound healing in the DRDM using different edge geometries presented in (B). (D) Sample height-deviation functions $G(r)$ obtained from the edge data from Experiment I. (E) Comparison of edge roughness among four groups (t_w= 24, 48, 72, and 96 h) in Experiment I.

3.2.3 Post-wounding healing

Fig. 3.5 shows the snapshots at three post-wounding time points for four groups with waiting time t_w of 24, 48, 72, and 96h. Groups with longer waiting times exhibited slower healing, which is an indication of bio-aging. Through post-processing of these snapshots, one can describe the healing events from two aspects: the healed area and the density profile.

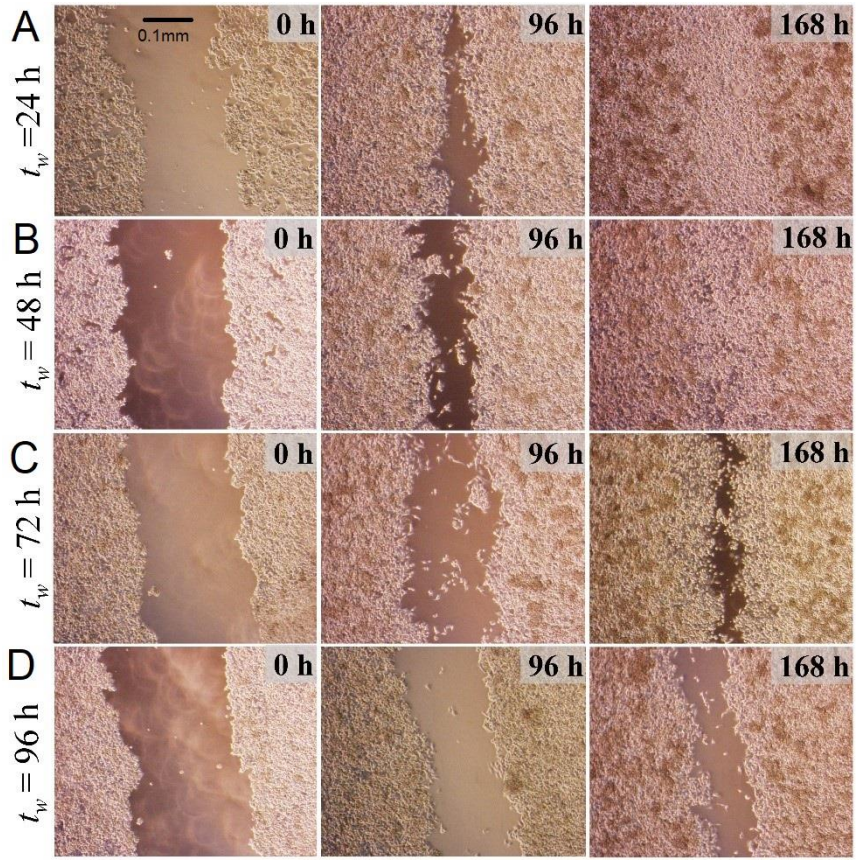

Figure 3.5 Snapshots of 0h, 96h and 168h after the creation of the 0.25mm scratch wound in time-delayed wound healing assays for HepG2.2.15 cells. The dark yellow clots scattered away from the wounds are packed cells.

1) Healed area

The healed area ΔA is calculated as $\Delta A(t-t_w) = A(t_w) - A(t)$, where A is the wound area measured in the unit of 10^5 pixels from the snapshots. Fig. 3.6 (A1) and (B1) show the time evolution of ΔA in different groups with the slope of the curves indicating the healing rate; particularly, a flatter curve illustrates a slower healing process. Obviously, the healing curves become flatter with longer waiting time.

At the first glimpse of Fig.3.6 (A-B), one may think that slow healing for long waiting times is caused by the increase in cell density during the waiting period.

Nonetheless, comparing the healing curves between Experiment I and II, one should notice that Experiment II for the correspondent groups healed more rapidly than Experiment I, implying that the increase in cell density indeed promotes healing efficiency. Besides, one can also compare Group 3 in Experiment I with Group 1 in Experiment II, which have a similar pre-wounding density(3.2×10^7 per well), and find that the Group 3 with a 72-h waiting time in Experiment I healed much slower than the Group 1 in Experiment II with a 24-h waiting time. These comparisons confirm that the density effect that accelerates healing is trivial compared with the aging effect brought by the waiting time.

If rescaling the time axis as $\left(t-t_w\right)/t_w^{\theta}$, where θ is a tunable scaling exponent, one can find that the data of all groups except for Group1 (t_w= 24 h) collapsed to a single curve as shown in the bottom panels in Fig.3.6 (A-B). The scaling exponent θ characterizing the aging rate is 0.72 in both groups. The failure of rescaling in the data of Group 1 in both experiments suggests that there is a dynamical transition from a growth regime (where density effect dominates) to an aging regime which obeys *dynamical scaling*. These findings agree very well with the wound healing simulation in DRDM (refer back to 3.1).

2) Density profile propagation

Shortly after the wound creation, a small number of cells detached from the main body behind and migrated into the wound bed, resulting in the cell density decreasing with the distance away from the original wound edge. To quantify this spatial distribution of cell density, one can segment the image near wound edge into several bins of the same width [Fig. 3.6(C1)] and count the area covered by the cells normalized by the total area in every bin. The positions of those bins are calculated as the distance between the bin center and the wound gap center. Then the bin-based densities should be further averaged over all samples for the bins with the same position.

Fig.3.7 (C2) shows the time evolution of the bin-averaged density as a function of the distance from the wound center for Group 1 (t_w = 24h) and Group 3 (t_w = 72h) in Experiment I. The original wound edge (the half-density position immediately after wounding) calibrated to the zero point of the horizontal axis. One can observe that the density profile propagates at a constant speed into the wound bed like a traveling wave, as is extensively documented in the previous literature [90-96]. The shape of the profile is approximate to a sigmoid curve, yet with a wider low-density head at the forefront, especially for t - t_w >24h. The profile in Group 3 propagates more slowly than that in Group 1; nevertheless, the extension of the low-density head is much longer in Group 3, indicating that the leading cells (at the first row of edge) can migrate into the denuded

area with a similar speed in both groups but the bulk of cells behind the leading edge in Group 3 failed to propagate as rapidly as in Group 1.

The colored shades in the profile in Fig.3.6 (C2) represent the standard deviation of the data drawn with filled area. It is seen that the error ranges are generally large for all sample sets, with the leading low-density heads having the largest variability at

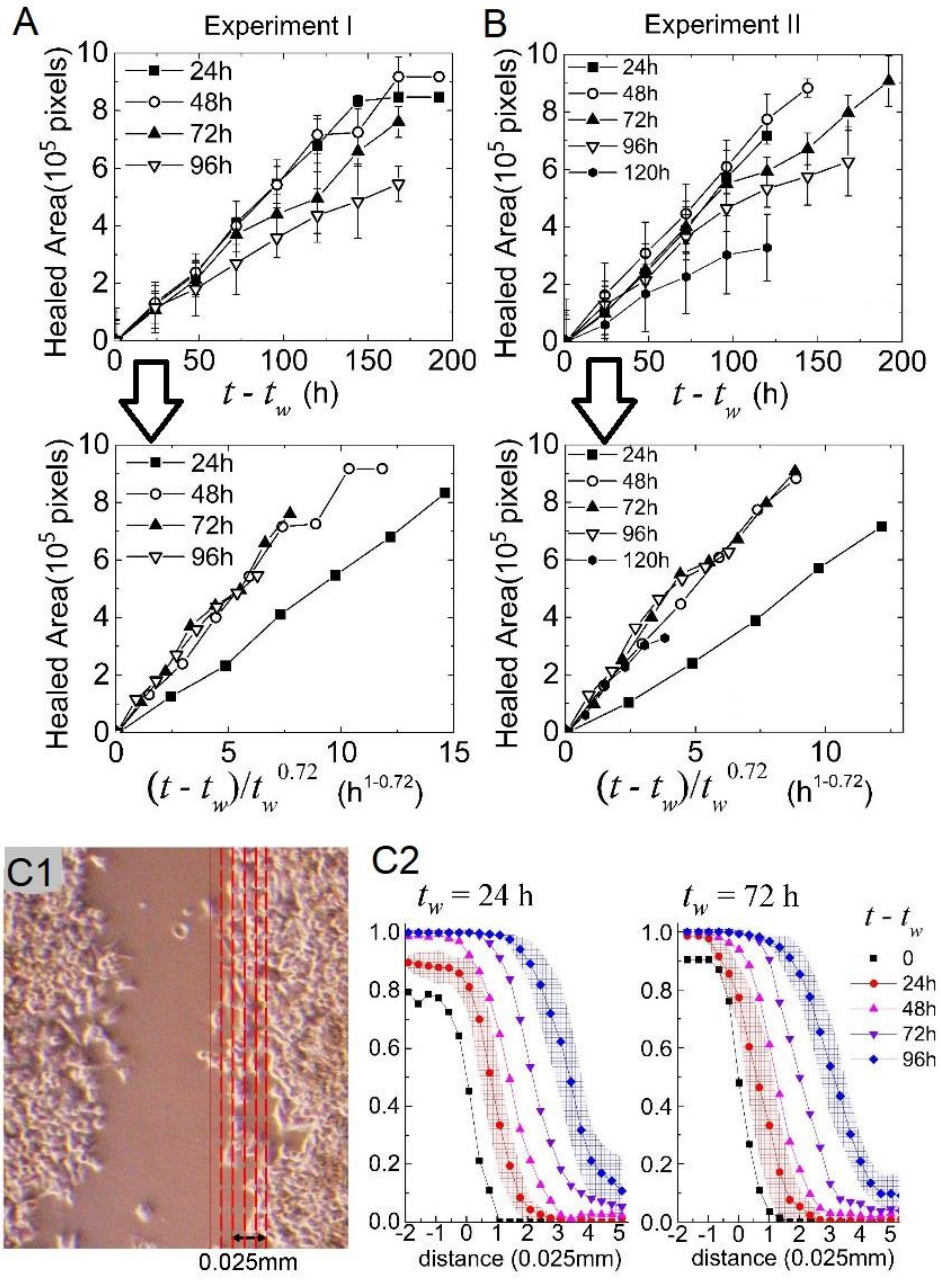

Figure 3.6 Closure of wounds in terms of healed areas and density profiles. (A-B) Healed area as a function of post-wounding time in a normal and rescaled axis for different waiting times in Experiment I (A) and Experiment II (B). (C) The cell density profile in Experiment I:(C1) the bins for density calculation on a snapshot; (C2) the density profile propagation.

$t-t_w$=96h in both groups. This large variance of data is related to the heterogeneity of healing rates across the samples, which peaks at the leading edges. For instance, in some samples [Fig.3.5 (B-C) 96h], several cell clusters detached from the bulk of the cells behind or some finger-shaped heads formed, whereas in other samples [Fig.3.5(A) 96h], the leading edge closed like a zipper. This variance of local healing patterns does not differ very much for short and long waiting times and should be considered as a natural result of some stochastic factors amplified during healing processes with no regard to the waiting time.

3) Summary of experimental results:

From the experimental data, several facts about the role of time in the regeneration of cell sheets under waiting should be concluded as:

(i) During the waiting time, cell density is slowly approaching a saturation level due to the limit of space and cell viability is exponentially decaying to a non-zero value as a possible result of contact inhibition.

(ii) The increase in intercellular adhesion and the accumulation of ECM with time induces no trivial impact on the irregularities of wound geometry.

(iii) There is a dynamical transition from the growth regime to the aging regime where the healing curves fit *dynamical scaling*.

(iv) The density effect is to accelerate healing but is trivial compared with the aging effect.

(v) The slowdown of healing was mainly caused by the slow advancement of cells behind the leading edge.

3.3 Reaction-diffusion models for wound healing

Although both experiments and the DRDM simulations reproduce that the slowdown of wound healing obeys a late onset of *dynamical scaling*, some gap still exists between *in silico* and *in vitro*. On one hand, the physical aging in the DRDM is the consequence of being a critical phenomenon of the normal homeostasis, to form which many parameters are fine-tuned; on the other hand, there could be many unknown mechanisms at the molecular level in the experiments. Therefore, further simplified models are necessary for proposing some testable hypotheses as a guide for pinpointing the key mechanisms in the experiments.

In this chapter, a simple model that bridges the DRDM on the mesoscopic level to the macroscopic experimental phenomena is present. One will see the power of modeling phenomena on multiple scales in its ability to give consistent hypothesis.

3.3.1 Original RDE for wound healing

One of the simplest macroscopic equation-based models for wound healing without waiting is the reaction-diffusion equation (RDE) proposed first by Fisher and Kolmogorov [88] and later verified and extended by many others [90-94]. Wound healing models using RDEs attribute the kinetics of cell density in space to two factors: cell proliferation (reaction) and cell movement (diffusion).

Given a normalized cell density $u(x,t)(0 \le u \le 1)$ at position x in a one-dimensional space at any time t, the time evolution of $u(x, t)$ is:

$$\frac{\partial u}{\partial t} = d\frac{\partial}{\partial x}D(u)\frac{\partial u}{\partial x} + mM(u)u, \qquad \text{(Eq. 3.2)}$$

where $D(u)$ and $M(u)$ are the normalized diffusivity and mitotic rate, repectively; and constants d and m weigh the contributions of the two terms.

Formulation of $D(u)$ has many candidates. In the first proposal by Fisher-Kolmogorov [88], $D(u)$ was set constant. Afterwards, Cai. *et al* [94]have shown with experiments that $D(u)$ should be a monotonic decreasing function with u. Without the loss of generality, one can choose $D(u)$ as follows:

$$D(u) = p/(p+u), \qquad \text{(Eq.3.3)}$$

where $p > 0$ is a coefficient inversely proportional to the strength of contact inhibition. Conventionally, the proliferation term $M(u)u$ takes the form of logistic growth $(1-u)u$ as is first proposed by Fisher. The formulation that the mitotic rate and diffusivity is monotonically decreasing with cell density models the effect of contact inhibition [94].

Given the initial condition $u(*,0) = u_0$, the solution to Eq. 3.2 is a sigmoid function of time for all x, hence the cell density at any t_w immediately before wounding is

$$u(t_w) = \frac{u_0}{u_0 + (1-u_0)e^{-mt_w}}, \text{ with the longtime limit:} \qquad \text{(Eq.3.4)}$$

$$u(t_w \to \infty) \approx 1 - u_0/(1-u_0)e^{-mt_w}. \qquad \text{(Eq.3.5)}$$

Therefore, the cell density approaches saturation with an exponentially decaying speed, agreeing with the experimental findings in Fig.3.3(A).

When a wound is created, the cell density drops to zero in the wound bed, inducing a dramatic density difference at the wound edge. Then the cells start to diffuse from the high-density region to the low-density region at a speed proportional to $D(u)$ while they proliferate at the rate proportional to $M(u)$. The solution to Eq.3.2, i.e., the time-dependent cell density profile $u(x, t)$ is a traveling wave at the wound edge, with the cells at the low-density region having the highest diffusivity and mitotic rate. The

formulation of diffusivity $D(u)$ and mitotic rate $M(u)$ in RDE naturally presumed that the cells can sense the local cell density and response to the appearance of wound instantly. According to Eq.3.4, the impact of the waiting time t_w to the variation in cell density is exponentially approaching zero for large t_w without profound impacts on other parts of the dynamics, hence the original RDE cannot reproduce aging.

Fig.3.7(A) shows the numerical results of original RDE for wound healing with $p = 0, x \in [0,100]$, and a wound condition initialized at different waiting times $u(x^{wound}, t_w) = 0, x^{wound} \in [35,65]$. With waiting time increasing, the healing processes become faster. Because of a longer waiting time, the cell density at the wound edge becomes higher [Fig.3.7 (B1)], which later promotes the cell migration into the wound area and consequently a faster rate of healing [i.e., the red line advances more quickly than the black line in Fig.3.7 (B2)]. The acceleration of healing with cell density agrees to the density effect observed in experiments if the waiting time is controlled [Fig.3.6 (A-B)], i.e., excluding the aging effect.

In conclusion, the original RDE for wound healing that merely involves contact inhibition can only reproduce the density effect.

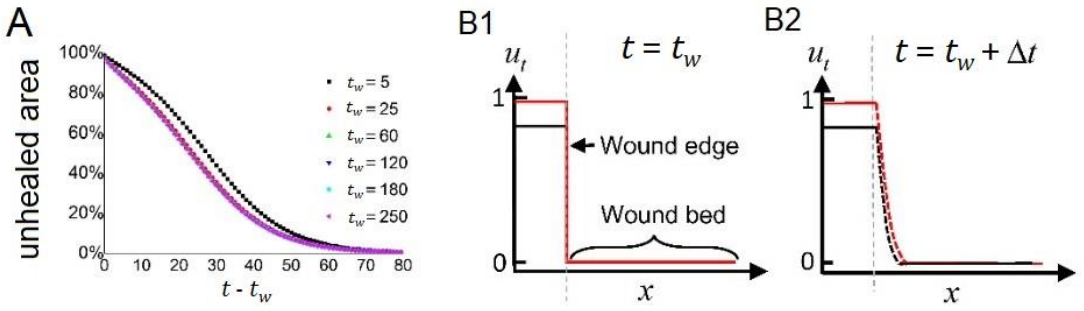

Figure 3.7 Numerical healing results in original reaction-diffusion model. (A) Healing results for different waiting periods under various parameter settings. (B) The cell density profile immediately after wounding for two healing events at different cell densities (the red line for higher density and the black line for lower density). (B1): at t_w (immediately after wounding); (B2): at $t_w + \Delta t$ (a time slightly later than wounding).

3.3.2 Asymmetric RDE for wound healing

To reproduce the aging effect, a strong dependence of the diffusivity and the mitotic rate on the waiting time is necessary. One can think of a situation where the cells at the wound edge cannot resume their diffusivity or mitotic rate immediately; particularly, the longer the cells wait, the slower the response to the wound should be.

1) Delayed-proliferation model

First, consider a model of delayed recovery in the mitotic rate $M\left(u\left(x,t\right)\right)$ for all x

as follows:

$$\begin{cases} M(t) = M_{con}(t), & \text{for } M_{con}(t) \le M(t-\Delta t) \\ M(t) = \delta M_{con}(t) + (1-\delta) M(t-\Delta t), & \text{for } M_{con}(t) > M(t-\Delta t) \end{cases}, \qquad \text{(Eq.3.6)}$$

where $\delta \in [0,1]$ is a delay fraction and $M_{con}(t) = 1 - u(t)$ is the mitotic rate subject merely to the contact inhibition. Indeed, Eq. 3.6 categorizes the dynamics of $M(t)$ into two conditional cases:

If $M_{con}(t)$ is smaller than the mitotic rate at the previous time step $M(t-\Delta t)$, which means that the contact inhibition gets stronger, then $M(t)$ will be reduced to $M_{con}(t)$ immediately as the inhibition of mitosis; otherwise if $M_{con}(t)$ is larger than $M(t-\Delta t)$, which implies a weaker contact inhibition at the current time, $M(t)$ would recover to $M_{con}(t)$ at a delayed pace controlled by the fraction δ. Apparently, the increase and decrease in M depends asymmetrically on $M_{con}(t)$ and thus asymmetrically on $u(t)$. In the extreme case of $\delta = 0$, $M(t)$ can only decrease, thereby modeling an irrevocable cell cycle inhibition. Contrastingly, in the case of $\delta = 1$, the recovery of mitotic ability becomes instantaneous, and Eq. 3.6 returns to the original logistic growth form proposed by Fisher. For $0 < \delta < 1$, which is a more general case, the transition from growth state to arrest state will be faster than its reversal process. In a clearer biological interpretation, δ characterizes how rapidly cells can revive from the state of cell cycle arrest and with such broken symmetry in the growth-to-arrest and arrest-to-growth transitions, the term asymmetric RDE (ARDE) is used to name this model.

The numerical solutions (the density profile) to this ARDE model under different delay fractions and waiting times are exhibited in Fig.3.8. The initial condition is u_0=0.9 and the wound condition is

$$u(x^{wound}, t_w) = 0,\ x^{wound} \in [35, 65].$$

Fig.3.8 (A1) shows that the density profile $u(x, t)$ still keeps a form of traveling wave for a larger δ (A1), while the low-density head of the cell front extends much wider for a small δ (A2). Also, the propagation speed of density profile is also slowed down with a smaller δ. Fig.3.8 (B) shows the comparison of the density profile between two different waiting times with the same value of $\delta = 10^{-5}$. A larger waiting time causes a slowdown of profile propagation, with the stable profile shape having the extended low-density head at the forefront. These results suggest that a small δ or a long waiting in ARDE can slowdown the advancement of the bulk of cells behind the leading edge, in accord with the experimental results [Fig.3.7 (C2)].

The healed area as a function of post-wounding time is displayed in the top panels of Fig. 3.9 (A1-A3) with three different values of δ. In the figures, the vertical axis of graph is the normalized healed area calculated as

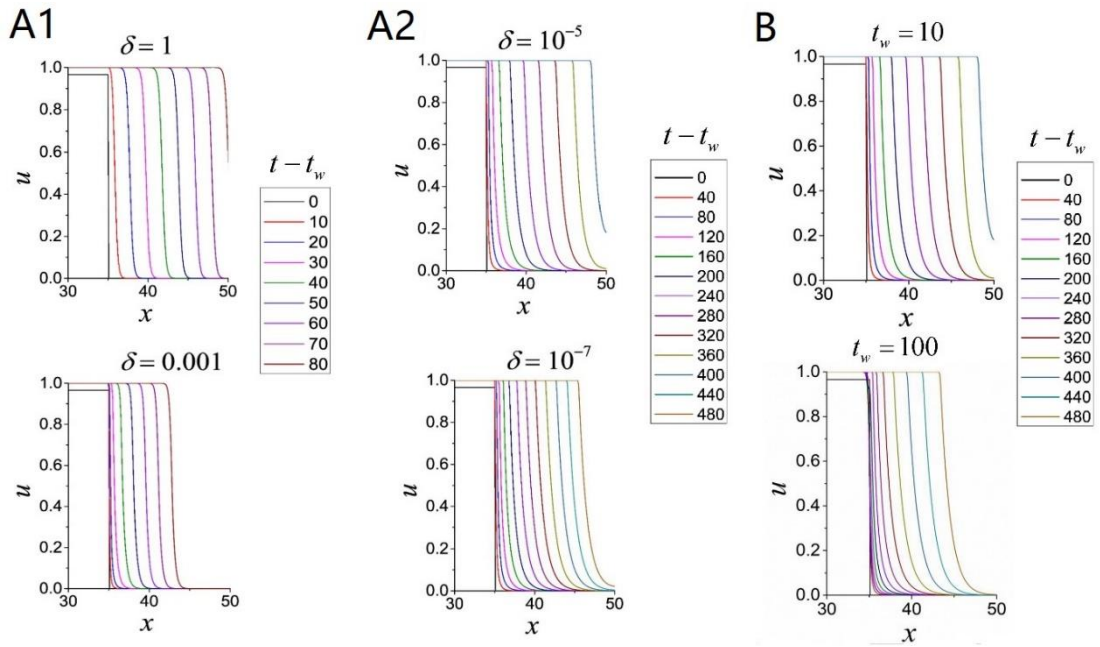

Figure 3.8 Numerical results of the post-wounding density profile propagation in the ARDE model with a delay in the proliferation term solved with u_0=0.9, and d = m = 0.1, p = 0.01 on $x \in [0,100]$: (A1-A2) for different values of delay fraction δ with t_w = 10 and (B) for different waiting times t_w with $\delta = 10^{-5}$. The total wound area ranges from x = 35 to x = 65. Only the left side of the wound edge is shown because the density profiles on two sides are mirror-symmetric.

$\tilde{A}(t) = \frac{1}{|x'' - x'|} \int_{x'}^{x''} u(x,t)\,\mathrm{d}x$, where $x \in [x', x'']$ defines the wound bed.

One can observe a slower increase in $\tilde{A}(t)$ with a longer waiting time in the top panels in Fig.3.9 (A). The lower panels of Fig.3.9 (A) show the healing data with a rescaled time axis. The healing curves with waiting times $t_w > 36$ could collapse to a single curve with scaling exponents dependent on δ, whereas the curves with shorter waiting times (t_w =12, 24) fail to obey the *dynamical scaling* just as the healing events do in DRDM simulations and in the *in vitro* experiments. The decrease in δ from 10^{-5} to 10^{-7} and 10^{-9} induces an increase in the scaling exponent (roughly from 0.48 to 2.33 and 4.35), manifesting the role of δ in controlling the deterioration of healing efficiency.

The reason why a near-zero δ can render a huge aging exponent can be inferred from the asymptotic analysis of mitosis rate $M(u)$. Assuming that all cells in the wound area only experience delayed recoveries of mitotic rate and assuming that cell diffusion is negligible, one can derive the following time evolution equation of $M(u(t))$ from Eq.3.6:

$$M(t,t_w) = \int_{t_w}^{t} \delta(1-\delta)^{t-t'} \left(1-u(t')\right)\mathrm{d}t' + (1-\delta)^{t-t_w}\left(1-u(t_w)\right). \qquad \text{(Eq.3.7)}$$

Eq. 3.7 consists of two terms: a convolution from t_w to t and a contribution from the density $u(t_w)$ immediately before wounding. Apparently, a small δ will reduce the impact from the convolution term, and in the extreme situation $\delta = 0$, $M\left(t,t_w\right)$ is reduced to $1-u(t_w)$, which approaches $\exp(-mt_w)$ in the limit of $t_w \to \infty$. The exponential decay in the mitotic rate M with t_w implies an exponential divergence of healing time with t_w, in which the scaling exponent is infinite [also demonstrated by Fig.3.11(B) and see the discussions in Ch. 3.3.3].

2) Delayed-migration model

Cell migration can also be suppressed by the increased cell density or the accumulation of cell-cell or cell-ECM adhesion [89-94,95,96]. Previous literature reveals that the motility of the cells will change over time [113] in a confluent cell sheet and the mechanics related to the migratory ability of the cells at the wound edge influence the wound closure efficiency [100-103]. In a similar way to Eq.3.6, one can realize a delay in the cell migration as follows:

$$\begin{cases} D\left(t\right) = D_{con}\left(t\right) & \text{for } D_{con}\left(t\right) \le D\left(t-\Delta t\right) \\ D\left(t\right) = \pi D_{con}\left(t\right) + \left(1-\pi\right) D\left(t\right) & \text{for } D_{con}\left(t\right) > D\left(t-\Delta t\right) \end{cases}, \qquad \text{(Eq.3.8)}$$

where π from 0 to 1 is the delay fraction for the diffusivity.

Fig.3.9 (B1) shows that the wound heals more slowly for $t_w = 0$ with a smaller π. Nonetheless, even if π is set to zero (meaning an irreversible decrease in the cell motility), the aging effect is still not observed [Fig. 3.9(B2)].

This result seems to contradict with the previous literature in which the emergence of non-proliferative spreading cells at the leading edge (around which lamellipodia can be found and their motility was reported to be crucial for healing efficiency [89,100-103]). In ARDEs, such spreading cells are not modeled. To test whether this absence of spreading cells can explain the loss of the aging effect, one can add the sub-model of spreading cells by multiplying a Heaviside step function $H(\lambda-D(x))$ to the original mitotic rate in Eq. 3.8. When the cells have a diffusivity D larger than λ, they will have zero mitotic activity.

The new parameter $\lambda > 0$ controls the length of the region dwelt by the spreading cells. Since these cells only appear in the front rows of the wound edge, λ should be small compared with the diffusivity coefficient d. Fig.3.9 (B3) shows the healing curves for λ=0.001 (black) and λ=0.01(red) in the case of $\delta = 1$, $\pi = 0$ for various waiting times. By comparing Fig.3.9 (B2) and (B3), one can find that when λ is small, the role of spreading cells is negligible. The healing processes apparently appear slower with a larger λ, yet still no significant aging effect is observed.

If further considering a reproduction of the extended heads in the density profiles as is shown in the experiments, one should apply the wake-up dynamics (Eq.3.8) specifically to the bulk of cells behind the leading edge, which will make the

unnoticeable aging effect even more trivial (results not shown).

The failure of reproducing aging by a "wake-up" mechanism in the cell migration term is be attributed to the fact that the diffusivity D does not decrease radically with large waiting times [because the diffusivity D takes the form of $p/(p+u)$]; in fact, any monotonic decreasing function of u satisfying $D(u=1) > 0$ cannot reproduce aging]. To induce an aging effect by modifying the diffusion term in the RDE models, one needs extra assumptions such that the diffusivity coefficient d decreases or the range of spreading cells λ increases radically with the waiting time in a specific fashion, which is lacking in evidence. Though the inhibition of cell locomotion due to the densification of the confluent cell sheets in short-time observation has been reported [109,111,113],

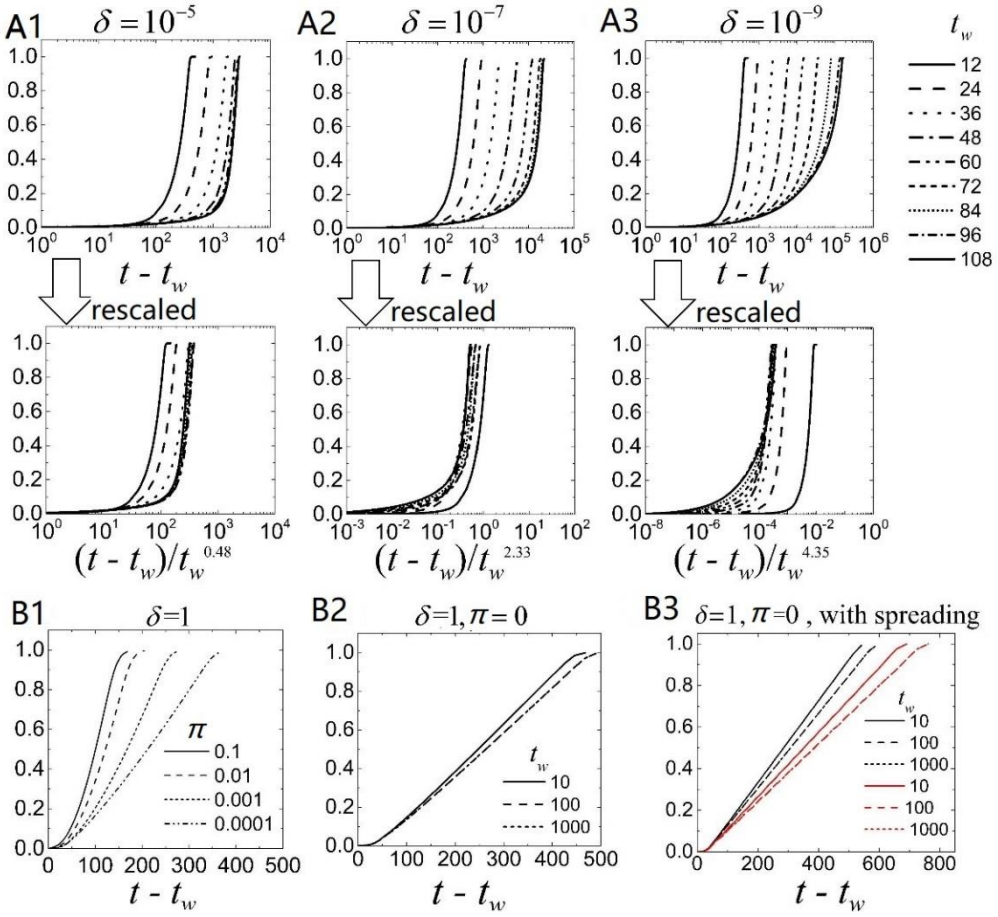

Figure 3.9 Numerical results of the normalized healed area as a function of post-wounding time in asymmetric reaction-diffusion equation (ARDE) model with $d = m = 0.1$, $u_0 = 0.5$, $p = 0.01$.The vertical axes represent the normalized healed area A. (A1-A3) For three values of the delay fraction δ in the proliferation term. Note that the x-axes are on logarithmic scales. (B1) For different values of the delay fraction π in the diffusion term with $t_w = 0$. (B2) For different values of waiting times. (B3) For different values of waiting times with the modeling of spreading cells. The black curves refer to $\lambda = 0.001$; the red curves refer to $\lambda = 0.01$, where λ is the length of the region occupied by the spreading cells.

the cell proliferation and the remodeling of ECM were not triggered in these experiments. For healing processes longer than the cell doubling time, which is 24h for HepG2.2.15 cells in our experiments, these issues regarding the role of cell migration still need more experimental investigations.

In DRDM simulations, the cell motility is also not critical for the slowdown of healing. The effect of delayed recovery in cell movement can also be examined by varying adhesion threshold *h*, which represents the minimal level of cell-cell and cell-ECM adhesion required to cease cell movement in its local surroundings. In Fig.3.10 (A), the adhesion threshold *h* was set to infinity, indicating that cell movement is totally free. Meanwhile, the growth threshold *g* was set as $0.3R_M$ which is a huge barrier for the cells to re-enter the growing state from an arrested state. The results revealed that even with the freest cell movement, a strong regrowth barrier still causes the slowdown of healing with short waiting times and the incomplete healing with longer waiting times. Conversely, if *h* is 0, which means zero cell motility due to a strong cell-cell and cell-ECM adhesion, a small value of *g* could still ensure a quick healing process, as shown in Fig.3.10 (B), nevertheless, with the cliff-shaped healing curves. This comparison illustrates that the role of mitotic deterioration is much more significant than the role of retarded cell movement in reproducing the slowdown of healing in DRDM. Besides, one can clearly see that the reduced cell motility causes a "frozen" phase before the initiation of healing in Fig.3.10 (B). This also implies that the role of delayed cell migration is to postpone the initiation of cell regrowth in the early stage of healing. Yet these "frozen" phase and cliff-shaped healing curves cannot be seen from the experiment, hence it is very unlikely for the cells to have low motility with a high proliferation rate in the experiments with current settings.

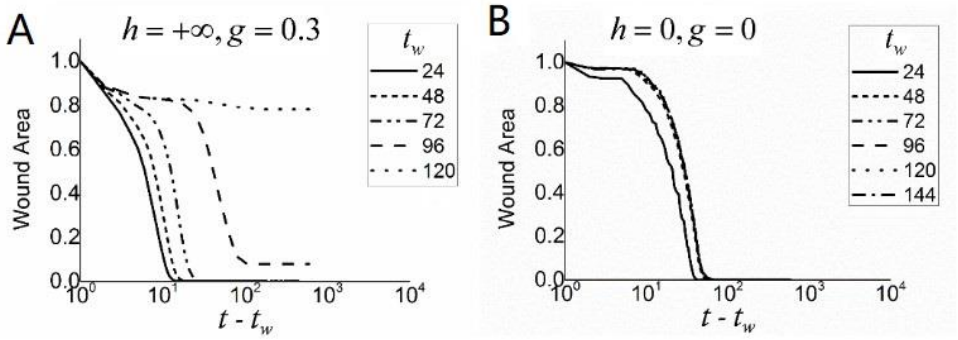

Figure 3.10 Wound closure in the discrete receptor dynamics model (DRDM). (A) Free cell movement ($h \to \infty$) with a high regrowth barrier ($g = 0.3R_M$). (B) No cell motility ($h = 0$) with no regrowth barrier ($g = 0$).

3) Summary of ARDE modeling for wound healing

The delayed recovery of cell proliferation in ARDE models can well reproduce the

dynamical scaling of the waiting-time-dependent healing events (including the dynamical transition from growth to the aging regime) and the slow propagation of the cell fronts with an extended low-density edge. By contrast, the delayed migration model cannot induce aging phenomenon without introducing extra assumptions on the evolution of other parameters. Nevertheless, considering that the cell motility and cell cycle dynamics are coordinately regulated by a complex signaling network of intracellular molecules, one should be aware that the slowdown of healing is a combined consequence of the mechanical and biochemical factors.

3.3.3 Criticality analysis

According to the theory of physical aging, if the system's relaxation time is sensitive to a parameter within its critical range, this parameter can control the speed of aging [82-84]. Therefore, criticality analysis can help one identify the control parameter of the systems. In this section, I will compare the criticality analysis of ARDE and DRDM to help infer the consistent controller of multicellular aging.

1) Criticality in ARDE

The criticality analysis is to examine the power-law relationship between the control parameter δ and complete healing time τ, where τ is defined as the time when the wound area shrinks to $\tilde{A}(t) > 99\%$. Fig.3.11 (A) illustrates the divergence of τ with δ under different values of $u(t_w)$. A larger value of $u(t_w)$ corresponds to stronger contact inhibition due to a longer waiting time, as shown in Eq. 3.5. The algebraic divergence $\tau \sim (1/\delta)^{\beta}$ resembles the criticality in physical systems with the critical point at $\delta = 0$, even though the divergence crosses over to a ceiling for a small δ. A larger wounding density $u(t_w)$ postpones this crossover, suggesting that the critical role of δ is manifested under strong growth inhibition (caused by higher cell density). The reason

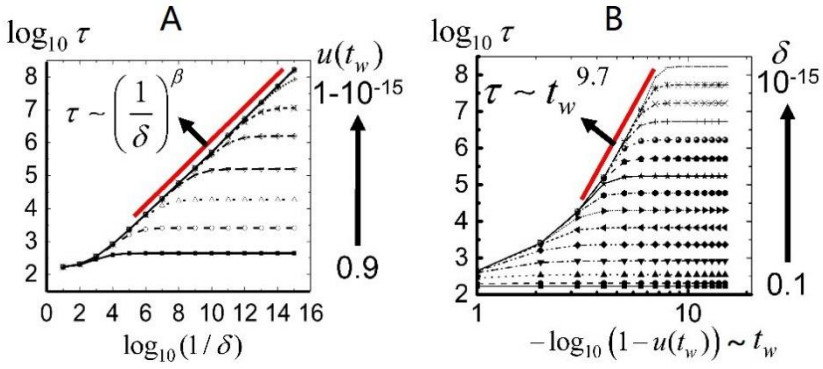

Figure 3.11 Critical behaviors in ARDE. (A) The divergence of healing time τ with delay fraction δ, under varying cell density at wounding time $u(t_w)$. (B) The divergence of healing time τ with the waiting time t_w under varying delay fraction δ.

for the ceiling lies in that as δ decreases, the second term in Eq. 3.7, which involves $u(t_w)$, becomes more dominant in M (t, t_w), and thus τ diverges as $\tau \sim \exp(mt_w)$ independently of δ. Under stronger contact inhibition, i.e., $u(t_w)$ closer to 1, the convolution term in Eq. 3.7 can take effect with a smaller δ, and thus extends the range of critical regime.

To evaluate the value of the critical exponent β, the local derivatives of log τ is calculated as a function of δ from a series of data $\tau(\delta_i)$, where i =1,2,…,N satisfying $\delta_{i+1}/\delta_i = 0.1$ as: $\Delta(\delta_i) = \left(\log_{10}\tau(\delta_{i+1}) - \log_{10}\tau(\delta_{i-1})\right) / \left(\log_{10}\delta_{i+1} - \log_{10}\delta_{i-1}\right)$.

Fig.3.12(A) shows that the value of $\Delta(\delta)$ has three regimes with $\log\delta^{-1}$: $\Delta(\delta)$ rises from zero first, then encounters a plateau and finally returns to zero. For small $u(t_w)$ (low contact inhibition), the regime with a stable plateau, which indicates a power-law relation $\tau \sim (1/\delta)^{\beta}$, is absent; for $u(t_w)$ extremely close to 1 (high contact inhibition), the stable regime exhibits two sub-regimes with the first plateau roughly at $\beta = \Delta(\delta) = 0.469 \pm 0.002$ and the second one at 0.5. The existence of such staircase in the plateau regime is confirmed with various model parameters under $u(t_w)=1-10^{-15}$ [Fig.3.12 (B-C)], where the first plateau is universally around $\beta = \Delta(\delta) = 0.471 \pm 0.009$, yet the onset timings of the second plateau are diverse. Meanwhile, the data groups with

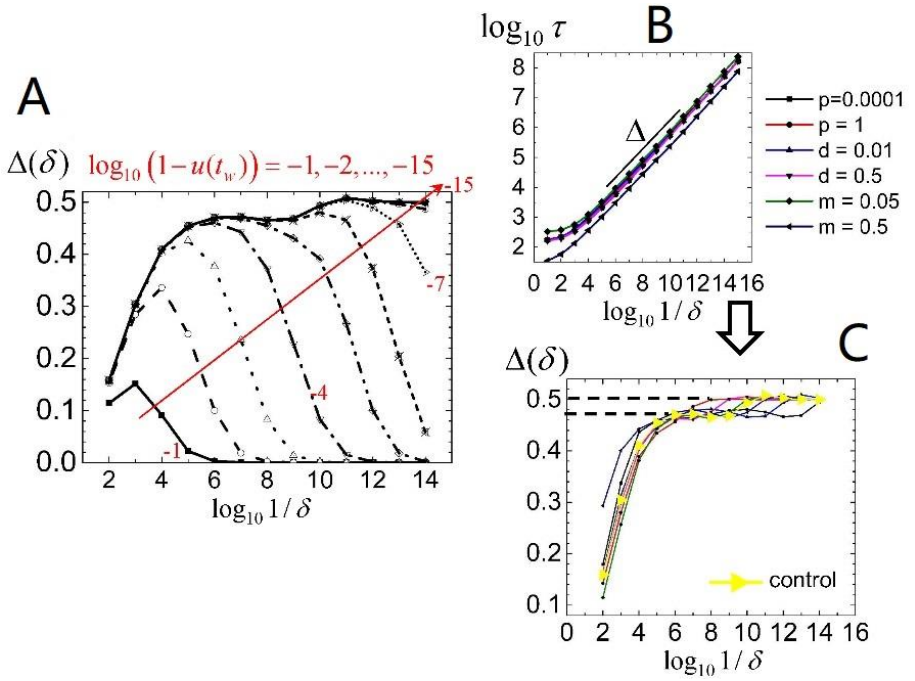

Figure 3.12 Estimating critical exponent of ARDE.(A)The derivatives of log τ as a function of delay fraction δ calculated from a series of data τ (δ_i), i =1, 2,…,N under various $u(t_w)$ with the parameter setting $m = d = 1$, $p = 0.01$ (used in all numerical simulations for Fig.3.8, Fig.3.9 and Fig.3.11). (B) Divergence of $\log\tau$ with other parameter settings under high contact inhibition $u(t_w) = 1-10^{-15}$. (C) The derivatives of log τ calculated from the curves in (B) compared with the control group ($m = d = 1$, $p = 0.01$).

smaller *p*, smaller *d*, and larger *m* tend to exhibit longer first plateaus, implying that the first plateau with lower β is more associated with the mitotic term in ARDE; by contrast, if the diffusional dynamics is dominant (larger *p*, larger *d*, and smaller *m*), the second plateau, i.e., $\tau \sim \sqrt{1/\delta}$ will quickly ensue.

Fig.3.11 (B) shows the relationship between $\log\tau$ and $\log\left(1-u\left(t_w\right)\right)^{-1}$ for a series of δ. One may note that $\log\left(1-u\left(t_w\right)\right)^{-1}$ is asymptotically proportional to t_w according to Eq. 3.5. The aging regime, in which τ increases with t_w in power law, also crosses over to a ceiling. The speed of divergence of τ depends on the value of δ: a rapid divergence indicative of a dramatic aging corresponds to an extremely small δ and the aging exponent can be very large (e.g., the $\tau \sim t_w^{9.7}$ highlighted in red). Additionally, there is a dynamical transition from the growth regime where τ diverges exponentially with t_w to the aging regime obeying power-law under smaller δ.

The vanishing of aging effect at extremely long waiting times originates from the existence of cell diffusion. When cell density approach the saturation level($u \to 1$), the number of diffusing cells $\nabla\left(D(u)\nabla u\right)$ from the wound edge immediately after wounding converges to a nonzero value $\left(D\left(u\to 1\right)+D\left(u\to 0\right)\right)/4$, asymptotically. The small number of cells migrating from the wound edge to the wound bed as an instant response to wounding is independent of $u(t_w)$ in the longtime limit:

$$\frac{\mathrm{d}u}{\mathrm{d}t}=\nabla\left(D\left(u\right)\nabla u\right)\sim\frac{1}{4}\left(D\left(u\to 1\right)+D\left(u\to 0\right)\right)\approx\frac{2p+1}{4\left(p+1\right)}.$$

Therefore, the instantaneous recovery of $M(u)$ for cells in the wound bed converged to a non-zero rate when the waiting time approaches infinity as follows:

$$\frac{\mathrm{d}M\left(t_w\right)}{\mathrm{d}t}=\mathrm{d}M\left(u(t_w)\right)/\mathrm{d}t=\delta\mathrm{d}u(x^{wound},t)/\mathrm{d}t=\delta(2p+1)/4(p+1).$$

This leads to a vanishing of aging effect ($\mathrm{d}M(u)/\mathrm{d}t$ irrelevant to t_w). Such a ceiling for criticality is almost inevitable in models where cell movement is driven by any existent density differences, even if in these two extremal circumstances:

(i) The diffusivity recovers at a delayed pace such that:

$D\left(t\right)=\pi D_{con}\left(u(t)\right)+\left(1-\pi\right)D\left(t-\Delta t\right)$, where $D_{con}(u)$ can be any ideal diffusivity purely under contact inhibition at cell density *u* satisfying (ii), and π, ranging from 0 to 1, is the delay fraction imposed on the diffusion term;

(ii) $D_{con}(u\to 1) \to 0$.

The reason is as follows: the instantaneous number of cells that migrate into the wound immediately after wounding depends on two terms $D(u\to 1)$ and $D(u\to 0)$, representing the cell diffusivity on the wound edge and in the wound bed, respectively. Even if $D(u\to 1)$ (at the edge) approaches zero with large waiting time t_w, $D\left(u=0,t_w+\Delta t\right)$ can asymptotically converge to a minimum of a non-zero value in the longtime limit as:

$$\pi D_{con}(u \to 0) + (1-\pi) D(t_w \to \infty)$$
$$= \pi D_{con}(u \to 0) + (1-\pi) D(u \to 1) \approx \pi D_{con}(0) + (1-\pi) D_{con}(1),$$

which is not sensitive to t_w. Clearly, the onset of the ceiling regime and the vanishing of aging effect at extremely large waiting times is inevitable for the ARDE models. In real experiments, incomplete healing may instead occur for such long waiting times (see Ch.3.4).

2) Criticality in DRDM

As is observed in the Fig.3.1(C), the shift of subpopulation structure is critical to the onset of physical aging. Yet, the dynamics of the subpopulation structure in DRDM are affected by multiple factors, including cell-ECM adhesion, cell-cell adhesion, cell polarization, regulation of cell-cycle arrest, apoptosis, and cell movement. Therefore, a criticality analysis is done to identify which are the critical ones to aging. Since apoptosis is negligible in the *in vitro* cell monolayer formation, only the effects of the ECM threshold *e*, polarization threshold *p*, arrest threshold *a*, and growth threshold *g* are examined.

Healing time $\tilde{\tau}$ in the DRDM simulation is defined as the time when 90% of the wound sites are re-occupied by cells, and is measured for different sets of *e*, *g*, *a*, and *p*. As Fig.3.13 (A) reveals, *e* and *g* are the two most critical factors that slow the healing; by contrast, *p* and *a* play insignificant roles in aging [Fig.3.13 (B)]. However, the abrupt jump of $\tilde{\tau}$ from roughly 50 steps to infinity corresponds to the emergence of incomplete healing, which is a complex issue that can only be reproduced in the DRDM and not found in ARDE. I will leave the discussion of incomplete healing to Ch.3.4.

The dependence of healing efficiency on the ECM threshold *e* [Fig.3.13 (C2)] shows that the ECM plays a role in the slowdown of healing. In the DRDM, a lower value of *e* induces a quicker polarization that may lead to cell cycle arrest, suggesting that the accumulation in ECM induces the slowdown of healing in DRDM through promoting cell cycle arrest. The growth of ECM in DRDM can meanwhile affect the cell motility. Nevertheless, as we have shown in Fig.3.10 (Ch.3.3.2.) that the loss of cell mobility cannot lead to a significant aging effect in DRDM. Hence, the aging effect associated with ECM here is caused by cell cycle arrest instead of the mechanical reasons.

Healing times diverge continuously with *g* as a power-law $\tilde{\tau} \sim g^{\tilde{\beta}}$ for small *g* [Fig. 3.13(C1)]. Clearly, 1/*g* serves as a control parameter like the delay fraction δ in ARDE [see Fig.3.11(A)], and for both, the criticality vanishes for smaller1/*g* and δ. However, the value of critical exponent $\tilde{\beta}$ in DRDM is varying with other parameters such as various ECM thresholds *e* [Fig.3.13 (C2)] and various arrest thresholds *a* [Fig.3.13 (D)], indicating that *g* is not as dominant as δ for the emergence of dynamical scaling.

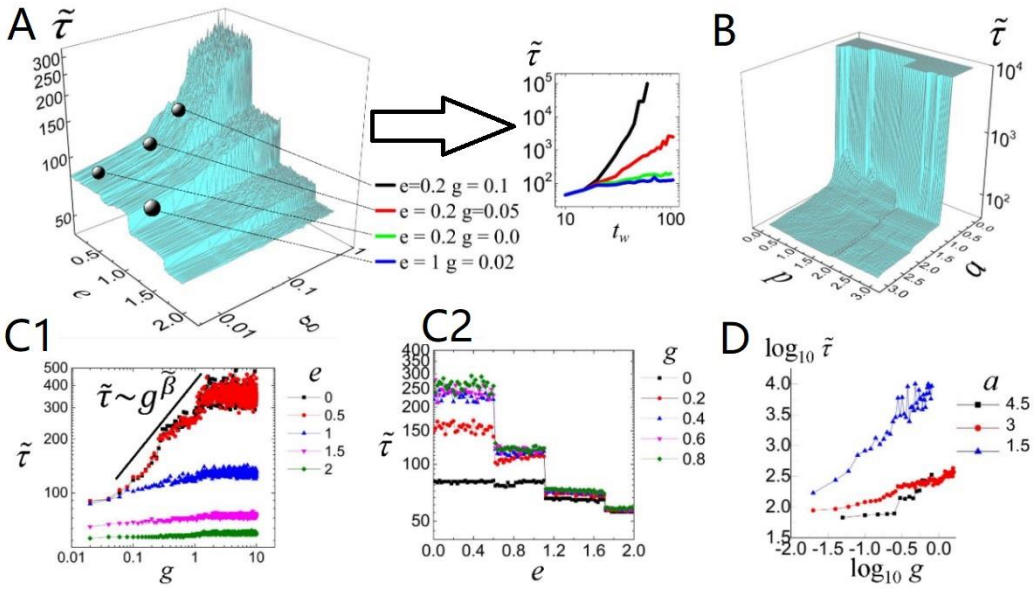

Figure 3.13 Critical behaviors in DRDM for different parameters. All wounds are set to be performed at 10 steps after the start of the simulation. The thresholds e, g, p, a are in the unit of R_M, which is the receptor amount required for mitosis. See APPENDIX B(3) for other parameters. (A) Healing time $\tilde{\tau}$ in relation to e and g. The right panel: the log-log plot of $\tilde{\tau}$ versus t_w with four pairs of $\{e,g\}$ marked as the black balls on the 3D diagram. (B Healing time $\tilde{\tau}$ in relation to p and a, with e fixed at $0.8R_M$ and g at $0.05\ R_M$. The infinitely diverged values of $\tilde{\tau}$ are truncated to 10^4. (C) The 2D log-log plot of $\tilde{\tau}$ versus g under various e (C1) and the log-linear plot $\tilde{\tau}$ of versus e under various g(C2). (D) The divergence of $\tilde{\tau}$ as a function of g for different arrest thresholds a, with $e = 0.8\ R_M$.

3) Essential interdependence structure: restriction asymmetry

Although DRDM and ARDE are models at distinct scales, the control parameters revealed by the criticality analysis in the two models have similarity in essence. In DRDM, growth threshold g determines the asymmetry of the regulation in the restriction point (a checkpoint for entry and exit of cell cycle arrest): entry into arrest depends only on the arrest receptors, whereas the exit from arrest requires additionally the growth receptor amount exceeding g [Fig.3.14 (A)]. When g is zero, entry into and exit from cell cycle arrest are governed solely by arrest receptors, i.e., the transitions between growth and arrest become symmetric. Otherwise, for any non-zero g, quiescent cells must have their growth receptor amount overcome an extra barrier of g. If g is too large, cells can rarely revive from cycle arrest. The arrest-to-growth (or the growth-to-arrest transition) in DRDM cells is exactly a more detailed representation of the increase (or decrease) in the mitotic rate M in the ARDE (Eq.3.6), and the growth threshold g in DRDM, similar to that of δin the ARDE [Fig.3.14(B)], controls the aging rate [referring to the inset of Fig.3.13(A)]. In addition, just as the critical role of $\delta$is more prominent under stronger contact inhibition in ARDEs [Fig.3.11 (A)], and the criticality or aging in DRDM controlled by g is likewise more apparent under growth-inhibitive conditions,

such as a low ECM threshold [Fig.3.13(C1)], a low polarization threshold (a sensitive polarizing response to cell-cell adhesion; results not shown here), or a low arrest threshold, i.e., a strong cell-arrest regulation [Fig.3.13(D)]. Since the delay fraction δ has been substantiated by the growth threshold g in many aspects, we can interpret the critical parameter for bio-aging in the wound healing context as *restriction asymmetry*, which means the degree of asymmetry between the growth-to-arrest and arrest-to-growth transitions in cell cycle governed by the restriction point.

For the real control parameter in the experiments, it could correspond to the time a cell needs to get cycle arrest over the time it needs to wake up from the quiescence. And this can be measured both for a single cell or a population of cells. To this point, a very clear hypothesis that can be falsifiable by experiment is proposed.

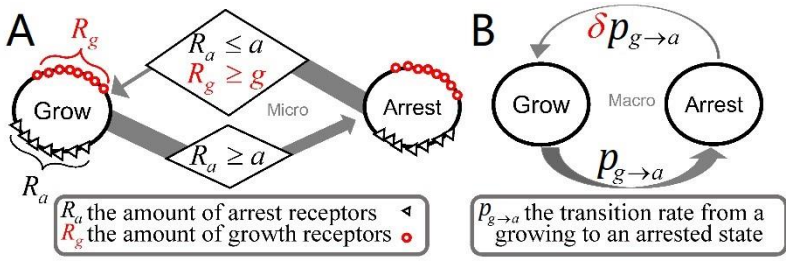

Figure 3.14 The essential interdependence structure for multicellular aging in DRDM (A) and in ARDE (B). The thickness of the arrows represents the transition rate.

3.4 Incomplete healing *in vitro* and *in silico*

The most eminent discrepancy between the DRDM and the ARDE model lies in the ability to reproduce the heterogeneous healing rates at the leading edge and the incomplete healing phenomenon. In the ARDE model, the varying ability of cell proliferation and migration depends only on the cell density, suggesting that the cells have the potential to grow and move ($D(u) > 0$, $M(u) > 0$) as long as any unhealed space with cell density $u < 1$ remains. By contrast, in the DRDM, the inhibition of cell growth and cell mobility depends not only on cell density, but also on the adherent cohesion among cells, the sensitivity to ECM, and on the intrinsic regulation for cell cycle arrest. These sophisticated factors yield a huge diversity of cell phenotypes in DRDM, resulting in heterogeneous healing behaviors along the wound edge. As shown in Fig.3.15(A) and (B), some of the leading cells invade into the wound bed quickly while others remain inactive, producing some finger-shaped healing fronts. Although the

macroscopic cell mitotic rate averaged along the whole edge should be equivalent to $M(u)$ in the ARDE model, this equivalence holds only for smaller waiting times when more cells are viable with less heterogeneous cell phenotypes.

The heterogeneity among cell phenotypes profoundly affects the healing processes when the waiting time is long enough, causing incomplete healings in DRDM especially with **a low arrest threshold *a*, i.e. a higher tendency for cell-cycle arrest**. As a result, healing was totally ceased in the middle of the process [Fig.3.15(C)], leaving the wound areas unhealed. To understand this phenomenon, one can imagine an extremely unfortunate case where no cell on the wound edge is reactivated to proliferate or move. This occurs when very few cells are active in the system with a finite number of total cells, hence the averaged mitotic rate along the edge can only decrease in a quantum manner with longer waiting times: jumping from a small value to zero. Even if the finger-shaped edges can form, a lower value of arrest threshold *a*, which indicates strong inhibition of cell cycle, will gradually suppress the mitosis of the cells during the healing, thus preventing the cells at the "finger" from further invasion into the denuded area.

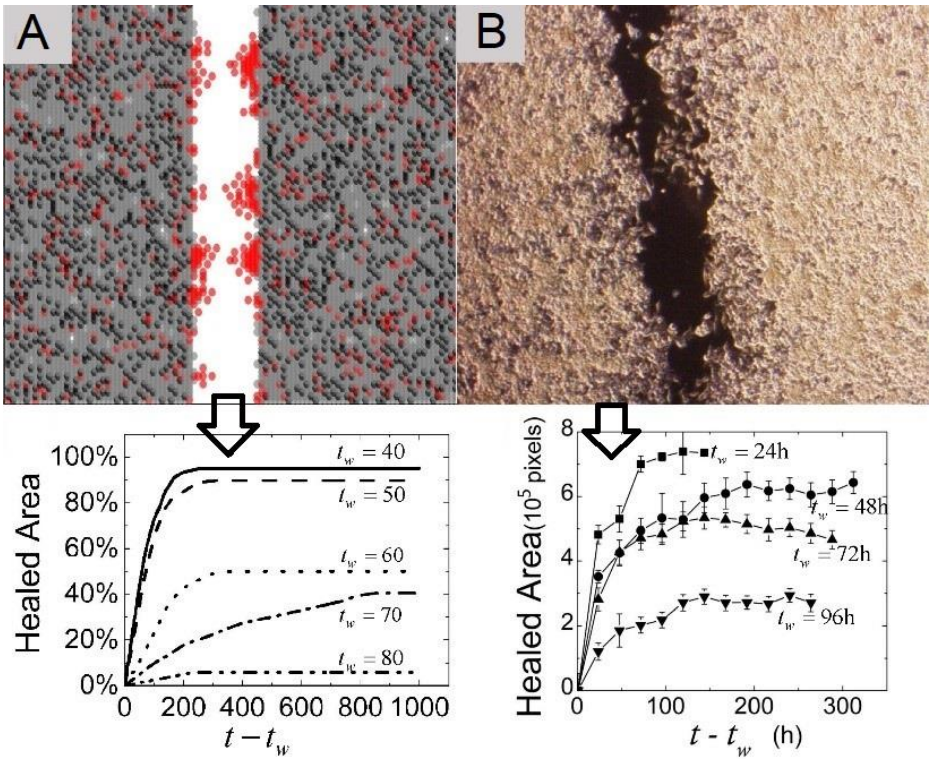

Figure 3.15 Incomplete healing phenomena (A) In DRDM simulation Red dots: proliferating cells; grey dots: temporarily arrested cells, black dots: permanently arrested cells. (B) *In vitro* experiment with cells subcultured for 40 generations.

In fact, incomplete healings have been observed in another series of experiment with a cell line of HepG2.2.15 subcultured for about 40 generations, i.e., these cells were “old” in contrast to the newly thawed cell line used in Experiments I and II (in the Ch.3.2). The reason of incomplete healing *in vitro* is unclear so far; yet, by associating with the incomplete healing phenomena in DRDM, it can be postulated that the accumulation of the damages to the cells over generations can correspond to the decrease in arrest thresholds in the DRDM simulation. Accordingly, the incomplete healing may be caused by the strong cell-cycle inhibition in experiments and it should occur for two kinds of cells: 1) the old cells which inherently have low arrest thresholds; 2) the newly thawed cells with extremely long waiting time, which have higher arrest thresholds but accumulate excessive non-degradable “arrest receptors” over time.

3.5 Analogy between bio-aging and physical aging

As is advocated in the previous results, multicellular aging behaves like the relaxation processes in nonequilibrium systems such as glasses. Over the past decade, the analogy between glassy or jammed materials and cellular sheets has been studied on the basis of mechanobiology [107-112]. Many glass-like mechanics such as dynamic heterogeneity, cooperativity, and kinetic arrest seem to prevail in living systems or active matters [114]. Although the interdependency and causality between the glass-like mechanics and the biological aging are not fully clarified, it is possible to establish an analogy between the slowdown of healing in the cellular sheet and the slowdown of relaxation in physical systems based on the current findings in experiments and simulations. Both of them conform to the *dynamical scaling* and the control parameter for wound healing, the *restriction asymmetry* which is identified by two wound healing models at different scales, can have many similarities with the physical control parameters like temperature, density, etc.

The analogy between the two types of aging can be articulated with the *trap* model [104]. In a system with many particles (or cells), each particle (or cell) senses a local energy trap (or a biochemical trap that induces cell cycle arrest) formed by neighbors (or ECM, cell-cell adhesion), the escape from which requires more effort than does entering into it. When the control parameter approaches a critical value, the barrier of the traps will become so high that the system dynamics may easily be captured in the local minimum of the energy landscape. In this analogy, the two systems based on disparate dynamics resemble each other, having a common definition of the control parameters as the ratio of the effort required to fall into a trap (arrest) to the effort required to escape. Typically, when this ratio is small (e.g. low temperature, high density in physical systems and small δ in ARDE), the dynamics of the particles (or cell

cycles) tend to be arrested and the system loses the ability to relax in physical systems (or to regenerate in biological systems).

Nevertheless, due to the low time resolution and the short observation timescale of the current experiments of TDWHAs, a finer comparison between the slowdown of healing and the slowdown of relaxation events in physical systems is limited, thus leaving many unclarified issues associated with the analogy between two types of aging. For instance, dynamical scaling of physical aging is believed to originate from the symmetry of time-spatial local scale invariance [105-106], a property that currently has not found its biological counterpart yet. Also, the scaling exponent of physical aging typically ranges from 0 to 1, whereas in the proposed ARDE, this exponent can be far greater than 1 when δ is close to zero; this suggests a possibility that the exact scaling of the healing curves might be exponential to the waiting time, instead of power-law. Meanwhile, the criticality around the critical point of the control parameter found in the biological model is restricted and influenced by many other factors such as cell movement, cell-ECM interactions, cell polarization among others, implying that the living systems with tremendous complexity might be no perfect analog of any physical systems. Finally, the concepts of equilibrium and relaxation in physics (associated with ergodicity and a process of reaching ergodicity) do not rigorously correspond to tissue homeostasis and regeneration (where only non-ergodic steady states are possible) and it is unclear to what extent this fundamental discrepancy could falsify the analogy and impair its application prospects. Future studies of TDWHAs should involve various cell lines and experimental settings at higher time resolution and with longer waiting periods for clarifying the detailed mechanism underlying the slowdown of healing and for better translating the theory of physical aging to bio-aging problems.

3.6 Summary of Chapter 3

Being close to the critical state, multicellular aging is a nonequilibrium critical phenomenon showing *dynamical scaling* in the DRDM. To verify and to better study these critical behaviors of the multicellular systems, a time-delayed wound healing assays on a confluent cellular sheet were performed. In the experiments, the *dynamical scaling* of wound healing was observed. In order to further merge the DRDM and the macroscopic phenomena observed in experiments for proposing testable theories on multicellular aging, another simpler asymmetric reaction-diffusion equation (ARDE) for wound healing is proposed. This simpler model can reproduce all the macroscopic phenomena observed in experiments in terms of the healing curves and the density profile propagations. Paralleled criticality analysis for ARDE and DRDM helps identify the control parameter of aging as the asymmetry between the growth-to-arrest and

arrest-to-growth processes of the cells (*restriction asymmetry*). The successful bridge between the two models of different scales indicates that for multicellular aging (at least *in vitro*), the complexity of the system can be reduced or self-averaged by removing the details that are irrelevant to *restriction asymmetry* and by replacing details related to *restriction asymmetry* with more simpler representations.

Chapter 4

Nonequilibrium phase transitions in multicellular homeostasis

So far, the theoretic answer to the question whether and why normal homeostasis appears unstable and absorbed into aged and tumorigenic states in a long time is still absent. The *restriction asymmetry* as a control parameter identified by wound healing analysis indeed implies that the intrinsic dissipation of energy through cell cycle arrest may be one of the reasons. If the aging and tumorigenesis processes are potentially mapped to the absorbing phase transition in nonequilibrium physics, the fundamental scientific task here is first to draw the basic mathematical principles for such a living system to have the absorbing-phase transitions from healthy homeostasis to abnormal states. This needs a precise theory abstracted from a simple model that keep non-trivial macroscopic properties comparable to DRDM with no further redundant details. A plausible solution could be to seek for the receptor dynamics in the DRDM a Markovian representation, whose advantage lies in its mathematical analyzability. The following three subsections serve to be a tentative practice to accomplish this task.

4.1 A simple Markovian spin model

In the DRDM, the cells change their phenotypes according to the configuration of five kinds of receptors; in the correspondent Markovian representation of the phenotype dynamics, cells can change their phenotypes by some probability rates, which are time-independent. Despite that cells have many phenotypes in the DRDM (such as growing, polarizing, dying, and moving), the basic phenotypes critical to the system lifespan and the system stability of subpopulation structure are the three: cell proliferation, cell death,

and cell cycle arrest. If the single-cell kinetics are Markovian, we can define a transition matrix whose elements are homogeneous probability rates between each pair of the three phenotypes (Fig.4.1). Note that this Markovian spin model for DRDM is by nature a Potts model [115], which belongs to the family of stochastic cellular-automata.

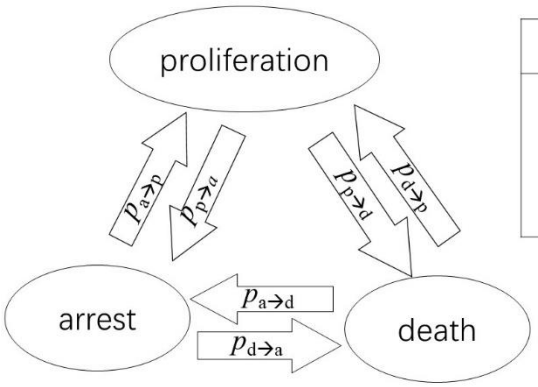

	p	a	d
p	X	$p_{p\to a}$	$p_{p\to d}$
a	$p_{a\to p}$	X	$p_{a\to d}$
d	$p_{d\to p}$	$p_{d\to a}$	X

p: cell proliferation
a: cell cycle arrest
d: cell death

Figure 4.1 A Markovian representation of spin dynamics at each node and its transition matrix. The fraction number $p_{i\to j}$ is the probability rate for a cell to transition from the state i to the state j ($i, j \in \{\mathrm{p,a,d}\}$) at each time step. The unknown fraction "X"s satisfy that sum of each row in the matrix equals 1.

Now since the transition matrix is defined as equivalent to the threshold dynamics of receptors in the DRDM, the transition rates $p_{i\to j}$ ($i, j \in \{\mathrm{p,a,d}\}$) must conform to the biological settings, especially of the intercellular interaction, in the DRDM. First, it should be noted that cells in this simple Markovian model is still assigned on the node in a network with predefined geometry and each node is mostly occupied by one cell, as is in the DRDM. Thus, the state "*d*" here broadly means that the node is null. As a universal principle for a living entity, the state "*a*", which means the cell cycle arrest, happens only to the living cell and not to the "null" state, so $p_{\mathrm{d}\to\mathrm{a}}$ must be zero. Next, let us specify the remaining transition rates one by one:

1) If the node state is "d":

The probability for an empty node to become occupied by a growing cell is only possible when the node is surrounded by some proliferative cells and the probability of the proliferation of the surrounding cells characterizes the transition rate $p_{\mathrm{d}\to\mathrm{p}}$. Hence,

$$p_{\mathrm{d}\to\mathrm{p}} \sim \left(\sum_{n\in N}\delta_{\eta_n,\mathrm{p}}\right)\Big/|N|,$$

where η_n is the state of the node n, $\delta_{i,j}$ is the Kronecker delta and N is the set of predefined neighboring nodes of this node with $|\cdot|$ denoting its size (the number of elements in this set). Clearly, $p_{\mathrm{d}\to\mathrm{p}}$ determines the rate of energy injection of the system.

2) If the node state is “p”:

In the DRDM, a growing cell secretes much extra-cellular matrix (ECM) whose concentration is one of the critical signals to stimulate the cell polarization that proceeds to accumulate arrest receptors, with the amount of inter-cellular adhesion the other critical signal. Both ECM and intercellular adhesion is large with sufficient local density of the cells. Accordingly, the probability of a node to change the state from cell proliferation to cell cycle arrest depends on the number of cells surrounding:

$$p_{\mathrm{p}\to\mathrm{a}} \sim \left(\sum_{n\in N} \left(\delta_{\eta_n,\mathrm{p}} + \delta_{\eta_n,\mathrm{a}} \right) \right) \Big/ |N| .$$

This density-dependent growth inhibition is also called contact inhibition of cells.

In the DRDM, the rate of cell death is highly dependent on the time the cell has spent in the unpolarized growing state in which the number of death receptors can accumulate. Unfortunately, it is very difficult to encode this time-dependent information into the time-independent transition probability $p_{\mathrm{p}\to\mathrm{d}}$ based merely on the last-time system configuration. Therefore, this $p_{\mathrm{p}\to\mathrm{d}}$ is set as constant to characterize the existing time of a single proliferative cell.

3) If the node state is “a”:

For a cell with ceased cell cycle, the condition for it to restart the cycle is the loss of growth inhibition, i.e., the decrease in ECM and intercellular adhesion in the DRDM. This is only possible when the empty space appears around this node. Therefore, the transition rate $p_{\mathrm{a}\to\mathrm{p}}$ is dependent on the number of empty nodes surrounding. Meanwhile, remember that in DRDM, another prerequisite for cell regrowth is its growth receptor amount exceeding the growth threshold g, which implies that the cell spent should not be deeply arrested. In the Markovian representation, this should be related to the fact that whether the node is still surrounded by sufficient proliferative cells: if the neighboring cells are proliferative, the chance by which this node is temporarily arrested by these proliferative cells is high; otherwise, the cell cycle of the cell at this node may have stayed in the quiescence for too long a time to be revocable. Combining the two rules, the probability for a cell to transition from cell cycle arrest to cell proliferation is:

$$p_{\mathrm{a}\to\mathrm{p}} \sim \left(\sum_{n\in N} \delta_{\eta_n,\mathrm{d}} \right) \bullet \left(\sum_{n\in N} \delta_{\eta_n,\mathrm{p}} \right) \Big/ |N|^2 ,$$

where the left bracket stands for the loss of contact inhibition and the right bracket for a temporary cell-cycle arrest. As one may observe from the equations above, the regrowth probability $p_{\mathrm{a}\to\mathrm{p}}$ is smaller than the growth probability $p_{\mathrm{d}\to\mathrm{p}}$.

Considering the death probability for an arrested cell, it also depends on the time the cell has spent on the non-polarized growing state during which the death receptors

are synthesized (the same as for $p_{\mathrm{p}\to\mathrm{d}}$). Nevertheless, since the polarized state of cell can lock the process of death receptors accumulation by transforming the active receptors (growth, adhesion, and ECM) to arrest receptors, the fact that whether the arrested cell is still polarized will influence the death probability of the cells: to simplify the situation, one can relate the loss of growth inhibition to the increase in cell death incidence. Combining the two aspects, the transition rate $p_{\mathrm{a}\to\mathrm{d}}$ becomes:

$$p_{\mathrm{a}\to\mathrm{d}} \sim \left(\sum_{n\in N}\delta_{\eta_n,\mathrm{d}}\right)\bullet p_{\mathrm{p}\to\mathrm{d}} \Big/ |N|.$$

By specifying these rules of intercellular interaction, one can update the transition matrix in Fig.4.1 as follows:

Table 4.1 Transition matrix for each node i in the Markovian representation of DRDM

η_i	proliferation	arrest	death
proliferation		$\dfrac{a\sum_{n\in N}\left(\delta_{\eta_n,\mathrm{p}}+\delta_{\eta_n,\mathrm{a}}\right)}{\lvert N\rvert}$	d
arrest	$\dfrac{r\left(\sum_{n\in N}\delta_{\eta_n,\mathrm{d}}\right)\bullet\left(\sum_{n\in N}\delta_{\eta_n,\mathrm{p}}\right)}{\lvert N\rvert^2}$		$\dfrac{d\sum_{n\in N}\delta_{\eta_n,\mathrm{d}}}{\lvert N\rvert}$
death	$\dfrac{g\sum_{n\in N}\delta_{\eta_n,\mathrm{p}}}{\lvert N\rvert}$	0	

Note: The blank elements for self-transition rate $p_{i\to i}$ satisfy that the sum of each row is unity.

In Table 4.1, four homogeneous parameters are introduced: the growth rate g, the growth inhibition strength a, the death probability d, and the regrowth power r, all ranging from 0 to 1. Without the loss of the generality, the growth rate can be set as 1 and the remaining three parameters are the irreducible control parameters to determine the system dynamics. So far as is shown in the next subsection, the three parameters are sufficient to reproduce the system dynamics which are similarly seen in the DRDM.

4.2 Simulation result

The simulation space S is, as in the DRDM, a 2D regular lattice with periodic boundary conditions. The neighbors of each node are predefined as the four Von

Neumann neighbors (other definitions of the neighbor set will make a trivial difference).

Fig.4.2 shows the snapshots of the system dynamics with different parameter settings. The lattice size is 100×100 and the initial condition is $\eta(50,50)$= p and η (others)= d, i.e., seeding one proliferative cell at the center of the lattice.

By changing the control parameters, one can still observe several growth patterns such as degenerate, normal to degenerate, normal to tumorigenesis, tumorigenesis. As is in the DRDM, the normal state can be quasi-stable with extremely large relaxation time to reach the final degenerate state [Fig.4.2 (A)]. The red dots represent proliferative cells and grey ones represent arrested cells. Fig.4.2 also shows for each growth pattern the time evolution of the vitality index $v = 0.1P_a + P_p$ (which is defined similarly as in the

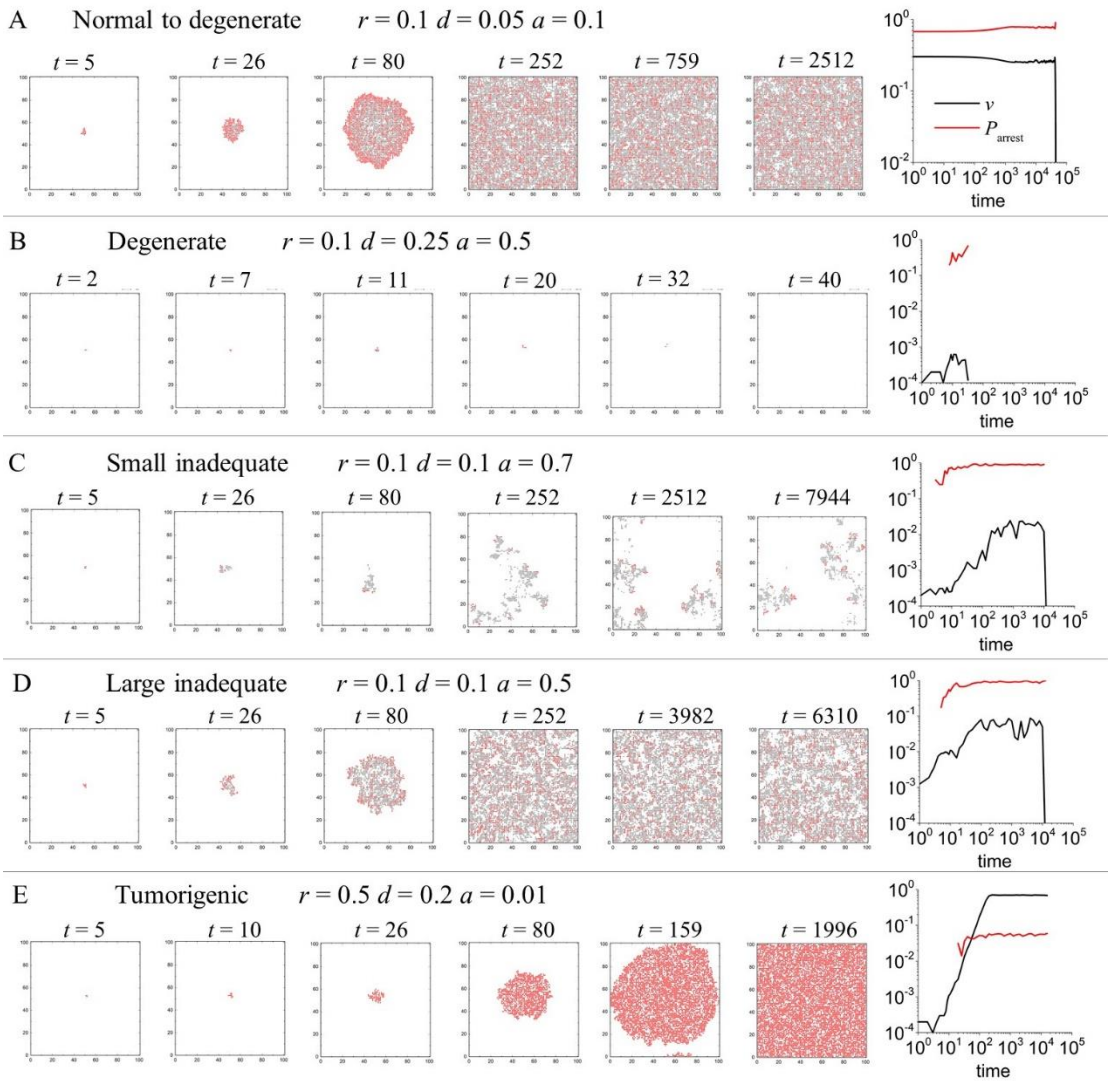

Figure 4.2 Simulation output for five kinds of parameter settings for linear system size L = 100. Red dots represent proliferative cells and grey ones arrested cells. The time plots on the rightmost column show the evolution of the vitality index v (black line) and the portion of arrested cells (red line).

Eq. 2.3), where P_η is the percentage of the cells in the state η. One can compare Fig.4.2 to Fig.2.2 and find two models have a very similar diversity of the growth patterns but the Markovian system can hardly keep stabilized morphology as is shown in the DRDM because the events like cell death and cell cycle arrest occur with spatial homogeneity. This small discrepancy between threshold dynamics and Markovian dynamics of cell phenotype transition reveals the fact that the time-independent probability "rate" of cell death loses some information which is accumulating through time in the DRDM although this might be trivial compared to other parts of the dynamics in the model.

4.3 Mean-field analysis

The Markovian spin model here is conceived for investigating the reason why the system has quasi-stable normal homeostasis and why the system has the intention of being absorbed into degeneration and tumorigenesis. One can approach this by mathematical analysis on the dynamics of system variables. The system has two degrees of freedom: the number of arrested cells and the number of proliferative cells; thus, the populations of these two types of cells are the two dynamic variables to be tackled. Let me denote these two fractions of populations at time t as $P_{\mathrm{a}}(t)$ and $\mathrm{P_p}(t)$. The "master equation" of this system is characterized as follows:

$$\begin{cases} P_{\mathrm{p}}(t+1)-P_{\mathrm{p}}(t)=\dfrac{1}{|S|}\displaystyle\sum_{n\in S}\left(p^n_{\mathrm{d}\to\mathrm{p}}(t)\delta_{\eta_n(t),\mathrm{d}}+p^n_{\mathrm{a}\to\mathrm{p}}(t)\delta_{\eta_n(t),\mathrm{a}}-\left(p^n_{\mathrm{p}\to\mathrm{a}}(t)+p^n_{\mathrm{p}\to\mathrm{d}}(t)\right)\delta_{\eta_n(t),\mathrm{p}}\right) \\ P_{\mathrm{a}}(t+1)-P_{\mathrm{a}}(t)=\dfrac{1}{|S|}\displaystyle\sum_{n\in S}\left(p^n_{\mathrm{p}\to\mathrm{a}}(t)\delta_{\eta_n(t),\mathrm{p}}-\left(p^n_{\mathrm{a}\to\mathrm{d}}(t)+p^n_{\mathrm{a}\to\mathrm{p}}(t)\right)\delta_{\eta_n(t),\mathrm{a}}\right) \end{cases} \quad \text{(Eqs.4.1)}$$

with the initial condition $P_{\mathrm{p}}(0)=1/|S|$ and $P_{\mathrm{a}}(0)=0$. $|S|$ is the system size $L\times L$. In order to solve this dynamic equation, one can use a mean-field approximation. The transition rate $p^n{}_{i\to j}(t)$ ($i, j\in\{\mathrm{p,a,d}\}$) at each node n, which is fluctuating across the whole space, can be replaced by an effective global transition rate $p^e{}_{i\to j}(t)$, which can be shared by all the nodes at the time t. This mean-field assumption is only valid when the cell number is large enough, i.e., the node state configuration in a local subsystem (which is the Von Neumann neighboring area in the simulation) in can be statistically approached by the configuration in the global system. Thence, one can obtain the effective transition rates by substituting the global node set S for the local node set N in the definitions of all transition rates (see Table 4.1) and Eqs.4.1 with the limit of infinitesimal time interval becomes:

$$\begin{cases} \dot{P}_{\mathrm{p}}(t) = \left(1 + rP_{\mathrm{a}}(t)\right)\left(1 - P_{\mathrm{a}}(t) - P_{\mathrm{p}}(t)\right)P_{\mathrm{p}}(t) - \left(a\left(P_{\mathrm{p}}(t) + P_{\mathrm{a}}(t)\right) + d\right)P_{\mathrm{p}}(t) \\ \dot{P}_{\mathrm{a}}(t) = \left(a\left(P_{\mathrm{p}}(t) + P_{\mathrm{a}}(t)\right)\right)P_{\mathrm{p}}(t) - \left(d + rP_{\mathrm{p}}(t)\right)\left(1 - P_{\mathrm{a}}(t) - P_{\mathrm{p}}(t)\right)P_{\mathrm{a}}(t) \end{cases} . \quad \text{(Eqs.4.2)}$$

Now, Eqs.4.2 is a set of nonlinear differential equations with only two time-dependent variables. The fixed points of Eqs.4.2 can be solved by setting

$$\dot{P}_{\mathrm{p}} = 0, \dot{P}_{\mathrm{a}} = 0$$

under different circumstances:

(i) When r, a, d = 0, the system has the fixed points lying at two lines: $P_{\mathrm{a}} + P_{\mathrm{p}}$=1 and P_{p} =0, the former one is stable and the latter unstable. Considering the initial condition (1/|S|,0), the two lines of fixed points predicts that P_{p}, i.e., the percentage of proliferative cells, keeps diverging until it reaches 1 and the system is in the all-proliferative configuration. This is easily understood that the cell-cycle arrest and the cell death are mutated hence the proliferative cells multiply to dominate the whole space.

(ii) When r, d = 0 and $a \neq 0$, Eqs.4.2 have fixed points located only on the line P_{p} = 0. This is also very evident that the percentage of arrest cells is monotonically increasing, i.e., $\dot{P}_{\mathrm{a}} > 0$, until the proliferative cells die out and the system reach an all-arrested configuration. The P_{p} = 0 serves as an absorbing wall of the system dynamics.

(iii) When $rd \neq 0$, which is the general non-trivial case encountered in the simulations, Eqs.4.2 has three fixed points ($P_{\mathrm{p}*}$, $P_{\mathrm{a}*}$) within $P_{\mathrm{p}*}$, $P_{\mathrm{a}*} \in [0,1]$:
($P_{\mathrm{p}*1}$, $P_{\mathrm{a}*1}$) = (0,0), ($P_{\mathrm{p}*2}$, $P_{\mathrm{a}*2}$) =(0,1), for all r, d, a

and ($P_{\mathrm{p}*3}$, $P_{\mathrm{a}*3}$) = $((1-d)(1-a/rd) + \varepsilon_{\mathrm{p}}, a(1-d)/rd - \varepsilon_{\mathrm{a}})$
where ε_{p} and ε_{a} are two correction terms.

For ($P_{\mathrm{p}*3}$, $P_{\mathrm{a}*3}$) to fall in the valid interval, one needs $rd \gtrapprox a$. If $rd \ll$ a, this fixed point does not exist.

Next, one can derive the Jacobian of Eqs.4.2 to analyze the stability of these fixed points. For simplicity of notation, the variable of time t can be omitted and let me set $x = P_{\mathrm{p}}$, $y = P_{\mathrm{a}}$, and then the Jacobian of the system becomes:

$$J = \begin{bmatrix} -ry^2 - 2rxy + (r-1-a)y - 2(a+1)x + 1 - d & -rx^2 - 2rxy - (r+a+1)x \\ y^2 + 2rxy + (d+a-r)x + 2ax + (d-r)y & rx^2 + (a-r+d)x + 2dy - d \end{bmatrix}_{x^*, y^*} .$$

For the fixed point (0,0), the determinant of J is $\Delta = -(1-d)d < 0$; thus, the fixed point (0,0) is a saddle point with the stable manifold at x = 0.

For the fixed point (0,1), the determinant of J is $\Delta = -(a+d)d < 0$, which

indicates that the fixed point (0,1) is also a saddle point but this time $x = 0$ is the unstable manifold.

For the fixed point $((1-d)(1-a/rd)+\varepsilon_p,\ \ a(1-d)/rd-\varepsilon_a)$, the determinant and the trace of J and the trace τ satisfies $\tau^2 - 4\Delta < 0$ (demonstration not shown here); therefore, this fixed point is a spiral.

A summary of the stability analysis is shown in the phase portrait of the system [Fig.4.3 (left)], which predicts the time logs in the simulation [Fig.4.3 (right)]. The red and blue dashed spirals in Fig.4.3 (left) only exists for $rd \gtrapprox a$; particularly, the red spiral exists when $rd \approx a$ [see the panel 2 in Fig.4.3; also refer to the Fig.4.2(A)] and the blue one exists when $rd \gg a$ [the panel 3 in Fig.4.3; also refer to Fig.4.2 (E)]. If $rd \ll a$, only degenerative processes absorbed into (0,0) is possible (the panel 1 in Fig.4.3).

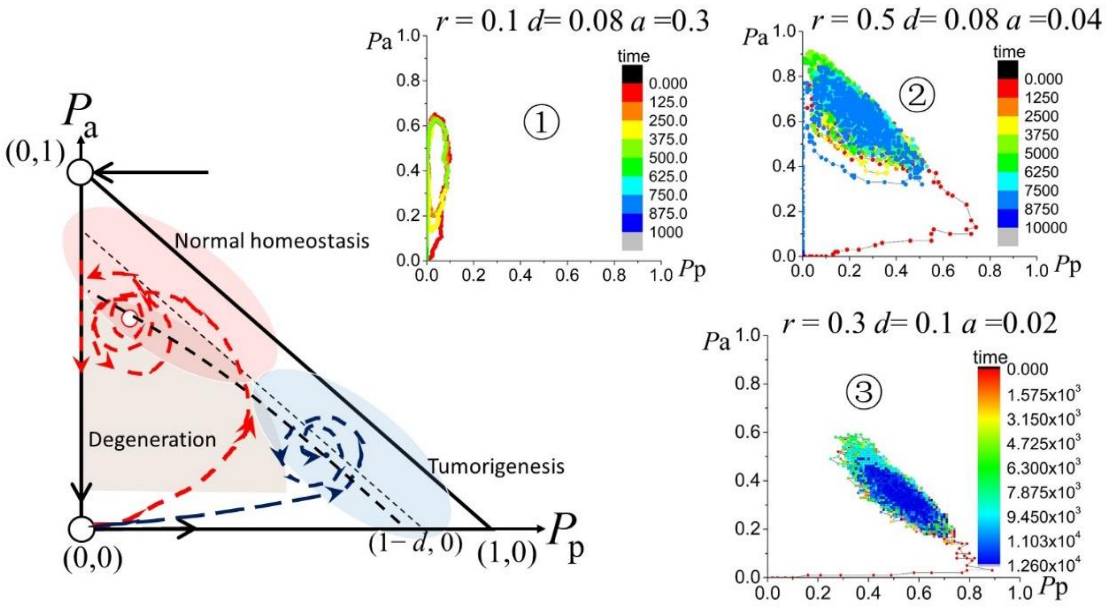

Figure 4.3 System trajectories in the space of P_p, P_a. Left: phase portrait from mean-field approximation. Right 1-3: the time log from the simulation of the spin flipping dynamics (for system linear size $L = 10$).

4.4 Finite size effect and memory effect

Knowing that the system trajectory may become a spiral around the fixed point, one needs further to look into the details of the Jacobian to estimate how "stable" the spiral might be in a turbulent environmental setting. In fact, the trace of the Jacobian can be positive if the fixed point is extremely large in P_a and extremely small in P_p

while the fixed point with small P_a and large P_p is always negative, which means that the spiral of the tumorigenic system (the blue dashed line in Fig.4.3) is rather stable but the spiral of the normal system (the red dashed line in Fig.4.3) has the risk to derail from the spiral and unfortunately absorbed into the stable manifold of the extinction point (0,0) (i.e., becomes extinctive degenerate).

From a theoretical point of view, most system trajectories of normal homeostasis could be a stable spiral, as is the trajectories of the tumorigenesis. The only difference between the two spirals is that the spiral of normal homeostasis is closer to the stable manifold of the extinction point (0,0) and is less stable in theory, thus having rare chances to be absorbed into the wall of non-proliferation (i.e., P_p=0). However, the mean field approximation does not consider the non-trivial heterogeneity among cells which may bring substantial spatiotemporal fluctuations to local variables, especially in smaller systems.

The chance for the normal homeostasis to be absorbed to the degeneration (or the characteristic timescale for the system dynamics to be active) decreases with the system

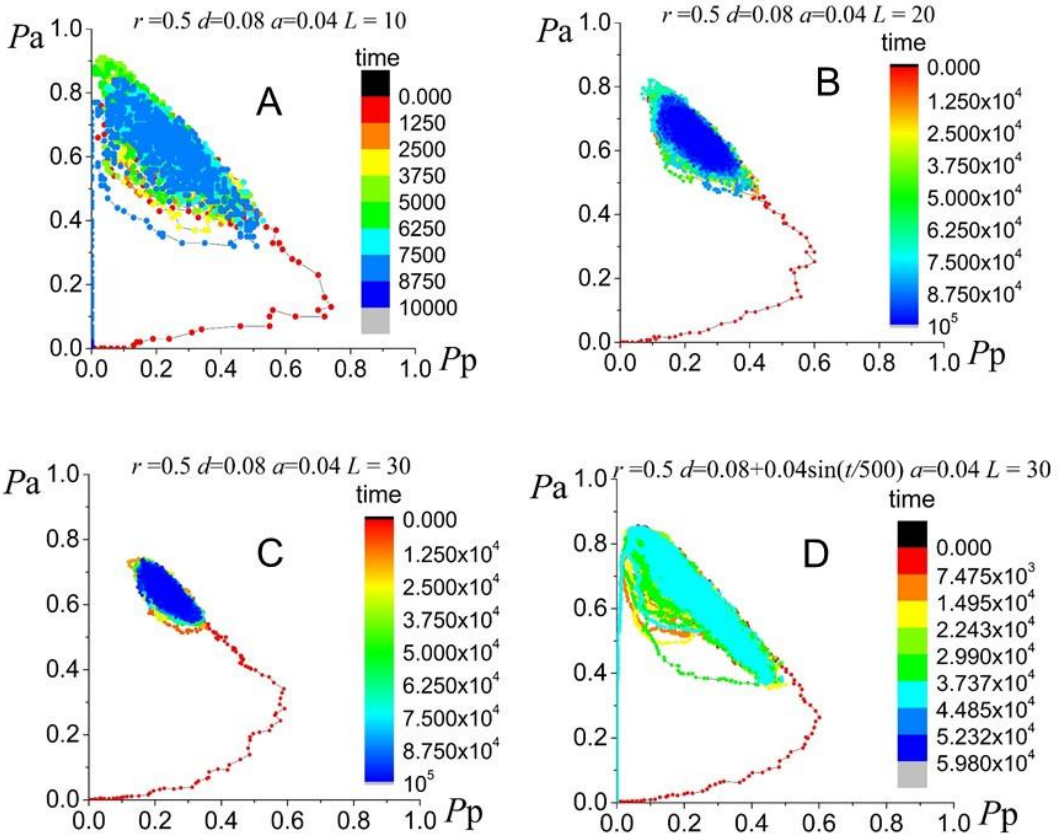

Figure 4.4 Absorbing phase transition under finite size and memory effect. Panels (A-C) show the system trajectories under the same parameter setting with increasing system linear size L= 10, 20, 30. Panel (D) shows the absorbing phase transition of normal homeostasis appears in large system with a periodically oscillation in death rate d.

size [Fig.4.4 (A)-(C)] because the spiral becomes more centered and appears rather stable. Being near the absorption wall, the system will also become sensitive to time-dependent fluctuations such as turbulent environments and synchronization of cell phenotype due to memory effect (e.g. brought by threshold dynamics). Fig.4.4 (D) shows that if the constant death rate d is imposed by a periodically oscillatory signal with zero average, the large system dynamics of normal homeostasis again look like that in a small system [Fig.4.4 (A)]. This also implies that the normal homeostasis in DRDM which might have stable spiral trajectories, in theory, is less stable than those in the Markovian spin model because the DRDM adopts a threshold formalism that brings about large time-dependent fluctuations (refer to the periodic growing patterns in Fig.2.2).

4.5 Summary of Chapter 4

The quasi-stability of normal homeostasis and the existence of three absorbing states with the relation to the value of control parameters has been fully understood in this simple Markovian spin model based on the DRDM. Some simple rules of the coordination of cell growth, cell death, and cell cycle arrest can produce very complex growth patterns and life excursions of tissues.

One can elaborate a theoretical picture for the Markovian spin system (and its complex equivalence, the DRDM), in which three possible fates appear according to the parameter setting regrowth ability r, death rate d and arrest tendency a:

(i) Degenerate, which happens when $rd \ll a$ and the dynamics terminates very fast;

(ii) Normal, which happens when $rd \approx a$ and whose system trajectories is a quasi-stable spiral around a fixed point close to wall of non-proliferative absorption wall (i.e., $P_p = 0$ in Fig.4.2) until it hits the wall and becomes degenerate after a very long time of relaxation;

(iii) Tumorigenic, which happens when $rd \gg a$, and whose system trajectories are spiraling towards the fixed point with a period of time.

One may notice that the transition between degeneration and normal homeostasis is abrupt since the existence or disappearance of the fixed point for the spiral is a qualitative change for the system; by contrast, the boundary between normal homeostasis and tumorigenesis is rather obscure and the transition is continuous. This can also be similarly observed in the phase diagram of the DRDM (refer to Fig.2.6).

Finally, let us discuss why rd/a turns to be the ultimate essential interdependence structure controlling the homeostasis: large r and d and small a help the system to stay in detailed balance (symmetry of ergodicity) [105-106] or away from the breaking of ergodicity in a turbulent environment. In this sense, rd/a resembles δ in their controlling

"detailed balance of cell phenotypes" and $rd/a<1$ corresponds to $\delta<1$.

In a more vivid picture, if the three phenotypes can "flow" from site to site, the regrowth and death ability in compare with cell cycle inhibition will decide how watery the "phenotype fluid" is. Tumorigenic system in DRDM and its Markovian version is a perfect detailed balanced system with huge fluidity (old cells die quickly and reduce the contact inhibition for the healthy and strong cells to maintain system activeness), thus very robust against external perturbations; by contrast, normal homeostasis is weakly broken in the detail balance and may undergo glass transition until it gets degenerate; degeneration is a totally jammed condition of the "phenotype fluid" and the system becomes a "solid" with no other adaptive ability to any external turbulence. Refer to Fig.4.5 for a schematic illustration.

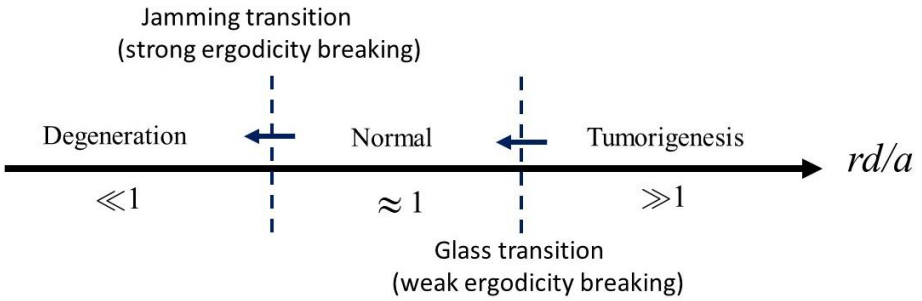

Figure 4.5 Non-equilibrium phase transitions in Markovian spin system and the DRDM for multicellular homeostasis.

Chapter 5

A generalized methodology for CASs

In the foregoing chapters, I have shown how multicellular system can be studied with models at several mesoscopic levels to deal with reducible and self-averaging complexities. As a result, these models embracing the same essential interdependence structure of dynamics can reproduce consistent macroscopic phenomena and propose testable theories for multicellular homeostasis and multicellular aging. Moreover, the coupling effect of non-adaptive relaxation and adaptation is also investigated. In this chapter, I will discuss the generalization of this mesoscopic modeling methodology to a broader class of complex adaptive systems (CASs) and its application prospect on pragmatic system engineering.

5.1 Complexity problem in CASs

Non-adaptive relaxation and adaptation are two fundamental equilibrium dynamics in CASs [79]. “Equilibrium dynamics” here broadly means that the process of dynamic optimization of some system functions, e.g. the minimization of energy for structural relaxation, the maximization of entropy for thermodynamic relaxation, or the maximization of fitness for biological evolution. The relaxation processes, prevalent in physical systems, depends on local individual interactions that facilitate to reach a stable microscopic configuration under some mechanical and behavioral principles. By contrast, the adaptive processes, a bequeathed wisdom by C. Darwin, are deemed as the essence of life [117] and depends on some autonomous variations of individual properties (i.e., the mutation in the biological context) that facilitate the interspecies competitions under the law of “the survival of the fittest”. Despite that adaptive processes have long been treated as the analogs of relaxations in evolutionary dynamics with concepts and

formulas borrowed from statistical physics [118-119], relaxation and adaptation are governed by laws on disparate levels yet extensively intertwined in CASs.

In a long history, relaxation and adaptation have been studied within distinctive academic disciplines for their incomparable characteristic spatiotemporal scales. The one process with shorter characteristic scales predominantly controls the system evolution with the other one yielding epiphenomena. For instance, in all many-body physical systems embracing fixed mechanical laws with non-mutable particles, the characteristic timescale of adaptation is infinitely long so that the system only equilibrates through relaxation, reaching a stable particle configuration; by contrast, for the systems with large-scale living entities such as cells, people, or even groups of people, the timescale of relaxation can be rather long, hence the system tends to equilibrate through adaptation to reach a configuration wherein no individual can gain more fitness, e.g., the Nash equilibrium in game theory[125].

Relaxation processes not only constitute the dynamics in condensed matters and material sciences[120], but also extends to pattern formations in diffusion-reaction systems[28], the self-organization of homeostasis in biological organisms [121], the Pareto optimization of resource allocation in neo-classical economics [122], the emergence of behavioral patterns in macroscopic socioeconomics[123] amongst others; whereas, the studies on adaptation tackles mainly ecological and biological issues[124], and has been extended to cancer biology [71-73], game theory[125-125], sociobiology[127], psychology[128], evolutionary economics[129], and so forth.

Complex adaptive systems (CASs) [130] are the systems where relaxation and adaptation feature comparable characteristic scales and intertwine to generate huge complexity (as one has seen in Ch.2.3) [131]. Variations of individual properties during adaptation changes the interaction laws and reciprocally, the ongoing relaxation of the individual configuration will interfere with the way of variation and selection.

A conventional approach to dealing with this complexity in the framework of the Darwinian evolutionary theory is to encapsulate the impact of both processes into the fitness function as two types of noises, which, nevertheless, is very difficult to formulate [118,132]. Particularly, Game theory [125] addresses this problem via a paradigm in which the fitness of an individual genotype dynamically varies as a function of the composition of other individual genotypes by assuming random phenotypic interactions. Note that a genotype is a replicable individual intrinsic trait that contributes to the phenotype, whereas a phenotype is a transient behavioral state resulted from not only the genotypes but the local interactions and the environment as well. This simplification of phenotypic interactions facilitates mathematical formulation at the sacrifice of non-trivial structures in the interactive dynamics that define the features of specific CASs.

Take multicellular system, which is the research object in this thesis, for example. On one hand, many biologists assert that Darwinian adaptation governs the complex diseases like cancer, in which cells with cancerous genes are advantaged and selected

to survive; on the other hand, the multicellular system is constantly subject to the relaxation mechanism stemming from the biochemical negative feedbacks among different bio-entities to stabilize the multicellular culture for the maintenance of overall biological functions, i.e., homeostasis. In the studies of multicellular homeostasis, cells are presumed to be homogeneously programmed automaton without mutations because mutation rate is considered as too small to affect homeostasis. By contrast, in studies focusing on the genetic mutations and evolutionary origin of cancer, those non-mutational factors (including the multicellular relaxation) can only be simplified as some "source of noise" added to the fitness function for the sake of theory formulation. How the two processes exactly couple in complex diseases like cancer is still obscure and the study oriented to practical uses is lacking.

As opposed to many existing paradigms which studies genotype dynamics in detail, the main methodology present in this thesis for addressing the complexity in multicellular systems is to disentangle the complexity by first focusing the non-mutational phenotypic dynamics of local interactions then tailoring the phenotypic dynamics by the impact of adaptation. In other words, the mesoscopic approach treats the CAS as a physical system composed of many mutable particles for abstracting the specifiable non-trivial interdependence structures (e.g. rd/a in Ch.4) and then utilizes the non-adaptive phase diagrams for analyzing adaptation.

5.2 Generalized framework

As is emphasized in 5.1, the methodology advocates a mesoscopic deconstruction of the system details into non-adaptive phenotypic interactions and the genotypic variation strategies for adaptation. The non-adaptive parts have been fully discussed in the thesis for multicellular systems in terms of model simplification, model comparison, and theory establishment and are summarized in Ch.5.2.1 as a systematical review. The coupling of non-adaptive relaxations and adaptation has been studied by the mutational DRDM and a general picture of how adaptation tailors the relaxation processes has also been established and summarized in Ch.5.2.2.

5.2.1 Models for non-adaptive relaxations

Fig.5.1 is an overview of the non-adaptive models discussed in this thesis on the plane of model analyzability (horizontal axis) and model scale (vertical axis). A model with full empirical details can reproduce richest phenomena; yet, the larger the scope of reproducible phenomena is, the lower mechanistic power the models has. By contrast, a model on a larger scale with fewer details can reproduce a more specific scope

phenomenon whose relation to the model assumption is clearer and more analyzable; yet phenomenon produced by simpler models may not lie within the scope of the phenomena reproduced by a complicated model or in reality. This is a gap between the pragmatic and theoretic approach in systems biology (refer back to Fig.1.1).

Fortunately, the non-adaptive details contributing to relaxation might have many isomorphic representations on different levels of scale because they compromise the huge amount of self-averaging complexity. As shown in Fig.5.1, the model with more microscopic details (IBcell) can be simplified to the DRDM, which loses the precise morphological information but keeps reproducing diverse homeostasis; a simpler Markovian spin model can further be simplified from the DRDM to analytically explain why diverse homeostasis occurs but totally loses the morphological patterns and memory effect in the DRDM. Meanwhile, a macroscopic model ARDE with only one parameter is specifically proposed to tackle with multicellular aging and is found to be isomorphic to the DRDM with normal-to-degenerate parameter settings through criticality analysis. Once the simple model is found to be isomorphic to a complicated model and they both reproduce consistent phenomena, the model assumptions used in the simple model should find its equivalent complex representation in the complicated model, which is the essential interdependence structure responsible for the self-averaging complexity. In most cases, the isomorphism between models on different scales cannot easily be confirmed, unlike the strictly defined universality classes in statistical physics for the models on similar levels. Therefore, it is always valuable to have models at many different scales and to compare them for cultivating an intuition

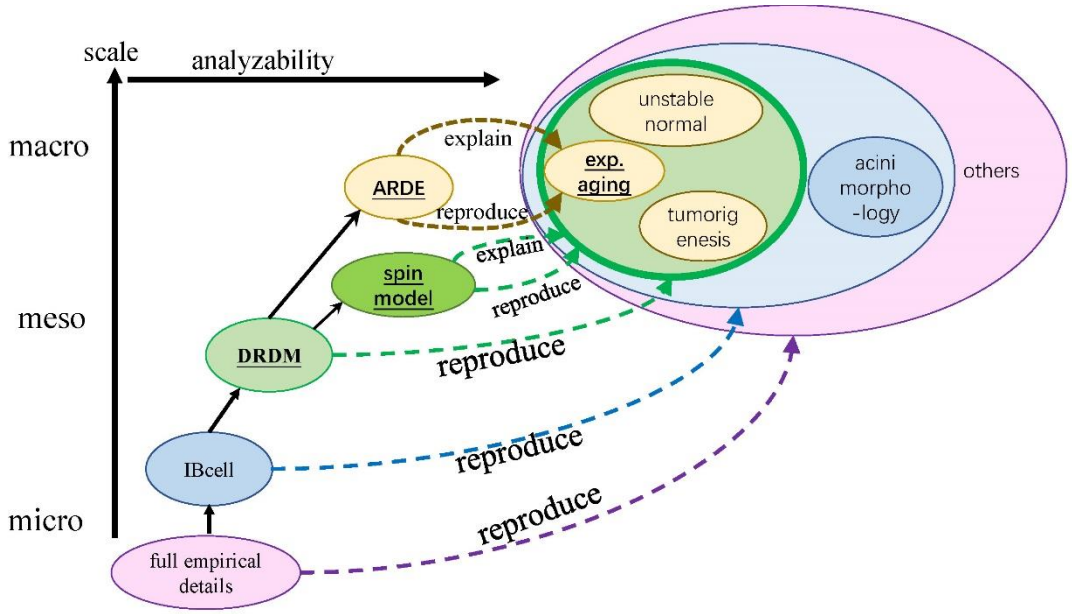

Figure 5.1 Non-adaptive models on different scales.

on the model selection. With suitable models on the mesoscopic scales, the gap between the pragmatic and theoretic models can be merged for generating testable theories applicable to pragmatic problems.

One should also note that the roads from complex models to simple models are diverse and phenomenon-oriented. A simple model usually can only address very few well-defined phenomena (e.g., the current ARDE can only explain the complete healing with late onset of the aging regime, while the DRDM can further reproduce incomplete healing because of more degrees of freedom in the parameter space). Therefore, defining a phenomenon of interest precisely will help one find the nearest mesoscopic path from the complex details to some simple theories.

5.2.2 Adaptation coupled with relaxation

Then, what is the role of adaptation in CASs? Based on the results in Ch.2.3.5, one can have a simple formulation to help abstract the essence of complicated dynamics under both relaxation and adaptation as:

$$f(\boldsymbol{x})=f_{sys}(\boldsymbol{x}) + \mu\, f_{in}(\boldsymbol{x}) \qquad \text{(Eq.5.1)}$$

where $\boldsymbol{x}$ is a multi-dimensional control parameter for non-adaptive relaxation and meanwhile the "genotypes" to be selected. $f(\boldsymbol{x})$ is the Wright potential for selecting individual genotypes, $f_{sys}(\boldsymbol{x})$ is the order parameter of non-adaptive relaxation serving as the potential under "system selection", and $f_{in}(\boldsymbol{x})$ is the potential under non-interactive selection(e.g. natural selection). The coefficient μ weighs the scale difference between the two terms and can also be interpreted as an effective mutation rate $\mu = \mu_0\, G(f_{sys}(\boldsymbol{x}))$, in which μ_0 is the speed of variation of individual genotype without being the constraint by others and $G(f_{sys}(\boldsymbol{x}))$ is a factor that adds a nonlinear dependence of μ on $f_{sys}(\boldsymbol{x})$. In the case of tumorigenesis in the DRDM, $G(f_{sys}(\boldsymbol{x}))$ is a non-zero increasing function of $f_{sys}(\boldsymbol{x})$ because the mutation of cells only happens when the cell is dividing, and a system with a higher $f_{sys}(\boldsymbol{x})$ will have a higher frequency of cell division, thus a higher mutation frequency. For other CASs, the prerequisite of mutation could be different. For instance, in the free market systems, $G(f_{sys}(\boldsymbol{x}))$ can be a decreasing function of f_{sys} because the mutation of investment strategies of one company in the market may only happen when the current strategy becomes non-profitable (inducing low fitness). Therefore, the formulation of μ is context-specified.

Then, the system's trajectory on the topologically complicated fitness landscape $f(x)$ through variations involves five determinants:

i) $f_{sys}(\boldsymbol{x})$, which is also a phase function resulted from the non-adaptive relaxation

where all individuals have the same set of genotypes (control parameter),
ii) $f_{in}(\boldsymbol{x})$,
iii) strategies of variation, which define d$\boldsymbol{x}$/dt for each individual;

And if the variation strategies are rigid (like the hereditary mutations in the DRDM), the following two are critical:
iv) μ, controlling the time scale difference between relaxation and adaptation,
v) the initial condition of $\boldsymbol{x}$.

It should also be mentioned that although $f_{in}(\boldsymbol{x})$ and $f_{sys}(\boldsymbol{x})$ are two different representations of fitness, they can be positively correlated because $f_{sys}(\boldsymbol{x})$ by its definition is contributed by all the individuals' fitness under the effect of phenotypic interactions. For instance, v, indicating the percentage of proliferating cells in the system, is low at the left-top corner in Fig.8 while the single cell vitality is also close to zero. On the other hand, the system composed of individuals with a high $f_{in}(\boldsymbol{x})$ can have a low $f_{sys}(\boldsymbol{x})$ because the resources and space are limited (by whatever means), then the conflicts among those strong competitors may harm the interactive cooperation, diminishing the collective fitness of the system.

The rigidity of the variation strategies tends to foster huge complexity in CASs (e.g. the clonal expansions in the DRDM). In reality, especially for systems on larger scales like economic systems or social organizations, variations of individual can hardly be isotropic since living entities are prone to inherit many settings from their ancestors or to imitate the successful individuals in a constraint-ridden setting, hence the evolutions in real CASs may exhibit huge complexities as in the computational tumorigenesis. Using the Eq.5.2, one can, to some extent, foresee the evolutionary paths under rigid mutations and predict the system's evolution. The lesson from the *stochastic* mutation results in the DRDM tells us that given a high plasticity of variation strategies, it is possible to predict the final state of the evolution through the f_{sys} (i.e., phase diagram for non-adaptive relaxations) alone because the system can efficiently find the fittest phase and tend to self-organized at the critical boundary between different phases if the individual fitness and system fitness have opposite trends.

5.3 Application: multicellular aging as an example

The central theme of this thesis is to help find testable theories for complex adaptive systems that help produce applications in system engineering. The greatest contribution of the paralleled modeling of ARDE and DRDM is its proposal of the theory that delayed response to regrowth signals of cells controls multicellular aging. This can be tested in real experiments and may open several new research directions on

tissue aging and regeneration modulation.

From the model analyses, two key factors in bio-aging were identified as 1) *growth inhibition* (resulting from cell-cell contact, cell-ECM interactions among others), which is the prerequisite, and 2) *restriction asymmetry*, the controller for the "wake-up" dynamics from the deep *growth inhibition*. For better regeneration, reducing the inhibition of cell growth is risky because growth inhibition is naturally programmed for tumor suppression. Nevertheless, reducing the asymmetry of cell-cycle regulation can enhance regeneration without risking tumorigenesis assuming natural growth inhibition is undisturbed. Therefore, administrating *restriction asymmetry* in the clutter of biological details is crucial. *Restriction asymmetry* in tissue may result from irreversibility of the activation route of signaling pathways [135-136] or can emerge from the monotonic shift of cell subpopulation structure [143]. Practical application to the regeneration of a specific tissue such as the liver tissue requires a full understanding of *restriction asymmetry* in a computational model exclusive to the hepatocytes in a multicellular context before key factors can be tuned in relevant experiments. However, we should always be aware that the delayed wake-up of cell activity may only be one possible ingredient attributed to tissue aging. In some circumstances, other factors such as the deterioration of the environment or the age-dependent pathogenesis can play more prominent roles. Within this scope, the effect of many medicines of interest can also be evaluated through its impact on the slowdown of healing.

Another potential application is the measurement of aging rate. Measurements of aging are difficult because of the complexity of the interactions among contributing factors [138-142]. Numerous studies have revealed the genetic determinants of longevity [134] and place a focus on life expectancy, i.e., the chronic distance to life termination (death; Fig. 5.2). However, the distance from the beginning of life (birth) and the speed of aging should also provide much information about the regenerative potential, which would facilitate health maintenance. The dynamical scaling exponent θ obtained by fitting the wait-dependent healing processes in our study can serve as a quantitative description of the regeneration-related aging rate of a tissue on its life

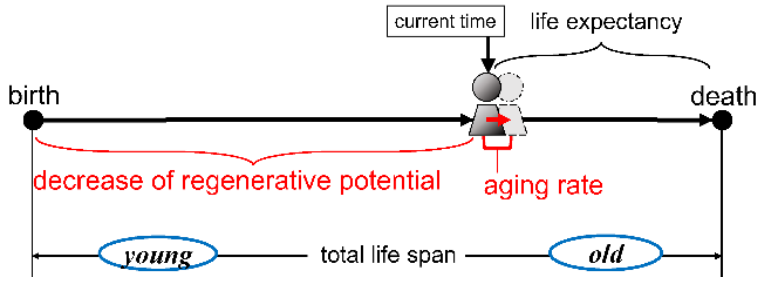

Figure 5.2 Measuring aging in a system's life excursion. Traditional biomarkers are focused on life expectancy (i.e., the chronological distance from the present to death); whereas, the dynamical scaling exponent θ quantitatively describes regeneration-related aging rate from young to old.

excursion from young to old age. Even though our protocol for measuring θ is inconvenient for *in vivo* experiments, θ can be easily measured *in vitro* for any cell lines of interest with any specific environment settings.

5.4 Final remarks

For a broader class of CASs, crucial interdependence structures providing non-reductionist theories for complex phenomena are also supposed to explain the correspondent complex phenomenon. Given any well-defined problem regarding a specific CAS, one should first confirm whether the timescales of relaxation and adaptation are comparable in the phenomenon of interest. If so, one can separate the adaptive processes from the non-adaptive ones and use mesoscopic models to reduce degrees of freedom and to figure out the interdependence structure responsible for the non-adaptive part. Then, according to the distinctive features of system adaptation, one should measure the individual/system fitness landscapes and analyze the system dynamics on the synthesized Wright potential as defined in Eq.5.2. More translations between the mesoscopic modeling and experiments as has been done for the ARDE and the TDWHA in Ch.3 should play the central role in advancing the CAS engineering in future.

Appendix A . *Adhere* function in DRDM

1. Cell-cell adhesion

Adhesion between two cells is dependent on the sizes of the cells and the distance between their cell membranes. There exists the largest distance (denoted as l) within which two receptors can be adhesive to each other. Since the single cell morphology is not presented, the receptors are regarded as uniformly distributed on the virtual cell membranes with a densityρ, hence, in 2D space, the length scale of the cells should be proportional to the total amount of cell receptor R. In other words, the calculation of the number of receptors and the calculation of geometric properties of the two cells are equivalent. Assume that when two neighboring cells grow to the physically maximal size with a total amount of receptor R_M for each, the cells have the largest radius R_M/ρ (hereafter ρ=1 for simplicity). The amount of the adhesion receptor attaching the two cells should at most reach 1/4 of the total free receptors for each cell because any single cell has at most four neighbors. The free receptors (denoted as R_f), i.e., the receptors that can be transformed into adhesion receptors merely through a cell-cell interaction, can be calculated as the sum of growth and adhesion receptors. In Fig. A1, when both cells have the maximal number of total receptors R_M, the central angle of adhesive range becomes $\pi/2$, thus 1/4 number of free receptors turning into the adhesion receptors for each cell.

Referring to Fig. A2, let any cell A and cell B be at a distance of $2R_M$ and with a radius r_1 and r_2 respectively. The maximal adhesive range of cell B is indicated by the circle in the dashed line with a radius $r_2 + l$. The adhesion range of cell A attached by cell B can be found at the intersection part of the circle A and the circle in the dashed line. The adhesion rate of cell A interacting with B (denoted as k^B), which is the portion of the adhesion receptors attached by cell B in the total free receptors, becomes $\varphi/2\pi$, where φ is the central angle corresponding to the adhesion range of cell A. Hence k^B can be calculated in the triangle ABC from laws of cosine as:

$$k^B = \frac{1}{\pi}\arccos\frac{4R_M^2 + r_1^2 - (r_2 + l)^2}{4R_M r_1}.$$

Considering that k^B =1/4 for $r_1 = r_2 = R_M$, the largest adhesion range is

$$l = \left(\sqrt{5-2\sqrt{2}} - 1\right)R_M \approx 0.47R_M$$

Thus the amount of the adhesive receptor obtained by the cell A is the summation over four neighbor nodes:

$$R_h^A(t+1) = \sum_{B \in neighbors} k^B R_f^A(t)$$

Note that the precision of this *Adhere* function is not crucial because, at this level of receptor dynamics, any description of the adhesion process is a coarse-grained one which qualitatively follows the principle that cell-cell adhesion is proportional to the cell size and inversely proportional to the distance in between the cell membranes.

2. Cell-ECM Adhesion

Adhesion between a cell and its ECM is dependent on its ECM concentration. Suppose that a unit mass of growth receptor can secrete ECM with the maximal amount of concentration e_{scr}. The density of ECM, denoted as d_E, is defined as follows:

$$d_E(t) = \frac{E(t)}{e_{scr} R_g(t)},$$

hence the amount of ECM receptor transformed from the growth receptor is

$$R_E(t+1) = \min\left(d_E(t) R_g(t), R_g(t)\right) = \min\left(\frac{E(t)}{e_{scr}}, R_g(t)\right)$$

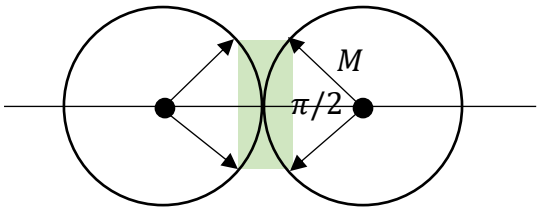

Figure A1 The adhesive receptors between two cells with the maximized cell sizes. The colored area shows the adhesive region with 1/4 amount of *free receptor number* transformed into the adhesion receptors.

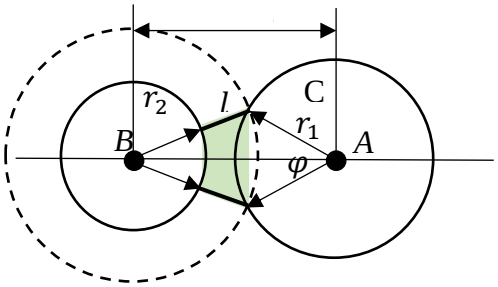

Figure A2 The adhesive receptors in any two cells shown in the colored area. The circle with a dashed line is the maximal range $r_2 + l$ within which the receptors on cell *A* can be attached by cell *B*.

Appendix B. Parameter settings of DRDM simulations

1. Basic simulations without mutation

Table B1 All the parameters for the simulation in Ch. 2.1 and Ch. 2.2.

Parameter	Definition	Baseline Value
L	System size	71×71
B	The number of basic growth receptors for a newly born cell	30
R_M	The number of total receptors required for mitosis	100
s_1	The secretion rate of ECM	10
s_2	The decrease rate of ECM	0.5
g	Growth threshold	0.3 R_M
p	Polarization threshold	0.09 R_M
h	Adhesion threshold	0.2 R_M
d	Death threshold	From 0 to 3.0R_M
e	ECM threshold	From 0 to1.0R_M
a	Arrest threshold	From 0 to1.0R_M
γ	Growth rate of growth receptor amount	0.1
a_{scr}	The transforming rate of arrest receptor	0.25
d_{scr}	The transforming rate of death receptor	0.001
e_{scr}	Maximal amount of ECM secreted by per mass of growth receptors	20

Note: Three thousand sessions of simulations are conducted by varying the death threshold, arrest threshold and ECM threshold at an interval of 0.1 R_M [results in Fig.2.6 (A-C)] ; For the results in Fig. 2.6(D-E), ECM threshold was varied at an interval of 0.05R_M. The unit of B, R_M is 10^{-10} mol per cell. The unit of s, c ,γ , a_{scr}, d_{scr} and e_{scr} is 1/step.

2. Simulations with mutation

Table B2 All the parameters for the simulation in Ch. 2.3.

Parameter	Definition	Baseline Value
L	System size	71×71
B	The number of basic growth receptors for a newly born cell	30
R_M	The number of total receptors required for mitosis	100
s_1	The secretion rate of ECM	0.01
s_2	The decrease rate of ECM	0.0005
g	Growth threshold	$0.3R_M$
p	Polarization threshold	$0.09\ R_M$
h	Adhesion threshold	$0.2\ R_M$
d	Death threshold	$3.0\ R_M$
e	ECM threshold	$0.2\ R_M$
a	Arrest threshold	$0.1\ R_M$
γ	Growth rate of growth receptor amount	0.1
a_{scr}	The transforming rate of arrest receptor	0.25
d_{scr}	The transforming rate of death receptor	0.001
e_{scr}	Maximal amount of ECM secreted by per mass of growth receptors	0.18

3. Simulations for wound healing phenomena

Table B3 Parameter settings used for time-delayed wound healing simulations in Ch.3.

Parameter	Definition	Baseline Value
S	Lattice size	71×10000
W	The size of the wound bed	16×10000
B	The number of basic growth receptors for a newly born cell	30
R_M	The minimum of total receptor numbers for mitosis	100
s	The secretion rate of ECM	10
c	The decrease rate of ECM	0.5
g	Growth threshold	From 0 to 2.0 R_M
p	Polarization threshold	0.09 R_M
h	Adhesion threshold	0.2 R_M
d	Death threshold	10^9 R_M
e	ECM threshold	From 0 to2.0 R_M
a	Arrest threshold	3 R_M
γ	Growth rate of growth receptor concentration	0.1
a_{scr}	The transforming rate of arrest receptor	0.25
d_{scr}	The transforming rate of death receptor	0.5
e_{scr}	Maximal amount of ECM secreted by per mass of growth receptors	20

Note: Death threshold d is set to a sufficiently large number to ensure that cell death was negligible during the wound healing simulation. ECM threshold e and growth threshold g were two variables scanned from 0 to 2 R_M with sampling interval 0.05 R_M. For the simulations in Fig.3.13 (B), g was fixed as 0.05 R_M and e as 0.8 R_M. The simulation space was a rectangular space with the 71 columns and the 10000 rows. The wound bed was a rectangular space with 16 columns and 10000 rows located at the center of the space.

Appendix C. Evolutionary Cont-Bouchaud Model

Financial price fluctuations exhibit many scaling laws in the statistics [145]. The simplest model for reproducing these scaling laws is the percolation model proposed by Cont and Bouchaud[144]. The model uses percolation theory to explain the spread of information based on the geometry of the connectivity of the investors. For reproducing the fat-tailed price return distribution, Cont-Bouchaud model (CB) needs fine-tuning of its control parameter, the connectivity, to a critical value. However, even with this fine-tuning of parameters, the tail of price return distribution is too fat to be representative of the real market.

A simple Darwinian mechanism coupled with a system feedback on individual participation rate can address these problems. Consider an investor in a lattice space with well-defined neighbors with an intention p ($0< p <1$) for participating in the market investment. The investor updates his intention p according to two rules:

(1) When he is not participating in the market: he will look at the neighbors and be influenced by their participation intention as:

$$p(t+1) = \text{avg}(p_{neighbors}(t)) + \sigma X ,$$

where $X \sim \mathcal{N}(0,1)$ is a Gaussian random variable and σ measures the strength of stochasticity.

(2) When he is in the market, his intention for continuing participation in the market is proportionally influenced by the price return of last time step. The price return serves as a macroscopic indicator of the system that "select" the gene, i.e., the intention p of investors, in the following way:

$$p(t+1) = p(t)[1+\beta r(t)],$$

where $r(t)$ is the log return of price(shortly termed as return) and $\beta \in [0,1]$ measures the sensitivity to the system behaviors.

The trading behavior of the investors and the price formation mechanisms are totally the same with the original C-B model. The only modification is to make the original control parameter p adaptive and the control parameters now are β and σ.

The influence from the neighbor, in fact, imposes a Darwinian selection for higher intention p because an investor with a lower p has more chances to look at other, while an investor with a higher p is more probably participating in the market thus not influenced by the neighbors. Therefore σ also serves as the mutation rate in Darwinian adaptation. With time iteration increasing, investors with low p gradually "die out" and the average participation rate of the investors is always increasing until the percolation effect happens when most of the investors are connected and share the same opinion on the market. Then the percolation of the investor's opinion results in such a huge positive or minus return that eventually will decrease the intention of participation if the return is minus by chance.

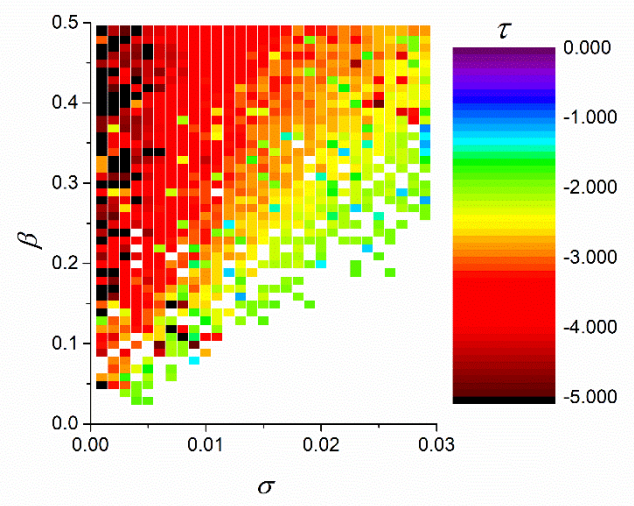

Figure C1 The tail exponent of price return distribution.

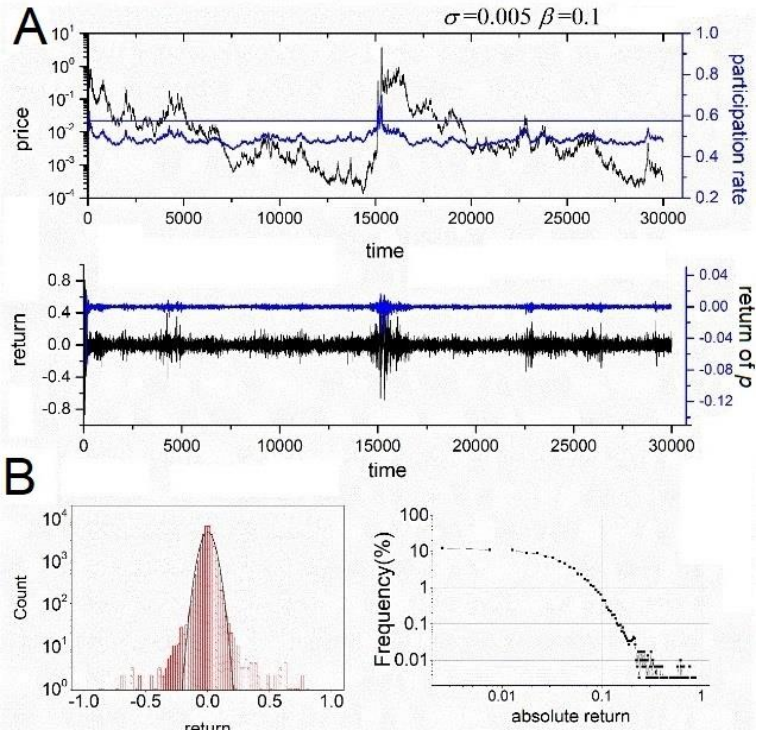

Figure C2 Statistics of evolutionary C-B model. (A) The exemplary time series of price, return, and participation rate averaged across all investors. (B) The distributions of returns, which exhibit the self-organized criticality in evolutionary CB model with σ=0.005,β=0.1.

The two rules serve as two forces that push the system self-organized to the critical value of the participation *p*, induce fat-tailed exponent -2.5~ -4 (Fig.C1) in all parameter spaces except for the sub-critical(black) and super-critical(white) region and produce the volatility clustering (Fig.C2).

The participation rate (which is the average *p*) of the investors evolve with time around the critical value of the percolation rate. As demonstrated in Ch.3.3, the variation of control parameters could be a driving force for the system approaching its critical state and showing self-organized criticaling when the interaction-based Wright potential (here is the price return) tends to propel the system in the opposite direction.

Appendix D. Material and methods for TDWHAs

1. Cell line and cell culture

HepG2.2.15 hepatocellular carcinoma cells were maintained in high-glucose Dulbecco's minimal essential medium (DMEM; Gibco, ThermoFisher Scientific), supplemented with 10% fetal bovine serum (US origin, Gibco, ThermoFisher Scientific) at 37°C and 5% CO_2. The medium was changed twice a day to ensure sufficient nutrients for the cells throughout the entire experiment.

2. Cell counting with a hemocytometer

Cell suspension (10 μL) was taken using a pipette and the pipette tip was placed near the edge of the chamber, allowing the cell suspension to enter the counting chamber by capillary action. The microscope was then focused on an area of the counting chamber and the cells were counted using a tally counter. The average cell count was taken from each of the sets of 16 corner squares and multiplied by 10000-fold. The final value was the number of viable cells per mL in the original cell suspension. The cell number in a total well can be calculated by the density times the total suspension volume (10mL) in the well.

3. Cell viability with 3-(4,5-dimethylthiazol-2-yl)-2,5-diphenyltetrazolium bromide (MTT) Assays

The medium was removed from each sample of the well and replaced with fresh culture medium. Then MTT (5 mg/ml) was added to each well to a final concentration of 10%. The cells were incubated at 37°C for 4 h. SDS-HCL solution (10% SDS in 0.01 M HCL) was then added to each well and mixed thoroughly using a pipette tip. Cells were then incubated at 37°C for another 4 h in a humidified chamber. Finally, the samples were mixed and absorbance was read at 550 nm (reference, 750 nm) with a spectrophotometer, indicating the metabolic viability of the total cells in the well.

4. Experiment parameter settings

Table D1. Parameter settings for two separate experiments with time-delayed wound healing assays.

Item	Description/Value
Pipette type	Gilson, 200μL/tips (200μL)
Average wound bed width	0.25 mm
Starvation time before waiting	24 h
Initial seeding cell density	5×10^5 cells/well (I), 2×10^6 cells/well(II)
Group number	4 (I), 5(II)

Appendix E. Pseudo codes for DRDM simulation

The DRDM is implemented on C++. Here I present the pseudo codes for non-mutational DRDM simulation (results in Fig.2.6). The annotation is in green.

1. Header

```
#ifndef header_h
#define header_h
#include "stdlib.h"
const int s =71; //system size
const double basic_r=30; //B
const double max_r=100; //R_M
const double scr = 10; //s_1
const double dc=0.05*scr; // s_2
const double e_scr=2*scr; //ecm secretion max
const double ad=0.01; //adhesion threshold
const double g= 0.03*max_r; //the growth threshold
const double gf = 0.1; //growth factor γ
const double a_scr=0.25;
const double d_scr=0.5;
/*time constant*/
const int max_t =1000; //simulation time
const int w_t = 20; //wounding time


class node //lattice node profile
{   public:
      node(int num):no(num),ar(false),age(0) //Initialization
      {    for(int i=0;i<5;i++)
             {   receptor[i]=0; }
           ecm=0;
           for(int i=0;i<8;i++)
           {      observable[i]=0;}
           left=NULL; right=NULL; top=NULL;bottom=NULL;
           a=0;d=0;e=0; }
/*cellular parameter*/
 bool ar; //cell cycle arrest index, 1 for arrested
 int no; //the node index
 double receptor[5]; //[growth][adhesion][ecm][arrest][death]
 double ecm; //extra cellular matrix amount E
 double observable[8]; //[num][age][G0][G1][S][death][permanent arrest][moving] for output
 int age;
double a; //arrest threshold
double d; //death threshold
double e; //ECM threshold
/*neighbours*/
 node *left; node *right; node *top; node *bottom;
```

```
    void cycle(); //cell cycle
    void wd(); //wound
    /*cellular function*/
    private:
    void growth(double gf); //accumulation of mass
    void proliferation(node *daughter);//give birth to a daughter
    void adhesion(); //adhere to other cell
    void rpoint(); //Restriction point
    bool death();
    void moveto(node *n);
    // void mutation();    };
/*Multicellular function*/
    int maxN(double * e, int l); // find the neighbor with least totalE
    double totalE(node * x); //calculate the total ECM concentration around
    int neighbour(node *x); //count the number of neighbors
    #endif
```

The definition and realization of these functions are following the Table 2.3, and I show the realization function of growth for an example. Others not shown here for saving space.

```
    void node::growth(double gf)
    {   if (!ar) //not arrested
        {       observable[3]=1; //a growing cell counted}
        else
        {   gf=0;   }
         if (receptor[0]+receptor[1]<max_r) //smaller than the mass of division
        {
            receptor[0]=((1+gf)*(receptor[0])); //growth receptor accumulation
            ecm = ecm+scr*receptor[0]-dc*(receptor[1]+receptor[2]+receptor[3]+receptor[4]);}}//ECM
    accumulation
```

2. Main body

```
#include "header.h"
#include "stdlib.h"
#include "fstream"
#include "math.h"
/*according to the simulation tasks, other headers may be included*/
using namespace std;

/*Establish the lattice*/
void create_network(node *first,int size)
{   2D-regular lattice: realization not shown.}
void destroy_network(node *first)
{   realization not shown. }
void seed(node *n,double aT,double eT,double dT)//aT,eT,dT arrest,ECM,death thresholds
{
        n->receptor[0] = basic_r;
        n->ecm = (double)scr*n->receptor[0];
```

```
            n->a = aT; n->d = dT; n->e=eT;
}
void process(node *n, int a)
{
        node *temp=n;
        for(int i=0;i<h;i++)
        {       for(int j=0;j<a;j++)
                {       for(int i=0;i<8;i++)
                        {       temp->observable[i]=0;}
                        if(temp->ecm!=0)//is there a cell already
                        {       temp->cycle();}
                        temp=temp->right;    }
                        temp=temp->bottom;
        }
}
void wound(node *n,int a,int b)//scratch an area of cells
{
        node *temp=n;
        for (int x = 0; x < (a - b) / 2; x++)
        {       temp = temp->right;   }
        for (int l = 0; l< b; l++)
        {       for (int r= 0; r< h; r++)
                {       temp->wd();
                        temp=temp->bottom;
                }       temp=temp->right;}
}
/*End*/
/*****************************************************************/
/*Main function of cell dynamics*/
int main()
{
        srand(time(NULL)); //random seed
        double a=0; double e=0; double d=0;
        double w_t=0;
        /*defining output file*/
         realization not shown here

        int t=0;
        double Rw = 0.3;//wound bet width rati

        /*repeat for different parameter settings*/
        for (a=0;a<=1*max_r; a = a + 0.05*max_r)
        {
                for (d = 0; d <= 3*max_r; d = d + 0.1*max_r)
                {
                        for (e = 0; e <= 1*max_r; e = e + 0.05*max_r)
                        {       node *first = new node(1);
                                create_network(first, s);
                                seed(first, a, e, d);
                                int time = 0;
                                for (time = 0; time < max_t; time++)
                                {
                                        /*instant data collection */
```

```
                    int num = 0;
                    int g0 = 0; //temporary arrested cell No.
                    int age = 0; //average age
                    int pm = 0;//permanent arrest
                    /*end*/
                    /*wounding*/
                    if (time == w_t)
                    {       wound(first, s, Rw*s);        }
                    /*Natural growth*/
                    if ((time != w_t))
                    {       process(first, s); }

                    /*collect instant data, and output them*/
                    node * temp = first;
                    for (int r = 0; r < s; r++)
                    {       for (int l = 0; l < h; l++)
                            {       num += (int)temp->observable[0];
                                    age += (int)temp->observable[1];
                                    g0 += (int)temp->observable[2];
                                    pm += (int)temp->observable[6];
                                    ecm += temp->ecm;
                                    temp = temp->bottom;
                            }
                            temp = temp->right;
                    }

                    }}}}
/*close output files*/          realization not shown here.
 return 0;}
```

Reference

1. Weinberg, S. (1992). Dreams of a Final Theory: the Search for the Fundamental Laws of Nature. Pantheon Books, N.Y.
2. Shiva, V. (1987). The violence of reductionist science. Alternatives, 12(2), 243-261.
3. Gallagher, R., Appenzeller, T., & Normile, D. (1999). Beyond reductionism. Science, 284(5411), 79.
4. Kauffman, S. (2009). Towards a post reductionist science: the Open Universe. arXiv preprint arXiv:0907.2492.
5. Lewin, R. (1999). Complexity: Life at the edge of chaos. University of Chicago Press.
6. Anderson, P. W. (1972). More is different. Science, 177(4047), 393-396.
7. Gorban, A. N., & Yablonsky, G. S. (2013). Grasping complexity. arXiv preprint arXiv:1303.3855.
8. Cohen, S. Marc, "Aristotle's Metaphysics", The Stanford Encyclopedia of Philosophy (Winter 2016 Edition), Edward N. Zalta (ed.), URL = <https://plato.stanford.edu/archives/win2016/entries/aristotle-metaphysics/>.1045, Book VIII 1045a20–25
9. Barillot. E. (2013). Computational systems biology of cancer (CRC Press, Boca Raton, FL),332-335.
10. Le Cam, L. (1986). The central limit theorem around 1935. Statistical science, 78-91Sibeon, R. (1999). Anti-reductionist sociology. Sociology, 33(2), 317-334.
11. Landau, L. D., & Lifshitz, E. M. (2013). Course of theoretical physics. Elsevier.
12. Castellano, C., Fortunato, S., & Loreto, V. (2009). Statistical physics of social dynamics. Reviews of modern physics, 81(2), 591
13. Sella, G., & Hirsh, A. E. (2005). The application of statistical physics to evolutionary biology. Proceedings of the National Academy of Sciences of the United States of America, 102(27), 9541-9546.
14. Albert, R., & Barabási, A. L. (2002). Statistical mechanics of complex networks. Reviews of modern physics, 74(1), 47.
15. Auyang, S. Y. (1999). Foundations of complex-system theories: in economics, evolutionary biology, and statistical physics. Cambridge University Press.
16. Stanley, H. E., Plerou, V., & Gabaix, X. (2008). A statistical physics view of financial fluctuations: Evidence for scaling and universality. Physica A: Statistical Mechanics and its Applications, 387(15), 3967-3981.
17. Radulescu, O., Gorban, A. N., Zinovyev, A., & Lilienbaum, A. (2008). Robust simplifications of multiscale biochemical networks. BMC systems biology, 2(1), 86.
18. Gilbert, W. (1991). Towards a paradigm shift in biology. Nature, 349, 99.
19. Sawyer, R. K. (2002). Emergence in psychology: Lessons from the history of non-reductionist science. Human Development, 45(1), 2-28.
20. Gallagher, S. (2010). Phenomenology and non-reductionist cognitive science. In Handbook of phenomenology and cognitive science (pp. 21-34). Springer Netherlands.
21. O'malley, M. A., & Dupré, J. (2005). Fundamental issues in systems biology. BioEssays, 27(12), 1270-1276.
22. Ideker, T., Galitski, T., & Hood, L. (2001). A new approach to decoding life: systems biology. Annual review of genomics and human genetics, 2(1), 343-372.
23. Kell, D. B., & Oliver, S. G. (2004). Here is the evidence, now what is the hypothesis? The complementary roles of inductive and hypothesis-driven science in the post-genomic era. Bioessays, 26(1), 99-105.
24. Kitano, H. (2002). Systems biology: a brief overview. Science, 295(5560), 1662-1664.
25. Wolkenhauer, O. (2001). Systems biology: The reincarnation of systems theory applied in biology?. Briefings in bioinformatics, 2(3), 258-270.
26. Barillot. E. (2013). Computational systems biology of cancer (CRC Press, Boca Raton, FL),17-18.
27. Kondo, S., & Miura, T. (2010). Reaction-diffusion model as a framework for understanding biological pattern formation. science, 329(5999), 1616-1620.
28. Turing, A. M. (1952). The chemical basis of morphogenesis. Philosophical Transactions of the Royal Society of London. Series B, Biological Sciences, 237(641), 37-72.; Wolpert, L. (1971). Positional information and pattern formation. In Current topics in developmental biology (Vol. 6, pp. 183-224). Academic Press. Gierer, A., & Meinhardt, H. (1972). A theory of biological pattern formation. Kybernetik, 12(1), 30-39.
29. Rothman, D. H., & Zaleski, S. (2004). Lattice-gas cellular automata: simple models of complex hydrodynamics (Vol. 5). Cambridge University Press; Chopard, B., Ouared, R., Deutsch, A., Hatzikirou, H., & Wolf-Gladrow, D. (2010). Lattice-gas cellular automaton models for biology: from fluids to cells. Acta Biotheoretica, 58(4), 329-340.
30. Glazier, J. A., Balter, A., & Popławski, N. J. (2007). Magnetization to morphogenesis: a brief history of the Glazier-

Graner-Hogeweg model. In Single-Cell-Based Models in Biology and Medicine (pp. 79-106). Birkhäuser Basel; Marée, A. F., Grieneisen, V. A., & Hogeweg, P. (2007). The Cellular Potts Model and biophysical properties of cells, tissues and morphogenesis. In Single-cell-based models in biology and medicine (pp. 107-136). Birkhäuser Basel.

31. Graner, F., & Glazier, J. A. (1992). Simulation of biological cell sorting using a two-dimensional extended Potts model. Physical review letters, 69(13), 2013.
32. Moreira, J., & Deutsch, A. (2002). Cellular automaton models of tumor development: a critical review. Advances in Complex Systems, 5(02n03), 247-267.
33. Bauer, A. L., Jackson, T. L., & Jiang, Y. (2007). A cell-based model exhibiting branching and anastomosis during tumor-induced angiogenesis. Biophysical Journal, 92(9), 3105-3121; Peirce, S. M. (2008). Computational and mathematical modeling of angiogenesis. Microcirculation, 15(8), 739-751.
34. Merks, R. M., & Glazier, J. A. (2005). Dynamic mechanisms of blood vessel growth. Nonlinearity, 19(1), C1.
35. Anderson, A. R. (2003). A hybrid discrete-continuum technique for individual-based migration models. In Polymer and Cell Dynamics (pp. 251-259). Birkhäuser, Basel.
36. Fletcher, A. G., Osterfield, M., Baker, R. E., & Shvartsman, S. Y. (2014). Vertex models of epithelial morphogenesis. Biophysical Journal, 106(11), 2291-2304; Alt, S., Ganguly, P., & Salbreux, G. (2017). Vertex models: from cell mechanics to tissue morphogenesis. Phil. Trans. R. Soc. B, 372(1720), 20150520.
37. Drasdo, D., & Hoehme, S. (2005). A single-cell-based model of tumor growth in vitro: monolayers and spheroids. Physical biology, 2(3), 133; Drasdo, D. (2007). Center-based single-cell models: An approach to multicellular organization based on a conceptual analogy to colloidal particles. In Single-Cell-Based Models in Biology and Medicine (pp. 171-196). Birkhäuser Basel.
38. Palsson, E., & Othmer, H. G. (2000). A model for individual and collective cell movement in Dictyostelium discoideum. Proceedings of the National Academy of Sciences, 97(19), 10448-10453.
39. Meineke, F. A., Potten, C. S., & Loeffler, M. (2001). Cell migration and organization in the intestinal crypt using a lattice-free model. Cell proliferation, 34(4), 253-266.
40. Newman, T. J. (2005). Modeling multi-cellular systems using sub-cellular elements. arXiv preprint q-bio/0504028.
41. McGarry, J. G., & Prendergast, P. J. (2004). A three-dimensional finite element model of an adherent eukaryotic cell. Eur Cell Mater, 7, 27-33; Hutson, M. S., Veldhuis, J., Ma, X., Lynch, H. E., Cranston, P. G., & Brodland, G. W. (2009). Combining laser microsurgery and finite element modeling to assess cell-level epithelial mechanics. Biophysical Journal, 97(12), 3075-3085; Vermolen, F. J., Mul, M. M., & Gefen, A. (2014). Semi-stochastic cell-level computational modeling of the immune system response to bacterial infections and the effects of antibiotics. Biomechanics and modeling in mechanobiology, 13(4), 713-734.;
42. Some of them are: Alarcón, T., Byrne, H. M., & Maini, P. K. (2003). A cellular automaton model for tumour growth in inhomogeneous environment. Journal of theoretical biology, 225(2), 257-274; Anderson, A. R., Weaver, A. M., Cummings, P. T., & Quaranta, V. (2006). Tumor morphology and phenotypic evolution driven by selective pressure from the microenvironment. Cell, 127(5), 905-915; Rejniak, K. A., & Anderson, A. R. (2011). Hybrid models of tumor growth. Wiley Interdisciplinary Reviews: Systems Biology and Medicine, 3(1), 115-125.; Gerlee, P., & Anderson, A. R. (2008). A hybrid cellular automaton model of clonal evolution in cancer: the emergence of the glycolytic phenotype. Journal of theoretical biology, 250(4), 705-722; Zhang, L., Athale, C. A., & Deisboeck, T. S. (2007). Development of a three-dimensional multiscale agent-based tumor model: simulating gene-protein interaction profiles, cell phenotypes and multicellular patterns in brain cancer. Journal of theoretical biology, 244(1), 96-107. Wang, Z., Butner, J. D., Kerketta, R., Cristini, V., & Deisboeck, T. S. (2015, February). Simulating cancer growth with multiscale agent-based modeling. In Seminars in cancer biology (Vol. 30, pp. 70-78). Academic Press; Dallon, J. C. (2007). Models with lattice-free center-based cells interacting with continuum environment variables. In Single-Cell-Based Models in Biology and Medicine (pp. 197-219). Birkhäuser Basel
43. Peskin, C. S. (2002). The immersed boundary method. Acta numerica, 11, 479-517; Peskin, C. S. (1977). Numerical analysis of blood flow in the heart. Journal of computational physics, 25(3), 220-252; Peskin, C. S., & McQueen, D. M. (1989). A three-dimensional computational method for blood flow in the heart I. Immersed elastic fibers in a viscous incompressible fluid. Journal of Computational Physics, 81(2), 372-405.
44. Rejniak, K. A. (2007). An immersed boundary framework for modeling the growth of individual cells: an application to the early tumour development. Journal of theoretical biology, 247(1), 186-204; Rejniak, K. A., & Dillon, R. H. (2007). A single cell-based model of the ductal tumour microarchitecture. Computational and Mathematical Methods in Medicine, 8(1), 51-69.
45. Fogelson, A. L., & Guy, R. D. (2008). Immersed-boundary-type models of intravascular platelet aggregation. Computer

methods in applied mechanics and engineering, 197(25-28), 2087-2104.; Liu, Y., & Liu, W. K. (2006). Rheology of red blood cell aggregation by computer simulation. Journal of Computational Physics, 220(1), 139-154.

46. Biteau, B., Hochmuth, C. E., & Jasper, H. (2011). Maintaining tissue homeostasis: dynamic control of somatic stem cell activity. Cell stem cell, 9(5), 402-411.
47. Rejniak, K. A., & Anderson, A. R. (2008). A computational study of the development of epithelial acini: II. Necessary conditions for structure and lumen stability. Bulletin of mathematical biology, 70(5), 1450; Rejniak, K. A., & Anderson, A. R. (2008). A computational study of the development of epithelial acini: I. Sufficient conditions for the formation of a hollow structure. Bulletin of mathematical biology, 70(3), 677-712.
48. Rejniak, K. A., Quaranta, V., & Anderson, A. R. (2010). Computational investigation of intrinsic and extrinsic mechanisms underlying the formation of carcinoma. Mathematical medicine and biology: a journal of the IMA, 29(1), 67-84; Rejniak, K. A. (2012). Homeostatic imbalance in epithelial ducts and its role in carcinogenesis. Scientifica, 2012.
49. Lou, Y. and Chen, Y., Simulating the multicellular homeostasis with a cell-based discrete receptor dynamics model: The non-mutational origin of cancer and aging, Journal of theoretical biology 404 (2016) 15–29.
50. Meredith, J. E., Fazeli, B., & Schwartz, M. A. (1993). The extracellular matrix as a cell survival factor. Molecular biology of the cell, 4(9), 953-961.
51. Hirsch, H. R., & Engelberg, J. (1965). Determination of the cell doubling-time distribution from culture growth-rate data. Journal of theoretical biology, 9(2), 297-302; Buehring, G. C., & Williams, R. R. (1976). Growth rates of normal and abnormal human mammary epithelia in cell culture. Cancer research, 36(10), 3742-3747; Assanga, I., & Lujan, L. (2013). Cell growth curves for different cell lines and their relationship with biological activities. International Journal of Biotechnology and Molecular Biology Research, 4(4), 60-70.
52. Barkan, D., Green, J. E., & Chambers, A. F. (2010). Extracellular matrix: a gatekeeper in the transition from dormancy to metastatic growth. European journal of cancer, 46(7), 1181-1188.
53. Lee, M., & Vasioukhin, V. (2008). Cell polarity and cancer–cell and tissue polarity as a non-canonical tumor suppressor. Journal of cell science, 121(8), 1141-1150; Wodarz, A., & Näthke, I. (2007). Cell polarity in development and cancer. Nature cell biology, 9(9), 1016.
54. Martin-Belmonte, F., & Perez-Moreno, M. (2012). Epithelial cell polarity, stem cells and cancer. Nature Reviews Cancer, 12(1), 23.
55. Some (but by no means all) of works on the mechanisms of cell cycle arrest: Evan, G. I., & Vousden, K. H. (2001). Proliferation, cell cycle and apoptosis in cancer. Nature, 411(6835), 342; Gérard, C., & Goldbeter, A. (2014). The balance between cell cycle arrest and cell proliferation: control by the extracellular matrix and by contact inhibition. Interface Focus, 4(3), 20130075; Hannon, G. J., & Beach, D. (1994). pl5INK4B is a potentia| effector of TGF-β-induced cell cycle arrest. Nature, 371(6494), 257; Hartwell, L. H., & Kastan, M. B. (1994). Cell cycle control and cancer. Science, 266(5192), 1821-1828; Kastan, M. B., & Bartek, J. (2004). Cell-cycle checkpoints and cancer. Nature, 432(7015), 316; Schwartz, G. K. (2002). CDK inhibitors: cell cycle arrest versus apoptosis. Cell Cycle, 1(2), 113-114; Vermeulen, K., Van Bockstaele, D. R., & Berneman, Z. N. (2003). The cell cycle: a review of regulation, deregulation and therapeutic targets in cancer. Cell proliferation, 36(3), 131-149.
56. Zetterberg, A., & Larsson, O. (1985). Kinetic analysis of regulatory events in G1 leading to proliferation or quiescence of Swiss 3T3 cells. Proceedings of the National Academy of Sciences, 82(16), 5365-5369; Zetterberg, A., Larsson, O., & Wiman, K. G. (1995). What is the restriction point?. Current opinion in cell biology, 7(6), 835-842; Novak, B., & Tyson, J. J. (2004). A model for restriction point control of the mammalian cell cycle. Journal of theoretical biology, 230(4), 563-579.
57. Pardee, A. B., Dubrow, R., Hamlin, J. L., & Kletzien, R. F. (1978). Animal cell cycle. Annual review of biochemistry, 47(1), 715-750; Morgan, D. O. (2007). The cell cycle: principles of control. New Science Press.
58. Hanahan, D., & Weinberg, R. A. (2000). The hallmarks of cancer. cell, 100(1), 57-70.
59. Schwartz, G. K. (2002). CDK inhibitors: cell cycle arrest versus apoptosis. Cell Cycle, 1(2), 113-114; Vermeulen, K., Berneman, Z. N., & Van Bockstaele, D. R. (2003). Cell cycle and apoptosis. Cell proliferation, 36(3), 165-175.
60. Carter, S. B. (1967). Haptotaxis and the mechanism of cell motility. Nature, 213(5073), 256; Haeger, A., Wolf, K., Zegers, M. M., & Friedl, P. (2015). Collective cell migration: guidance principles and hierarchies. Trends in cell biology, 25(9), 556-566; Ridley, A. J., Schwartz, M. A., Burridge, K., Firtel, R. A., Ginsberg, M. H., Borisy, G., ... & Horwitz, A. R. (2003). Cell migration: integrating signals from front to back. Science, 302(5651), 1704-1709.
61. Parsons, J. T., Horwitz, A. R., & Schwartz, M. A. (2010). Cell adhesion: integrating cytoskeletal dynamics and cellular tension. Nature reviews Molecular cell biology, 11(9), 633.
62. Cattaruzza S, Perris R (2005) Proteoglycan control of cell movement during wound healing and cancer

spreading. Matrix Biology 24(6): 400-417.
63. Blagosklonny MV (2011). Cell cycle arrest is not senescence. Aging (Albany NY), 3(2): 94-101; Collado M, Blasco A and Serrano M (2007). Cellular senescence in cancer and aging. Cell 130(2): 223-233.
64. Hoeijmakers, J. H. (2009). DNA damage, aging, and cancer. New England Journal of Medicine, 361(15), 1475-1485. Campisi J, Andersen JK, Kapahi P and Melov S (2011) Cellular senescence: a link between cancer and age-related degenerative disease?. In Seminars in cancer biology (Vol. 21, No. 6, pp. 354-359). Academic Press.
65. Campisi J, Yaswen P (2009) Aging and cancer cell biology, 2009. Aging Cell 8:221-225;
66. Ertel A, Tsirigos A, Whitaker-Menezes D, Birbe R, Pavlides S, Martinez-Outschoorn, UE, ... and Lisanti MP (2012) Is cancer a metabolic rebellion against host aging? In the quest for immortality, tumor cells try to save themselves by boosting mitochondrial metabolism. Cell Cycle 11:253-263.
67. Blagosklonny MV (2012) Answering the ultimate question "what is the proximal cause of aging?". Aging (Albany NY) 4(12): 861-877.
68. Wales, D. (2003). Energy landscapes: Applications to clusters, biomolecules and glasses. Cambridge University Press; Berthier, L., & Biroli, G. (2011). Theoretical perspective on the glass transition and amorphous materials. Reviews of Modern Physics, 83(2), 587.
69. Lou, Y., Sheng, Q., & Chen, Y. (2017). When relaxation meets adaptation in complex adaptive systems: a computational study of tumorigenesis. Advances in Complex Systems, 1750016.
70. Beerenwinkel, N., Antal, T., Dingli, D., Traulsen, A., Kinzler, K. W., Velculescu, V. E., ... & Nowak, M. A. (2007). Genetic progression and the waiting time to cancer. PLoS computational biology, 3(11), e225; Cahill, D. P., Kinzler, K. W., Vogelstein, B., & Lengauer, C. (1999). Genetic instability and Darwinian selection in tumours. Trends in cell biology, 9(12), M57-M60; Crespi, B., & Summers, K. (2005). Evolutionary biology of cancer. Trends in ecology & evolution, 20(10), 545-552; Gillies, R. J., Verduzco, D., & Gatenby, R. A. (2012). Evolutionary dynamics of carcinogenesis and why targeted therapy does not work. Nature Reviews Cancer, 12(7), 487; Merlo, L. M., Pepper, J. W., Reid, B. J., & Maley, C. C. (2006). Cancer as an evolutionary and ecological process. Nature Reviews Cancer, 6(12), 924.
71. Johnson, B. E., Mazor, T., Hong, C., Barnes, M., Aihara, K., McLean, C. Y., ... & Asthana, S. (2014). Mutational analysis reveals the origin and therapy-driven evolution of recurrent glioma. Science, 343(6167), 189-193; Taddei, F., Radman, M., Maynard-Smith, J., Toupance, B., Gouyon, P. H., & Godelle, B. (1997). Role of mutator alleles in adaptive evolution. Nature, 387(6634), 700.
72. Marusyk, A., Almendro, V., & Polyak, K. (2012). Intra-tumour heterogeneity: a looking glass for cancer?. Nature Reviews Cancer, 12(5), 323; Burrell, R. A., McGranahan, N., Bartek, J., & Swanton, C. (2013). The causes and consequences of genetic heterogeneity in cancer evolution. Nature, 501(7467), 338; Swanton, C. (2012). Intratumor heterogeneity: evolution through space and time. Cancer research, 72(19), 4875-4882 ;Alizadeh, A. A., Aranda, V., Bardelli, A., Blanpain, C., Bock, C., Borowski, C., Caldas, C., Califano, A., Doherty, M., Elsner, M., et al., Toward understanding and exploiting tumor heterogeneity, Nature Medicine 21 (2015) 846–853;
73. Ao, P., Galas, D., Hood, L., & Zhu, X. (2008). Cancer as robust intrinsic state of endogenous molecular-cellular network shaped by evolution. Medical Hypotheses, 70(3), 678-684; Yuan, R., Zhu, X., Wang, G., Li, S., & Ao, P. (2017). Cancer as robust intrinsic state shaped by evolution: a key issues review. Reports on Progress in Physics, 80(4), 042701.
74. Drake, J. W., Charlesworth, B., Charlesworth, D., & Crow, J. F. (1998). Rates of spontaneous mutation. Genetics, 148(4), 1667-1686; Martincorena, I., & Campbell, P. J. (2015). Somatic mutation in cancer and normal cells. Science, 349(6255), 1483-1489.
75. Greaves, M., & Maley, C. C. (2012). Clonal evolution in cancer. Nature, 481(7381), 306; Xie, M., Lu, C., Wang, J., McLellan, M. D., Johnson, K. J., Wendl, M. C., ... & Ozenberger, B. A. (2014). Age-related mutations associated with clonal hematopoietic expansion and malignancies. Nature medicine, 20(12), 1472; Sidransky, D., Mikkelsen, T., Schwechheimer, K., Rosenblum, M. L., & Vogelstein, B. (1992). Clonal expansion of p53 mutant cells is associated with brain tumour progression. Nature, 355(6363), 846.
76. Levine, A. J. (1997). p53, the cellular gatekeeper for growth and division. cell, 88(3), 323-331; Levine, A. J., & Oren, M. (2009). The first 30 years of p53: growing ever more complex. Nature Reviews Cancer, 9(10), 749; Song, H., Hollstein, M., & Xu, Y. (2007). p53 gain-of-function cancer mutants induce genetic instability by inactivating ATM. Nature cell biology, 9(5), 573.
77. Fisher, R. A. (1999). The genetical theory of natural selection: a complete variorum edition. Oxford University Press; Wright, S., The Roles of Mutation, Inbreeding, Crossbreeding and Selection in Evolution, Vol. 1 (na, 1932).
78. Wright, S. (1942). Statistical genetics and evolution. Bulletin of the American Mathematical Society, 48(4), 223-246.

79. Bak, P. (2013). How nature works: the science of self-organized criticality. Springer Science & Business Media.
80. Carlson, J. M., & Doyle, J. (2002). Complexity and robustness. Proceedings of the national academy of sciences, 99 (suppl 1), 2538-2545; Hidalgo, J., Grilli, J., Suweis, S., Muñoz, M. A., Banavar, J. R., & Maritan, A. (2014). Information-based fitness and the emergence of criticality in living systems. Proceedings of the National Academy of Sciences, 111(28), 10095-10100.
81. Lou, Y., Xia, J., Tang, W., &Chen, Y.(2017). Linking biological and physical aging: Dynamical scaling of multicellular regeneration. Physical review E 96, 0624118.
82. Bouchaud, J. P., Cugliandolo, L. F., Kurchan, J., & Mezard, M. (1998). Out of equilibrium dynamics in spin-glasses and other glassy systems. Spin glasses and random fields, 161-223.B. Abou, D. Bonn, and J. Meunier, Physical review E 64, 021510 (2001).
83. Hohenberg, P. C., & Halperin, B. I. (1977). Theory of dynamic critical phenomena. Reviews of Modern Physics, 49(3), 435.
84. Henkel, M., & Pleimling, M. (2011). Nonequilibrium Phase Transitions: Volume 2: Ageing and Dynamical Scaling Far from Equilibrium. Springer Science & Business Media.
85. Nicodemi, M., & Coniglio, A. (1999). Aging in out-of-equilibrium dynamics of models for granular media. Physical review letters, 82(5), 916.
86. Martin, P. (1997). Wound healing--aiming for perfect skin regeneration. Science, 276(5309), 75-81.
87. Liang, C. C., Park, A. Y., & Guan, J. L. (2007). In vitro scratch assay: a convenient and inexpensive method for analysis of cell migration in vitro. Nature protocols, 2(2), 329; Jonkman, J. E., Cathcart, J. A., Xu, F., Bartolini, M. E., Amon, J. E., Stevens, K. M., & Colarusso, P. (2014). An introduction to the wound healing assay using live-cell microscopy. Cell adhesion & migration, 8(5), 440-451.
88. Fisher, R. A. (1937). The wave of advance of advantageous genes. Annals of Human Genetics, 7(4), 355-369; Kolmogoroff, A., Petrovsky, I., & Piscounoff, N. (1988). Study of the diffusion equation with growth of the quantity of matter and its application to a biology problem. In Dynamics of Curved Fronts (pp. 105-130).
89. Zahm, J. M., Kaplan, H., Hérard, A. L., Doriot, F., Pierrot, D., Somelette, P., & Puchelle, E. (1997). Cell migration and proliferation during the in vitro wound repair of the respiratory epithelium. Cell motility and the cytoskeleton, 37(1), 33-43; Ronot, X., Doisy, A., & Tracqui, P. (2000). Quantitative study of dynamic behavior of cell monolayers during in vitro wound healing by optical flow analysis. Cytometry Part A, 41(1), 19-30; Bereiter-Hahn, J. (1986). Epidermal cell migration and wound repair. In Biology of the Integument (pp. 443-471). Springer, Berlin, Heidelberg; Riahi, R., Yang, Y., Zhang, D. D., & Wong, P. K. (2012). Advances in wound-healing assays for probing collective cell migration. Journal of laboratory automation, 17(1), 59-65; Haider, A. S., Grabarek, J., Eng, B., Pedraza, P., Ferreri, N. R., Balazs, E. A., & Darzynkiewicz, Z. (2003). In vitro model of "wound healing" analyzed by laser scanning cytometry: accelerated healing of epithelial cell monolayers in the presence of hyaluronate. Cytometry Part A, 53(1), 1-8.
90. Sherratt, J. A., Martin, P., Murray, J. D., & Lewis, J. (1992). Mathematical models of wound healing in embryonic and adult epidermis. Mathematical Medicine and Biology: A Journal of the IMA, 9(3), 177-196; Arciero, J., & Swigon, D. (2013). Equation-based models of wound healing and collective cell migration. In Complex Systems and Computational Biology Approaches to Acute Inflammation (pp. 185-207). Springer, New York, NY; Savla, U., Olson, L. E., & Waters, C. M. (2004). Mathematical modeling of airway epithelial wound closure during cyclic mechanical strain. Journal of Applied Physiology, 96(2), 566-574.
91. Maini, P. K., McElwain, D. S., & Leavesley, D. I. (2004). Traveling wave model to interpret a wound-healing cell migration assay for human peritoneal mesothelial cells. Tissue engineering, 10(3-4), 475-482.
92. Simpson, M. J., Landman, K. A., Hughes, B. D., & Newgreen, D. F. (2006). Looking inside an invasion wave of cells using continuum models: proliferation is the key. Journal of Theoretical Biology, 243(3), 343-360.
93. Tremel, A., Cai, A., Tirtaatmadja, N., Hughes, B. D., Stevens, G. W., Landman, K. A., & O'Connor, A. J. (2009). Cell migration and proliferation during monolayer formation and wound healing. Chemical Engineering Science, 64(2), 247-253.
94. Cai, A. Q., Landman, K. A., & Hughes, B. D. (2007). Multi-scale modeling of a wound-healing cell migration assay. Journal of Theoretical Biology, 245(3), 576-594.
95. Khain, E., Katakowski, M., Charteris, N., Jiang, F., & Chopp, M. (2012). Migration of adhesive glioma cells: Front propagation and fingering. Physical Review E, 86(1), 011904.
96. Charteris, N., & Khain, E. (2014). Modeling chemotaxis of adhesive cells: stochastic lattice approach and continuum description. New Journal of Physics, 16(2), 025002.
97. Simpson, M. J., Towne, C., McElwain, D. S., & Upton, Z. (2010). Migration of breast cancer cells: understanding the

roles of volume exclusion and cell-to-cell adhesion. Physical Review E, 82(4), 041901.
98. Arciero, J. C., Mi, Q., Branca, M., Hackam, D., & Swigon, D. (2013). Using a continuum model to predict closure time of gaps in intestinal epithelial cell layers. Wound Repair and Regeneration, 21(2), 256-265;Ravasio, A., Cheddadi, I., Chen, T., Pereira, T., Ong, H. T., Bertocchi, C., ... & Trepat, X. (2015). Gap geometry dictates epithelial closure efficiency. Nature communications, 6, 7683.
99. Barabási, A. L., & Stanley, H. E. (1995). Fractal concepts in surface growth. Cambridge university press; Constantoudis, V., Patsis, G. P., Leunissen, L. H. A., & Gogolides, E. (2004). Line edge roughness and critical dimension variation: Fractal characterization and comparison using model functions. Journal of Vacuum Science & Technology B: Microelectronics and Nanometer Structures Processing, Measurement, and Phenomena, 22(4), 1974-1981.
100. Reffay, M., Parrini, M. C., Cochet-Escartin, O., Ladoux, B., Buguin, A., Coscoy, S., ... & Silberzan, P. (2014). Interplay of RhoA and mechanical forces in collective cell migration driven by leader cells. Nature cell biology, 16(3), 217.
101. Cochet-Escartin, O., Ranft, J., Silberzan, P., & Marcq, P. (2014). Border forces and friction control epithelial closure dynamics. Biophysical journal, 106(1), 65-73.
102. Anon, E., Serra-Picamal, X., Hersen, P., Gauthier, N. C., Sheetz, M. P., Trepat, X., & Ladoux, B. (2012). Cell crawling mediates collective cell migration to close undamaged epithelial gaps. Proceedings of the National Academy of Sciences, 109(27), 10891-10896.
103. Vedula, S. R. K., Peyret, G., Cheddadi, I., Chen, T., Brugués, A., Hirata, H., ... & Lim, C. T. (2015). Mechanics of epithelial closure over non-adherent environments. Nature communications, 6, 6111.
104. Monthus, C., & Bouchaud, J. P. (1996). Models of traps and glass phenomenology. Journal of Physics A: Mathematical and General, 29(14), 3847.
105. Henkel, M., & Pleimling, M. (2006). Ageing in disordered magnets and local scale invariance. EPL (Europhysics Letters), 76(4), 561.
106. Bouchaud, J. P. (1992). Weak ergodicity breaking and aging in disordered systems. Journal de Physique I, 2(9), 1705-1713
107. Lenormand, G., Alencar, A. M., Trepat, X., Zhou, E. H., Fabry, B., Butler, J. P., & Fredberg, J. J. (2008). The cytoskeleton of the living cell as an out-of-equilibrium system. In Phase Transitions in Cell Biology (pp. 111-141). Springer, Dordrecht.
108. Bi, D., Yang, X., Marchetti, M. C., & Manning, M. L. (2016). Motility-driven glass and jamming transitions in biological tissues. Physical Review X, 6(2), 021011.
109. Angelini, T. E., Hannezo, E., Trepat, X., Marquez, M., Fredberg, J. J., & Weitz, D. A. (2011). Glass-like dynamics of collective cell migration. Proceedings of the National Academy of Sciences, 108(12), 4714-4719.
110. Sadati, M., Qazvini, N. T., Krishnan, R., Park, C. Y., & Fredberg, J. J. (2013). Collective migration and cell jamming. Differentiation, 86(3), 121-125..
111. Sadati, M., Nourhani, A., Fredberg, J. J., & Taheri Qazvini, N. (2014). Glass-like dynamics in the cell and in cellular collectives. Wiley Interdisciplinary Reviews: Systems Biology and Medicine, 6(2), 137-149.
112. Pegoraro, A. F., Fredberg, J. J., & Park, J. A. (2016). Problems in biology with many scales of length: Cell–cell adhesion and cell jamming in collective cellular migration. Experimental cell research, 343(1), 54-59.
113. Garcia, S., Hannezo, E., Elgeti, J., Joanny, J. F., Silberzan, P., & Gov, N. S. (2015). Physics of active jamming during collective cellular motion in a monolayer. Proceedings of the National Academy of Sciences, 112(50), 15314-15319.
114. Berthier, L., & Kurchan, J. (2013). Nonequilibrium glass transitions in driven and active matter. Nature Physics, 9(5), 310; Schimidt, C. (2016). Dynamic steady states and nonequilibrium phase transitions in active biological matter, Banff international Research Station for Mathematical Innovation and Discovery, 10.14288/1.0343616; Steimel, J.P.(2017). Investigating nonequilibrium phenomena in active matter systems, PhD thesis, Massachusetts institute of technology.
115. Potts, R. (1952). Some generalized order-disorder transformations. Mathematical Proceedings of the Cambridge Philosophical Society, 48(1), 106-109. doi: 10.1017/S0305004100027419.
116. Kauffman, S. A. (1992). The origins of order: Self-organization and selection in evolution. In Spin glasses and biology (pp. 61-100).
117. Darwin, C. (1968). On the origin of species by means of natural selection. 1859. London: Murray Google Scholar; Dobzhansky, T. (2013). Nothing in biology makes sense except in the light of evolution. The American biology teacher, 75(2), 87-91.
118. Ao, P. (2005). Laws in Darwinian evolutionary theory. Physics of life Reviews, 2(2), 117-156.
119. Drossel, B. (2001). Biological evolution and statistical physics. Advances in physics, 50(2), 209-295.
120. Dattagupta, S. (2012). Relaxation phenomena in condensed matter physics. Elsevier; Ngai, K. L. (2011). Relaxation

and diffusion in complex systems. Springer Science & Business Media.
121. Guillot, C., & Lecuit, T. (2013). Mechanics of epithelial tissue homeostasis and morphogenesis. Science, 340(6137), 1185-1189; Biteau, B., Hochmuth, C. E., & Jasper, H. (2011). Maintaining tissue homeostasis: dynamic control of somatic stem cell activity. Cell stem cell, 9(5), 402-411.
122. Debreu, G. (1954). Valuation equilibrium and Pareto optimum. Proceedings of the national academy of sciences, 40(7), 588-592.
123. Durlauf, S. N. (1996). Statistical mechanics approaches to socioeconomic behavior; LeBaron, B., & Tesfatsion, L. (2008). Modeling macroeconomies as open-ended dynamic systems of interacting agents. American Economic Review, 98(2), 246-50.
124. Nowak, M. A. (2006). Evolutionary dynamics. Harvard University Press; Smil, V. (2003). The Earth's biosphere: Evolution, dynamics, and change. Mit Press.
125. Nash, J. (1951). Non-cooperative games. Annals of mathematics, 286-295.
126. Smith, J. M. (1988). Evolution and the Theory of Games. In Did Darwin Get It Right? (pp. 202-215). Springer, Boston, MA.; Schweitzer, F., Behera, L., & Mühlenbein, H. (2002). Evolution of cooperation in a spatial prisoner's dilemma. Advances in Complex systems, 5(02n03), 269-299. Myerson, R. B. (2013). Game theory. Harvard university press.
127. Hamilton, W. D. (1964). The genetical evolution of social behaviour. II. Journal of theoretical biology, 7(1), 17-52; Grafen, A. (2006). Optimization of inclusive fitness. Journal of Theoretical Biology, 238(3), 541-563.
128. Barkow, J. H., Cosmides, L., & Tooby, J. (Eds.). (1995). The adapted mind: Evolutionary psychology and the generation of culture. Oxford University Press, USA.
129. Andersen, E. S. (2013). Evolutionary economics: post-Schumpeterian contributions. Routledge; Dosi, G., & Nelson, R. R. (1994). An introduction to evolutionary theories in economics. Journal of evolutionary economics, 4(3), 153-172; Friedman, D. (1998). Evolutionary economics goes mainstream: a review of the theory of learning in games. Journal of Evolutionary Economics, 8(4), 423-432; Holland, J. H., & Miller, J. H. (1991). Artificial adaptive agents in economic theory. The American economic review, 81(2), 365-370.
130. Auyang, S. Y. (1999). Foundations of complex-system theories: in economics, evolutionary biology, and statistical physics. Cambridge University Press; Gros, C., Complex and Adaptive Dynamical Systems (Springer, 2010); Holland, J. H. (1992). Complex adaptive systems. Daedalus, 17-30.
131. Some (by no means all) examples are found in: Arthur, W. B., Durlauf, S. N., & Lane, D. A. (Eds.). (1997). The economy as an evolving complex system II (Vol. 27). Reading, MA: Addison-Wesley; Dooley, K. J. (1997). A complex adaptive systems model of organization change. Nonlinear dynamics, psychology, and life sciences, 1(1), 69-97; Levin, S. A. (1998). Ecosystems and the biosphere as complex adaptive systems. Ecosystems, 1(5), 431-436; Mauboussin, M. J. (2002). Revisiting market efficiency: The stock market as a complex adaptive system. Journal of Applied Corporate Finance, 14(4), 47-55; Pathak, S. D., Day, J. M., Nair, A., Sawaya, W. J., & Kristal, M. M. (2007). Complexity and adaptivity in supply networks: Building supply network theory using a complex adaptive systems perspective. Decision sciences, 38(4), 547-580; Rammel, C., Stagl, S., & Wilfing, H. (2007). Managing complex adaptive systems—a co-evolutionary perspective on natural resource management. Ecological economics, 63(1), 9-21.
132. Gould, S. J., & Lewontin, R. C. (1979, September). The spandrels of San Marco and the Panglossian paradigm: a critique of the adaptationist programme. In Proc. R. Soc. Lond. B (Vol. 205, No. 1161, pp. 581-598). The Royal Society; Levin, S. (2003). Complex adaptive systems: exploring the known, the unknown and the unknowable. Bulletin of the American Mathematical Society, 40(1), 3-19.
133. Elowitz, M. B., Levine, A. J., Siggia, E. D., & Swain, P. S. (2002). Stochastic gene expression in a single cell. Science, 297(5584), 1183-1186
134. Christensen, K., Johnson, T. E., & Vaupel, J. W. (2006). The quest for genetic determinants of human longevity: challenges and insights. Nature Reviews Genetics, 7(6), 436.
135. Carlson, M. E., Hsu, M., & Conboy, I. M. (2008). Imbalance between pSmad3 and Notch induces CDK inhibitors in old muscle stem cells. Nature, 454(7203), 528.
136. Novak, B., Tyson, J. J., Gyorffy, B., & Csikasz-Nagy, A. (2007). Irreversible cell-cycle transitions are due to systems-level feedback. Nature cell biology, 9(7), 724.
137. Bürkle, A., Moreno-Villanueva, M., Bernhard, J., Blasco, M., Zondag, G., Hoeijmakers, J. H., ... & Gonos, E. S. (2015). MARK-AGE biomarkers of ageing. Mechanisms of ageing and development, 151, 2-12.
138. López-Otín, C., Blasco, M. A., Partridge, L., Serrano, M., & Kroemer, G. (2013). The hallmarks of aging. Cell, 153(6), 1194-1217.K. Sousounis, J. A. Baddour, P. A. Tsonis, Curr. Top. Dev. Biol. 108, 217 (2014).

139. Coffman, J. A., Rieger, S., Rogers, A. N., Updike, D. L., & Yin, V. P. (2016). Comparative biology of tissue repair, regeneration and aging. NPJ Regenerative Medicine, 1, 16003.
140. Muller-Sieburg, C. E., Sieburg, H. B., Bernitz, J. M., & Cattarossi, G. (2012). Stem cell heterogeneity: implications for aging and regenerative medicine. Blood, 119(17), 3900-3907.L. C. E. Struik, thesis, Delft University of Technology, 1977.
141. Harley, C. B., Futcher, A. B., & Greider, C. W. (1990). Telomeres shorten during ageing of human fibroblasts. Nature, 345(6274), 458.
142. Jeyapalan, J. C., & Sedivy, J. M. (2008). Cellular senescence and organismal aging. Mechanisms of ageing and development, 129(7-8), 467-474.
143. Conboy, I. M., Conboy, M. J., Wagers, A. J., Girma, E. R., Weissman, I. L., & Rando, T. A. (2005). Rejuvenation of aged progenitor cells by exposure to a young systemic environment. Nature, 433(7027), 760.
144. Cont, R., & Bouchaud, J. P. (2000). Herd behavior and aggregate fluctuations in financial markets. Macroeconomic dynamics, 4(2), 170-196.
145. Demirgüçkunt, A., & Levine, R. (1996). Stock market development and financial intermediaries: stylized facts. World Bank Economic Review,10(2), 291-321.